Regulation of RNA granule composition and non-coding RNA decay in mammalian cells

by

Thao Ngoc Huynh

B.S. Chemistry, Biochemistry Emphasis,

University of Colorado Denver, 2017

A thesis submitted to the

Faculty of the Graduate School of the

University of Colorado in partial fulfillment

of the requirement for the degree of

Doctor of Philosophy

Department of Biochemistry

2023

Committee Members:

Professor Roy Parker

Professor Dylan Taatjes

Professor Robert Batey

Professor Xuedong Liu

Professor Robert Garcea

Huynh, Thao Ngoc (Ph.D., Biochemistry)

Regulation of RNA granule composition and non-coding RNA decay in mammalian cells

Thesis directed by Professor Roy Parker

Gene expression in eukaryotes is regulated at multiple levels. While transcription regulation plays an important role, the regulation of RNA stability and RNA localization are also key factors in controlling gene expression in response to stimuli. This thesis aims to 1) investigate the molecular mechanisms for how mRNAs are targeted to stress granules (SGs) and to 2) identify potential inhibitors for PARN, a deadenylase that is actively involved in regulating non-coding RNAs (ncRNAs) by removing their oligo(A) tails.

1) SGs are conserved cytoplasmic RNA-protein assemblies that form when translation initiation is inhibited. Although RNAs can differentially partition into SGs, the rules that dictate RNA partitioning into SGs are unknown. In this thesis, we demonstrated that SG-enriched NORAD RNA when added to the 3' UTR of a SG-depleted reporter RNA can efficiently target the reporter RNA to SGs through the combined effects of multiple elements. Moreover, we observed that artificial tethering of SG RNA-binding proteins (RBPs), G3BP1, TIA1, or FMRP, can target mRNAs into SGs and SG transcriptome is largely unchanged in cell lines lacking the abundant SG RNA-binding proteins G3BP1 and G3BP2. The data suggest the targeting of ribonucleoproteins (RNPs) into SGs is due to a summation of multiple RNA-protein, protein-protein, and RNA-RNA interactions with no single interaction dominating RNP recruitment into SGs.

2) Poly(A)-specific ribonuclease (PARN) is a 3'-5' exoribonuclease that is shown removes poly(A) tails from the 3' end of ncRNAs to enhance their stability by limiting the access of 3' to 5' exonucleases recruited by oligo(A) tails. Several PARN-regulated miRNAs target p53 mRNA, and PARN knockdown leads to an increase of p53 protein levels in human cells. Thus, PARN inhibitors might be used as a potential therapeutic treatment to repress tumor progression by inducing p53. Herein, we identified four compounds, including three novel compounds and GNF-7, previously shown to be a Bcr-Abl inhibitor, as PARN inhibitors using computational-based molecular docking and high-throughput screening (HTS). These inhibitors can be used as lead compounds for the development of improved PARN inhibitors.

ACKNOWLEDGEMENTS

I am extremely fortunate to have all the love, guidance, and support from many people throughout my life, without them, I would not have been able to finish my thesis projects. I cannot express enough how grateful I am towards everyone, and I would like to thank everyone here.

First and foremost, I would like to thank my Ph.D. PI, Roy Parker, for his endless support and guidance throughout my Ph.D. I have improved so much as an individual and as a scientist thanks to Roy. I greatly appreciate Roy for teaching me how to convey my ideas in a clear and concise manner, giving me uncountable feedbacks on my strengths and weaknesses, and never sugar-coating them. Every discussion we have had is always to help me develop myself. Roy has always been there for help and at the same time given me the confidence that I can solve problems and work independently as a scientist. Thank you for everything, Roy!

I cannot forget to acknowledge all my amazing lab members here. It is such an amazing experience to be able to work and be friends with all the talented and kind people. I would like to thank everyone for all the advice and help whenever I need them. Special thanks to Anne Webb, Carolyn Decker, Denise Muhlrad, and Kathleen McCann for keeping everything up and running smoothly in the lab. I also want to acknowledge Briana Van Treeck. I was lucky to work together with her when I first joined the lab, I was really impressed by her energy, her enthusiasm for science, and of course her science. Thanks to all the post-docs (Stephanie Moon, Anthony Khong, Siddharth Shukkla, Nina

Ripin, James Burke, Kate Westkamp, J.P. Ouyang, Meaghan Val Alstyne, Dylan Parker, and Edward Courvan) for being leading example of high-quality scientists. Thanks to my fellow Parker lab graduate students (Giulia Corbet, Denvin Tauber, Evan Lester, James Pratt, Liyi Cheng, Gaia Bublitz, and Luisa Macedo de Vasconcelos). It has been amazing working with you all. I would also thanks Jeff Kuo for all the help and advice and Olke Uhlenbeck for all his ideas on my projects during lab meetings.

The biochemistry department at CU has been a wonderful place to be in with countless support and collaborations. I would like to thank the Tissue Culture Facility, Theresa Nahreini and Nickole Kethley, and the Imaging Core, Joseph Dragavon. Also, thanks to Cech and Batey labs for sharing some reagents with me and give me advice when I needed them. Special thanks to Arthur Zaug in the Cech lab for being extremely helpful and constantly looking at my northern blots to give me advice.

I highly appreciate the thoughts and suggestions from my committees. I am fortunate to have Dylan Taatjes, Robert Batey, Xuedong Liu, and Robert Garcea to provide insights into my projects.

I would not have made it to graduate school without my undergraduate mentors. My undergraduate PI, Xiaojun Ren, prepared me with the skillsets and scientific knowledge to be successful as a Ph.D. student. I would like to thank Xiaojun Ren, Douglas Dyckes and Vanessa Fishback for all their guidance and support in science and in my life.

Thanks to all my closest friends I have ever had since childhood: Mai Huong, Dang Thong, Nhu Quynh, Thuy Tien, Kim Ngan, Ngoc Thuyet, Phuong Thao, and Mai Thao. Thank you for always being there listening to my complaints and supporting me no matter how far we are apart.

My graduate work would be impossible without my family. Thank you for your unconditional love and support. My parents have always been there to share happy moments or to encourage me at hard times. They have sacrificed a lot to bring me where I am now it is a true blessing to have them around. I also want to acknowledge my brother for being there when I need. I would like to thank my grandfather, grandma, grandaunts, aunts, uncles, and cousins for taking care of me and giving me all the love. Thanks, my son, Val, for providing unconditional love and reminding me of how strong I can be. Thanks to Remy for being a great helper and an awesome sister to Val. I also appreciate my in-laws, Janene, Robert, Channing, Lindsey, Witny, Hannah, my nieces and nephew for their love and support. Finally, I want to express how much I appreciate my best friend and husband, Desmond Hamilton, for his love, companionship, and support through different stages of my life. Thank you for always being there for me and our family.

CONTENTS

TABLES

Appendix

FIGURES

CHAPTER I

Stress granules and the PARN, TOE1, and USB1 RNA deadenylases and their roles in RNA regulation.

1.1. Abstract

RNAs are regulated at multiple steps, including transcription, splicing, RNA decay, RNA localization, and translation. One mechanism for the degradation of ncRNAs involves the addition of oligo(A) tails by noncanonical poly(A) polymerases, which then recruit processive sequence-independent 3’ to 5’ exonucleases for RNA degradation. This pathway of decay is also regulated by three 3' to 5' exoribonucleases, USB1, PARN, and TOE1, which remove oligo(A) tails and thereby can protect ncRNAs from decay. Loss of function mutations in these nucleases leads to premature degradation of some ncRNAs, which can be coupled to altered RNA processing, and leads to specific human diseases such as poikiloderma with neutropenia for Usb1 (PN), dyskeratosis congenita for PARN (DC) and Pontocarebella Hypoplasia type 7 for TOE1 (PCH7). On the other hand, mRNAs are proposed to be sorted to ribonucleoprotein (RNP) granules for gene expression regulation. Herein, we review 1) the biochemical properties of Usb1, PARN, and TOE1, how they modulate ncRNA levels, and their roles in human diseases and 2) how RNAs are targeted to RNP (ribonucleoprotein) granules and their roles in mRNA regulations.

1.2. Introduction

Gene expression in eukaryotes is regulated at multiple levels. While transcription regulation plays important role, the regulation of RNA processing and degradation can play important roles in controlling both mRNAs and non-coding RNAs (ncRNAs) [1].

After transcription, 3’ end modifications of mRNA molecules can modulate the fate of newly synthesized RNAs. The 3’ ends of mRNAs are dynamically changed by the opposing effects of poly(A) polymerases and exonucleases, which can affect all aspects of mRNA metabolism [2]. For example, the addition of poly(A) tails to mRNAs promotes their processing, export, and translation [3-7]. Moreover, 3' poly(A) tails on mRNAs can increase their stability by reducing the rate of decapping and/or inhibiting access to 3' to 5' exonucleases [8].

Similarly, 3’-end modifications of ncRNAs can regulate RNA processing and/or degradation. For instance, the addition of CCA to tRNA and uridylation of U6 small nuclear RNA (snRNA) are involved in RNA maturation [9-11], and the polyuridylation of let-7 pre-miRNA by TUT4/TUT7 enhances its processing into mature let-7 [12]. In contrast, other polymerases can promote degradation. For example, non-canonical poly(A) polymerases of the TRAMP complex interact with the nuclear exosome complex and are involved in the 3’ end processing and degradation of rRNAs and snoRNAs [13-15]. Similarly. the uridylation of target RNAs, such as uridylation of let-7 pre-miRNA by TUT4/TUT7, or histone mRNAs [16], can recruit exonucleases for RNA degradation [13-15,17-21].

Oligo(A) tail addition can also promote the degradation of some ncRNAs. For example, oligoadenylation by PAPD5/PAPD7 of miRNAs, human telomerase RNA (hTR), Y RNAs, rRNAs, snoRNAs, scaRNAs, and snRNAs can recruit exonucleases to degrade the RNAs [22-30]. Similarly, PAPD5-mediated adenylation has been proposed to destabilize miR-21 and hTR in human cancer cell lines [22,25-28].

Since oligo(A) tails can promote RNA degradation, it is not surprising that a set of deadenylases can remove oligo(A) tails and thereby stabilize some ncRNAs. To date, there are three such ncRNA deadenylases that can regulate ncRNAs in this manner including the poly(A) specific ribonuclease (PARN), Usb1 (also called Mpn1), and Target of Erg1 (TOE1, also called Caf1z). Recent studies have shown that these enzymes regulate the stability of several ncRNAs in mammalian cells, such as human telomerase RNA (hTR), Y RNAs, piRNAs, and miRNAs by removing poly(A) tails added by PAPD5/7. The poly(A) tail removal limits the recruitment of exonucleases DIS3L, DIS3L2, and/or the nuclease exosome [22-37].

Usb1, PARN, and TOE1 are also linked to several human diseases [32,38-48]. Loss of function mutations in Usb1 lead to the genetic disorder poikiloderma with neutropenia, an autosomal-recessive bone marrow failure (BMF) syndrome with marked clinical overlap with dyskeratosis congenita (DC) [49]. Loss of function mutations in PARN were shown to cause a severe form of DC called Hoyeraal-Hreidarsson syndrome, which causes abnormally short telomeres and congenital defects [38-41] and idiopathic pulmonary fibrosis [40]. Finally, biallelic loss of function mutations in TOE1 gene cause Pontocarebella Hypoplasia type 7 (PCH7), a unique recessive syndrome characterized by neurodegeneration with ambiguous genitalia [32,45].

Another pathway involved in RNA regulation is through RNP (ribonucleoprotein) granules. RNP granules form from a combination of RNA-RNA, protein-RNA, and protein protein interactions [50,51]. Nuclear RNP granules include the nucleolus, paraspeckles, and

Cajal bodies [52]. In the cytoplasm, common RNP granules are P-bodies (PBs), which are composed of untranslating mRNAs and components of the translation repression and mRNA degradation mechinery, and stres granules (SGs), which contain untranslating mRNAs and some RNA binding proteins (RBPs) and translation factors [53,54]. RNP granules are also found in oocytes and embryos, where they play a role in sequestering maternal mRNAs, and in neurons, where neuronal RNP granules can affect at least some forms of synaptic plasticity [55-58].

SGs are conserved cytoplasmic RNP assemblies that form as a result of inhibition of translation initiation [53]. SGs, composed of non-translating mRNPs, are involved in the stress response, neurodegenerative diseases, and viral infections [53,59]. SGs also share many protein components with neuronal granules. Interestingly, mutations that increase SG formation or disturb SG clearance are implicated in degenerative diseases such as amyotrophic lateral sclerosis (ALS) and multisystem proteinopathy, where aberrant SG-like assemblies form [60-65]. Understanding how RNAs and proteins are recruited to and retained in SGs will provide tools for studying SG functions and may give insights into the functions, organization, and mechanisms of other membrane-less RNA bodies such as PBs, Cajal bodies, and the nucleolus.

SGs and other RNP granules have been proposed to form by a summation of potential RNA-RBP, RBP-RBP, and RNA-RNA interactions. The roles of proteins in SG and other RNP granule formation have been previously reviewed [51,53,56,66]. Here, we focus

on RNAs in RNPs and how RNAs are targeted to these RNP assemblies via RBP-RNA and RNA-RNA interactions.

Herein, we review the properties of Usb1, PARN, and TOE1 in different species and their roles in RNA regulation. Moreover, since mutants in these enzymes lead to diseases, understanding their functions and targets will provide insights into treatments for these diseases. We also discuss the roles of RNAs in RNP assembly and how these granules control RNA regulation.

1.3. Regulation of non-coding RNAs

1.3.1 The Usb1, PARN, and TOE1 enzymes

Usb1 is a member of the 2H phosphodiesterase superfamily, which can be subdivided into HxT and HxS enzymes, the latter of which contains Usb1 [67]. The 2H phosphodiesterase superfamily is an enzyme family with 2',3'-cyclic or 1',2'-cyclic phosphodiesterase (CPDase) activity, 3'-5' or 2'-5' phosphodiesterase activity, or 2',5'-RNA ligase activity. The active sites of these enzymes all utilize two catalytic histidines within the central HxS/T tetrapeptide motifs that act as a general acid and base, while the serine or threonine residues help coordinate substrates and assist in transition state stabilization [68-74]. In the Usb1 family members these key histidines are His120 and His208 in human Usb1, His109 and His199 in fission yeast *Schizosaccharomyces pombe* (*S. pombe*) Usb1, and His133 and His231 in budding yeast *Saccharomyces cerevisiae* (*S. cerevisiae*). Although the overall sequence conservation can be rather low between family members, all known crystal structures of 2H family members display a characteristic fold

with conserved terminal and transit lobes and the HxS/T motifs centrally positioned in a substrate binding cleft including the human Usb1 protein (**Figure 1.1**) [70,74-83].

Unlike Usb1, PARN and TOE1 belong to the DEDD protein superfamily, one of the 6 exoribonuclease superfamilies [84,85]. Exoribonucleases in the DEDD superfamily are part of the much larger exonuclease superfamily, containing the proofreading domains of many DNA polymerases as well as other DNA exonucleases [86,87]. DEDD-type nucleases are named after their conserved catalytic Asp and Glu residues and include several other conserved residues distributed in three separate sequence motifs [87]. The nucleases of this superfamily coordinate two metal ions in their catalytic mechanism [88]. The DEDD superfamily can be divided into two subgroups, DEDDy and DEDDh, which are distinguished by whether the fifth conserved residue is a tyrosine or a histidine [84]. Based on its crystal structure, PARN was determined to belong to the DEDDh subfamily [84].

PARN consists of three domains: an RNA recognition motif domain (RRM), a nuclease domain, and an R3H domain (**Figure 1.1**). Mutational analyses showed that four conserved DEDD residues in PARN (Asp28, Glu30, Asp292, and Asp382) are essential for the catalytic activity of PARN and are required for the binding of divalent metal ions to PARN [89]. Moreover, when substituting His377 by Ala in C-terminal truncated PARN, PARN's activity is inhibited, suggesting that His377, as the fifth conserved residue, is also essential for the catalytic activity of PARN [90].

There are modest studies on TOE1 structure compared to PARN. Initial inspection of the human genome revealed TOE1 as a distant homolog of yeast Caf1p, which encodes an mRNA deadenylase subunit [91,92]. However, through evolutionary distance analysis, TOE1 shows greater similarity to PARN than to Caf1 [93], which led to TOE1 being classified as a member of the DEDDh family. The TOE1 protein consists of a unique C3H-type zinc finger domain, a DEDD nuclease domain, and an arginine-rich predicted basic nuclear localization signal (NLS) (**Figure 1.1**) [94]. Point mutations TOE1 in the nuclease domain, Asp64Ala and Glu66Ala, showed little deadenylase activity *in vitro*, suggesting these residues are important for TOE1's enzymatic activity [94].

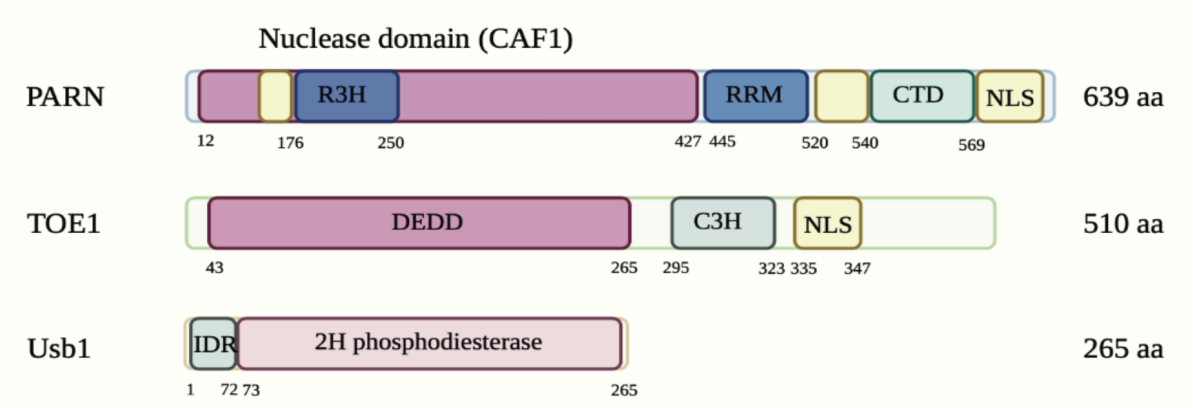

Figure 1.1. Cartoons illustrating the domains of Usb1, PARN, and TOE1.

R3H domain: a conserved sequence motif that is thought to be involved in polynucleotide binding. RRM: RNA regconition motif. NLS: nulcear localization signal. C3H: Cys3His zinc finger domain. IDR: intrinsically disordered region.

1.3.2. Biochemical roles of Usb1, PARN, and TOE1 in RNA regulation

Biochemical Roles of Usb1

Usb1 was first shown to affect U6 snRNA maturation [74]. U6 snRNA is a part of the spliceosome, a large and highly dynamic complex that acts to remove introns from precursor messenger RNAs [43,68,95,96]. Nascent human U6 and U6atac snRNA transcripts are transcribed with a heterogeneous polyuridine 3' end, owing to the stochastic nature of RNA polymerase III terminations [97,98]. While TUT1 catalyzes 3' polyuridylation of U6 and U6atac snRNAs, Usb1 removes 3' uridines from U6 [74]. More specifically, *in vitro* experiments showed that Usb1 can remove uridine nucleotides from the 3' end of U6 snRNA and catalyzes a formation of terminal 2', 3' cyclic phosphate, which stimulates the binding of Lsm2-8 and leads to the formation of U6 snRNPs [75,81,99-101].

Human and yeast Usb1 appear to process U6 snRNAs differently, despite sharing highly similar structures. *In vitro* analyses showed that the human Usb1 post-transcriptionally removes uridine and adenosine nucleosides from the 3′ ends of spliceosomal U6 snRNA, and can catalyze terminal 2′, 3′-cyclic phosphate formation [74,75,81,102]. Usb1 measures the appropriate length of the U6 oligo(U) tail by reading the position of a key adenine nucleotide (A102) and pausing 5 uridine residues downstream [68,74,75,81,103]. In *S. cerevisiae*, an unbiased genetic screen revealed that the yeast ortholog of *Usb1* is essential for U6 snRNA biogenesis and cell viability [95]. In *S. cerevisiae*, Usb1 mainly removes a single nucleotide from U6, leaving a 3′ monophosphate which strongly inhibits further processing [81]. This argues that *S. cerevisiae* Usb1 has 2′-CPDase activity

that hydrolyzes the 2′,3′-cyclic phosphate product into a 3′ monophosphate, which is not exhibited in human Usb1.

Crystallography studies showed that even with low similarity in sequence identity (<20%), human and *S. cerevisiae* Usb1 share highly similar structures [74,81]. Moreover, these structures of human Usb1 bound to nucleotides and intact RNA, along with kinetic analyses, and QM/MM simulations, have provided insights into its catalytic mechanism [74,81]. However, despite their similar structure, the mechanism of *S. cerevisiae* Usb1's 2'-CPDase activity remained poorly understood. By comparing *S. cerevisiae* Usb1 and *Kluyveromyces marxianus* Usb1, it has been suggested that the CPDase activity comes from a loop structure that is conserved in yeast and forms a distinct penultimate (n-1) nucleotide binding site [102]. This suggested that the CPDase activity in yeast Usb1 is related to the loop architecture that many yeast species possess but is absent from the human Usb1.

Despite the related role for Usb1 in U6 and U6atac snRNAs processing, Usb1 defects show distinct phenotypes in different species (**Figure 1.2**). In budding yeast, Usb1 deletion leads to cell death [75,95], while in the fission yeast strand, the ΔUsb1 cells only showed reduced proliferation [68]. In both yeast species, Usb1 deletion showed global defects in pre-mRNA splicing, and this can be reversed by overexpressing U6 [68,75,95]. This suggests that these yeast phenotypes are probably linked to U6 processing by Usb1, and a subsequent defect in proper pre-mRNA splicing.

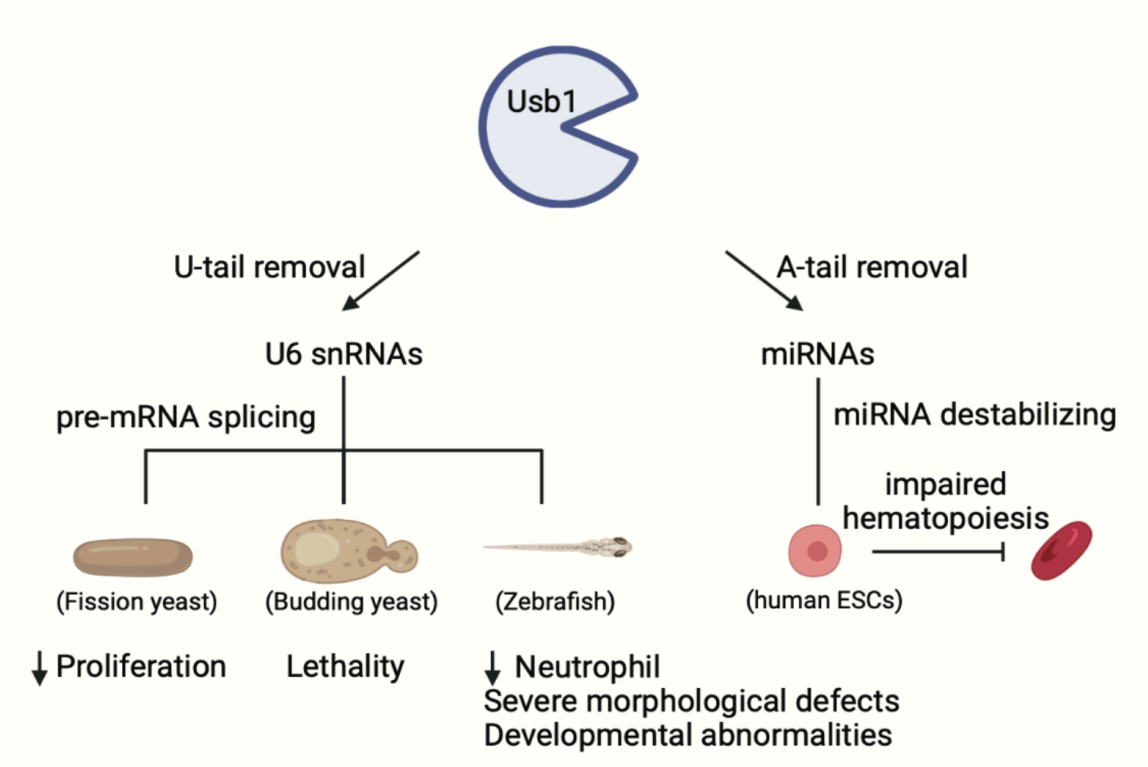

Figure 1.2. Substrates of Usb1 and Usb1-related phenotypes [31,68,75,95,104,105].

Usb1 removes poly(U) tails from U6 snRNAs and poly(A) tails from miRNAs. Usb1-deficiency leads to pre-mRNA splicing defects and miRNA destabilization, resulting in developmental defects of various species and hematopoiesis.

In more complex organisms, Usb1 can affect other processes including hematopoiesis (**Figure 1.2**) [31,104,105]. In PN-modeled zebrafish, morpholino Usb1 KD causes pigmentation and osteochondral defects, severe morphological defects, including a bent tail, think yolk extension, reduced body length, and a significantly decreased number of neutrophils [104,105]. Thus, Usb1-depleted embryos display developmental abnormalities recapitulating the signs of the human syndrome [105]. In this zebrafish model, Usb1 KD also causes splicing defects and a decrease in the formation of aberrant transcripts [104,105]. Specifically, the splicing of genes involved in neutrophil differentiation and development was aberrant in the morphant. Real-time PCR analyses of stage-specific markers showed defects of primitive hematopoiesis [104,105]. Together, these studies demonstrate the intrinsic requirement of Usb1 for hematopoiesis and raise the possibility this could be affected by changes in pre-mRNA splicing.

In humans, Usb1 also regulates hematopoietic development, but this appears to be primarily through deadenylating miRNAs instead of directly affecting splicing (**Figure 1.2 and 1.5A**) [31,75]. The possibility that Usb1 affects miRNAs comes from several observations in experiments done with a pathogenic Usb1 mutation introduced into hESCs [31]. First, while most ncRNAs, mRNAs, and U6 snRNA levels were not affected by the Usb1 mutation, some key miRNAs affecting hematopoietic development were decreased. Second, when these miRNAs were over-expressed, the Usb1 dependent defect in hematopoiesis was rescued. Third, there was an increase in short A tails on miRNAs in the Usb1 mutant, and those tails were reduced by inhibition of the PAPD5/7 adenylase. Finally, inhibition of PAPD5/7 adenylase rescued miRNA levels and the defect

in development seen in the Usb1 mutant cells. While Usb1 generally acts on U-tails, it can remove poly(A) tails *in vitro* [74]. These results suggest that one function of Usb1 is to remove oligo(A) tails of miRNAs and thereby regulate human hematopoiesis.

Usb1 may regulate hematopoiesis in a tissue-specific manner. Usb1 is required for U6 and U6atac snRNA processing and there are observed defects in pre-mRNA splicing in PN-modeled zebrafish [68,95,104,105]. However, in PN-modeled zebrafish, there was no difference in U6 snRNA levels between wild-type and Usb1-deficient embryos and only the genes involved in neutrophil differentiation and development showed splicing defects, not the hematopoietic precursors and erythroid-specific genes [104]. These observations are consistent with the data from human PN that lymphoblastoid cells do not exhibit reduced U6 snRNA levels and have normal pre-mRNA splicing [75] and Usb1 acts as a miRNA deadenylase to regulate hematopoiesis [31]. These data suggested that Usb1 might affect both splicing by U6 processing and miRNA stability by removing 3' end adenylated tails added by PAPD5/7 to regulate hematopoiesis in a tissue-specific manner.

Biochemical Roles of PARN

PARN is a poly(A) specific nuclease, first identified in extracts of *Xenopus* oocytes [106]. PARN removes poly(A) tails from RNAs and releases 5' AMP as a reaction product. It is suggested that the homodimer of PARN may function as a structural unit for its enzymatic activity since the substitution of Ile113, Phe123, or Phe127, important residues for homodimerization, inactivated or reduced PARN's activity significantly [90]. PARN has

been demonstrated to prefer to cleave a poly(A) substrate with a free 3'-OH group [107,108]. This idea was supported by crystal structure showing that Glu30 specifically interacts with the 3'-OH group of the ribose. This observation suggested that Glu30 may act both as the catalytic residue and also confer specificity for the recognition of the 3' poly(A) tail.

Among all deadenylases, PARN is unique since it can bind both the cap structure and the poly(A) tail during deadenylation [109-113]. PARN recognizes and binds m7GpppG through Trp residue in the RRM domain (Trp475 in human and Trp468 in mouse) while the R3H domain helps to stabilize PARN [113-115]. PARN's activity was higher when processing RNA with 5'-cap structure compared to noncapped RNA substrates and the addition of free m7GpppG cap analog inhibited poly(A) degradation *in vitro*, suggesting that 3' end poly(A) removal is linked to 5' end cap structure of the RNA substrates [108,109,111]. One unclear functional property of PARN is its specificity for poly(A). Biochemical studies have shown that PARN degrades poly(A) the most efficiently and poly(U) under certain conditions but not poly(C) and poly(G) [107,108]. Since there are no H-bonding interactions between adenine bases and the protein and the backbone phosphates and ribose moieties make more interactions with the protein compared to adenine based on crystal structure, how PARN achieves specificity for poly(A) remains undecided [90].

Recent studies have identified several targets of PARN. Even though PARN was suspected as a key regulator for mRNAs due to its preference for m7G-cap and its role in global poly(A) shortening during *Xenopus* oocyte [106,107,116], PARN was shown to

predominantly localize to the nucleolus and cytoplasmic foci and process ncRNAs in Hela cells, such as 18S rRNAs, snoRNAs, hTR, scaRNAs, piRNAs, Y RNAs, and miRNAs (**Figure 1.3**) [22-27,29,30,117-123].

PARN also plays important roles in development **(Figure 1.3**). PARN is essential in plant development [124-126]. Specifically, PARN mutant embryos showed developmental defects in higher plants, which has been proposed to be due to a failure to remove the 3' poly(A) tails on a specific subsets of mRNAs [126]. In *C. elegans*, PARN mutants showed reduced brood size and fertility compared to wild-type animals and accumulated untrimmed piRNAs with 3' extensions [37,93]. Moreover, during *Xenopus* oocyte maturation, PARN was shown to cause global poly(A) shortening [106,107,116]. These studies indicated that PARN deadenylase activity is crucial for the development of various species.

PARN deadenylase activity is involved in cancers and human diseases. A recent study found that in acute lymphocytic leukemia (ALL) and acute myeloid leukemia (AML), PARN expression levels were increased compared to non-malignant clinical samples [127]. In lung cancer, expression of PARN is associated with increased overall survival [128]. Moreover, mutations in *PARN* are associated with Dyskeratosis Congenita (DC) and the familial form of idiopathic pulmonary fibrosis (IPF), an age-related disease featuring processive lung scarring [38-41,47]. Both of these diseases are characterized by defects in telomerase activity and shorter telomeres [38-41]. Since PARN acts as a deadenylase to remove 3' oligoadenylated ends of hTR, this suggests a link between PARN, hTR deadenylation, and the causes of DC and IPF (**Figure 1.3 and 1.5B**) [22,29,129].

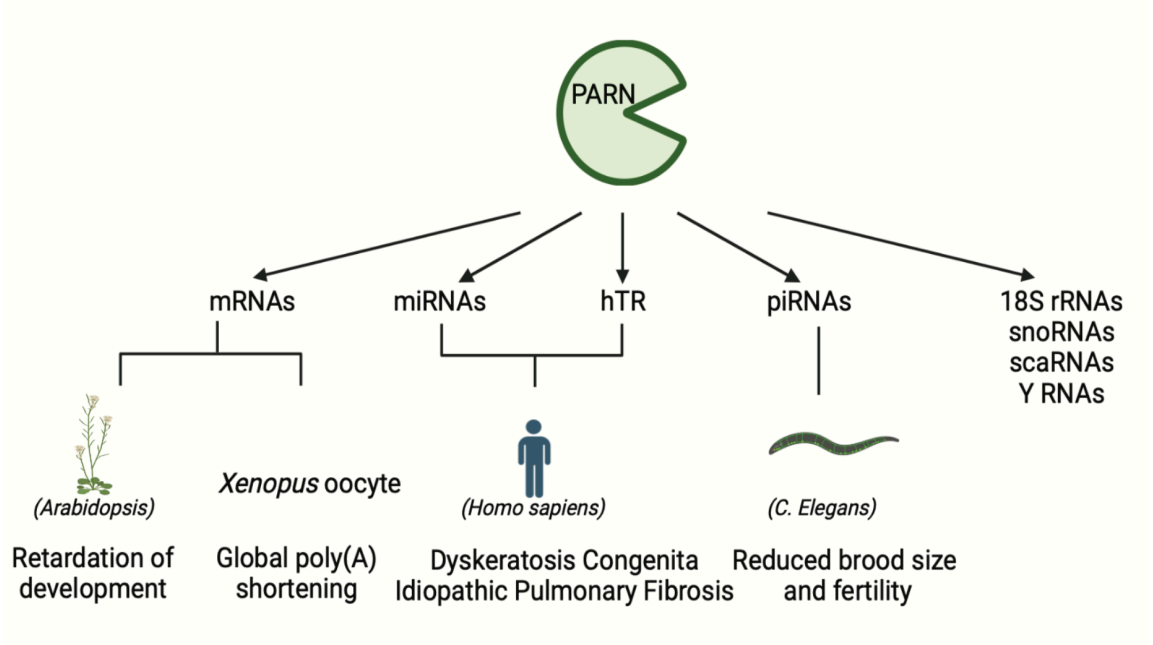

Figure 1.3. Substrates of PARN and PARN-related phenotypes [22-27,29,30,38-41,47,102-105,112,124-126]**.**

PARN removes poly(A) tails from mRNAs, miRNAs, hTR, piRNAs, 18S rRNAs, snoRNAs, scaRNAs, and Y RNAs. PARN mutants show dysregulation of these RNAs and lead to developmental defects in higher plants, zebrafish, *C.elegans*, and DC and IPF in human.

PARN requires binding partners for proper regulation in cells. The binding partners can either repress or activate the enzyme's activities. For example, the interaction of the poly(A) tail with poly(A) binding proteins (PABPs) and/or the interaction of cap-binding proteins (CBPs) such as eIF4E and CBP80 with the 5' cap structure have been shown to repress PARN and protect RNA substrates [130,131]. On the other hand, several RNA-binding proteins (RBPs) help to recruit PARN to the target RNAs for poly(A) removal. For instance, the CUG-binding protein (CUG-BP) can bind to cFos and TNFα mRNA and stimulate the poly(A) tail shortening of these RNAs by recruiting PARN [132]. Similarly, miR-125b-loaded miRISC has been suggested to contribute to the specific recruitment of PARN to TP53 mRNA to regulate p53 levels [133]. Finally, human tristetraproline (TTP) activates PARN activity when transfected in HEK293 extracts and this activation requires the binding of TTP to RNAs [134].

Biochemical Roles of TOE1

TOE1 is a deadenylase that was first identified as a target of Erg1, an immediate early transcription factor. One function of Erg1 is to decrease the growth and tumorigenic potential of several tumor cell types [135,136] and TOE1 was shown to be accountable for the growth inhibitory effect of Erg1 [91]. Since TOE1 shows high similarity to PARN through evolutionary distance analysis [93], one could hypothesize that TOE1 may act redundantly with PARN in removing 3' end tails of RNAs. However, in Hela cells, TOE1 was shown to localize to Cajal bodies, while PARN is primarily in the nucleolus, indicating that TOE1 and PARN have distinct subcellular locations [29,30,117].

TOE1 exhibits deadenylation on RNA substrates and shows a preference for poly(A) [94]. However, TOE1 catalyzes rapid deadenylation followed by a slower 3'-to-5' exonucleolytic decay of non-poly(A) sequences, which is distinct from PARN [94].

TOE1 has been shown to deadenylate several ncRNAs. For instance, TOE1 processes snRNAs [32]. More specifically, TOE1 promotes the maturation of all regular RNA polymerase II transcribed snRNAs of the major and minor spliceosomes by removing 3' oligo(A) tails and preventing nuclear exosome targeting [33]. However, TOE1 showed little to no activity on tested U1 variant snRNAs, leading to exosome degradation, suggesting that TOE1 removal of oligo(A) tails on snRNAs and snoRNAs can provide a mechanism for RNA quality control [33]. TOE1 does show some overlap of substrates with PARN, and together both these enzymes can act on snoRNAs, scaRNAs, and hTR (**Figure 1.4**) [30,34].

TOE1 expression also shows effects on development. Over-expression of TOE1 negatively affects the growth of HEK293 and H4 cells by altering the cell cycle through the induction of p21 [34,91]. On the contrary, TOE1 KD causes developmental arrest during the morula-to-blastocyst transition in mice by upregulating p21 [137]. These studies suggest that TOE1 regulating p21 may be tissue-specific and further investigation of the molecular mechanism of TOE1 is needed for a better understanding of TOE1's role in development.

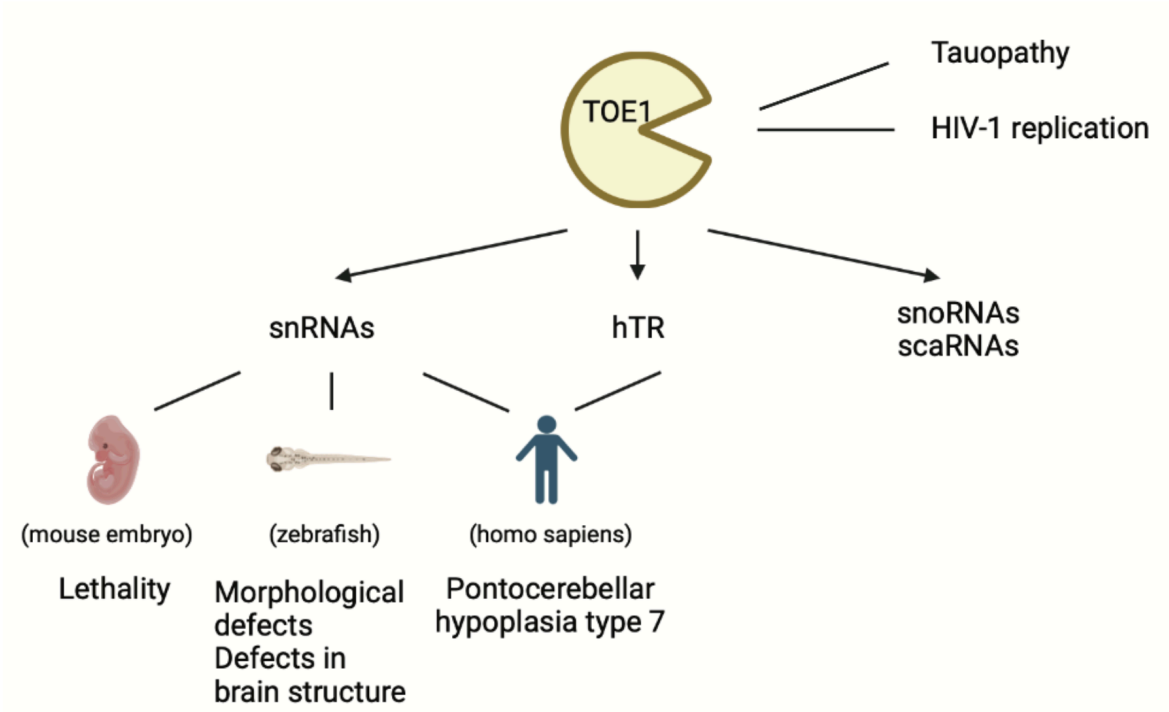

Figure 1.4. Substrates of TOE1 and TOE1-related phenotypes [30,32,34,45,138,139].

TOE1 removes poly(A) tails from snRNAs, hTR, snoRNAs, and scaRNAs. TOE1 mutants in PCH7 patients and PCH7-modeled mice and zebra lead to extended adenylated 3' ends of hTR and snRNAs, resulting in developmental defects and defects in brain structures.

TOE1 is involved in Pontocerebellar hypoplasia type (PCH) 7 (**Figure 1.4 and 1.5C**). Various mutations in *TOE1* were found in PCH7 patients [32,45]. Mouse embryos with homozygous *Toe1* frameshift mutations showed uniform lethality demonstrating *Toe1* is required for mouse development. Furthermore, in a PCH7-disease model using zebrafish, knockdown of the single *toe1* orthologue led to reproducible microcephaly, small eye, and curly tail phenotype in 90% of embryos with defects in the brain structure of the midbrain, cerebellum, and hindbrain by 48 hours post-fertilization, which was rescued by co-injection of human *TOE1* mRNA but not the catalytically inactive DE mutant- or patient mutation-encoding mRNAs, suggesting that reduced expression of TOE1 leads to neurodegeneration and PCH-like brain defects *in vivo* [32]. Moreover, TOE1 DE-associated snRNAs are predominantly enriched for untemplated 3' adenosine [32], suggesting a link between PCH7 and TOE1 deadenylase activity on the processing of snRNA 3' ends.

TOE1 is also suggested to modulate HIV-1 infection (**Figure 1.4**). TOE1 was shown to directly interact with the HIV viral transactivation response element as part of the inhibitory mechanism [138]. Moreover, TOE1 can be secreted following immune response activation and exhibits the ability to spontaneously cross the plasma membrane and penetrate cells in culture [138]. Interestingly, exogenously added TOE1 can also inhibit HIV-1 LTR (long terminal repeat) transactivation, retaining HIV-1 inhibitory activity [138]. Both TOE1's antiviral potency and its cell-penetrating capability have been identified to lie within the 35-amino-acid region containing the nuclear localization signal (NLS) [138]. The direct mechanism by which TOE1 inhibits HIV remains to be clearly worked out but is likely to involve deadenylation of some RNAs.

TOE1 was also shown to be involved in tauopathy. In *C. elegans*, loss of parn-2, an ortholog of TOE1, partially suppressed tauopathy [139]. Moreover, this might be relevant to human disease since Alzheimer's disease patients with low TOE1 levels exhibit significantly increased pathological tau deposit [139]. Furthermore, blocking 3' end poly(A) extensions with cordycepin exacerbated tauopathy in human cultured cells [139]. Together, these data suggest that there is a link between tauopathy, TOE1, and poly(A) RNA metabolism.

Similar to PARN, TOE1 has been shown to associate with several proteins, like hCcr4d, DKC1 (TERC subunit), and spliceosomal proteins [32,34,94]; however, there has not been established mechanism of TOE1's functions regarding these associations.

1.3.3. Human diseases are caused by failure to deadenylate ncRNAs

A striking hallmark is that loss-of-function mutations in Usb1, PARN, and TOE1 are all involved in human diseases featuring abnormal 3' end extensions of ncRNAs (**Figure 1.5**) [32,38-42,44-48]. For example, Usb1 mutants cause accumulated poly(A) tails on miRNAs in PN, while TOE1 and PARN mutants fail to remove poly(A) tails from snRNAs, miRNAs, and hTR in PCH7 and DC. Interestingly, miRNAs and hTR are adenylated by PAPD5/7, and inhibition of PAPD5 can rescue the effects of the deadenylases' mutants on these RNAs. Together, this argues that the regulation of 3' oligo(A) tails on ncRNAs play important roles in diseases and may be a potential therapeutic target for these diseases.

Loss-of-function mutations in Usb1 in humans leads to Poikiloderma with neutropenia (PN) (**Figure 1.5A**), which is a rare, autosomal recessive skin condition (OMIM 604173). To date, there are 38 PN patients reported with 19 different mutations in *C16orf57* gene [43,49,140]. Based on the bioinformatic prediction, all *C16orf57* mutations impair the protein structure by either removing one or both tetrapeptide motifs, or destroying the symmetry of the native folding. Mutations in *C16orf57* gene also produce phenotypes with marked clinical overlap with dyskeratosis congenita (DC) and Rothmond-Thomson syndrome (RTS), a poikiloderma that is sometimes confused with PN [49]. However, unlike patients with DC, which is often caused by mutations in factors involving telomere maintenance, telomeres in PN patients are not significantly shortened, and therefore telomere length represents a clear distinguishable feature for the correct diagnosis of these different BMF syndromes [48]. RTS can also be distinguished from PN since RTS patients harbor mutations in the RECQL4 DNA helicase, which is involved in DNA repair and replication [141]. Thus, mutations in *C16orf57* can be used as a molecular marker for precise diagnosis.

In humans, it appears Usb1 acts as a miRNA deadenylase to regulate hematopoietic development (**Figure 1.3A**). A previous study showed that lymphoblastoid cells from PN patients do not exhibit reduced U6 snRNA levels and have normal pre-mRNA splicing [75]. Recently, Jeong et. al. generated human embryonic stem cells harboring PN-associated mutation c.531_delA in USB1 and showed that this mutation severely impairs human hematopoietic development [31]. By using this model system, they demonstrated that hematopoietic failure in Usb1 mutants is caused by dysregulated

miRNA levels in hematopoiesis, due to a failure to remove destabilizing 3' end oligo(A) tails added by PAPD5/7. This phenotype can be reversed by inhibition of PAPD5/7 with a PAPD5/7 inhibitor, RG7834. Despite the dominant role of Usb1 in U6 maturation, this study identified a new role for Usb1 in miRNA regulation and in PN disease.

Loss of function mutations in PARN also leads to a type of bone marrow failure. Specifically, mutations in PARN were found in a severe form of DC known as Hoyeraal-Hreidarsson syndrome and IPF [38-41,46,47]. DC is an inherited, life-threatening bone marrow failure disorder, caused by genetic defects in components of the telomerase holoenzyme in human cells and leads to age-related bone marrow failure and cancer. Most mutations associated with DC are found in genes encoding components of the telomerase enzyme complex including hTR, the telomerase RNP component dyskerin (*DCK1)*, and the catalytic subunit TERC [142,143]. Moreover, it was shown that loss of PARN leads to defective 3' end maturation of hTR, suggesting the link between PARN, hTR maintenance, and the causes of DC and IPF (**Figure 1.5B**) [22,25-27,30,41,129].

PARN deficiency negatively affects the stability of hTR and miRNAs, which is likely to cause severe phenotypes in DC and IPF (**Figure 1.3B and 1.5B**). Several studies have shown that PARN inhibition leads to a failure to remove the poly(A) tail of hTR, leading to the recruitment of nuclear 3' to 5' exonuclease EXOSC10 and RNA degradation [22,25-27,29,30,41,129]. Moreover, it was shown that PARN deficiency also leads to the accumulation of longer poly(A) tails and affects the stability of several miRNAs, which upregulate p53 expression [24]. Since chronic upregulation of p53 signaling would negatively affect cell

growth and development, this could explain the severe phenotype of PARN deficiency in DC patients [24].

Biallelic, loss-of-function mutations in *TOE1* were found in PCH7. PCH is a group of autosomal recessive neurodegenerative disorders with prenatal onset, mainly affecting the growth and survival of neurons in the cerebellar cortex, the dentate, inferior olivary and ventral pontine nuclei [144]. To date, ten subtypes of PCH have been identified [32,144-159]. PCH7 is characterized by neurological deterioration, astrophy/hypoplasia of the pons and cerebellum, muscular hypotonia, and breathing abnormalities, combined with hypogonadism [159].

Patients with PCH7 harbor biallelic, loss-of-function mutations in *TOE1*, resulting in the accumulation of incompletely processed snRNAs (**Figure 1.3C and 1.5C**). TOE1 is associated with pre-snRNAs and snRNAs associated with TOE1 DE-mutant, U1, U2, and U5 snRNAs contained longer tails than those associated with WT TOE1, and this effect can be rescued with exogenous WT TOE1, suggesting that TOE1 plays a role as a 3'-5' exonuclease for specific snRNA processing [32]. There was an increase in the fraction of U1 and U2 snRNAs, and to a less extent, U5 snRNAs containing tails in patient-derived fibroblast and NPC lines compared to unaffected relatives, suggesting that there might be a link between the cause of PCH7 and a key factor involved in incompletely processed snRNAs which are likely caused by loss-of-function TOE1 mutants [32].

TOE1 and PARN may act non-redundantly on regulating and maintaining hTR biogenesis in diseases (**Figure 1.3B**). It is interesting to note that cerebellum hypoplasia also manifests in patients with telomere-related diseases, such as Hoyeraal-Hreidarson and Revesz syndromes [160,161]. It has been shown that TOE1 deficiency leads to the accumulation of hTR precursors, including oligoadenylated and 3' end extended forms. However, TOE1 deficiency only affects telomerase activity and the shortening, but not hTR levels [34]. The current model speculated that most of the hTR poly(A) tails are removed by PARN in the nucleoli, then hTR transits to Cajal bodies for further processing by TOE1 and/or PARN, cooperative or sequentially [34]. This explains why when TOE1 is deficient, there are more immature hTR precursors but no decrease in total hTR levels. Thus, understanding the precise mechanisms of how these deadenylases function may give insights into the development and pathogenesis of diseases such as DC and PCH7.

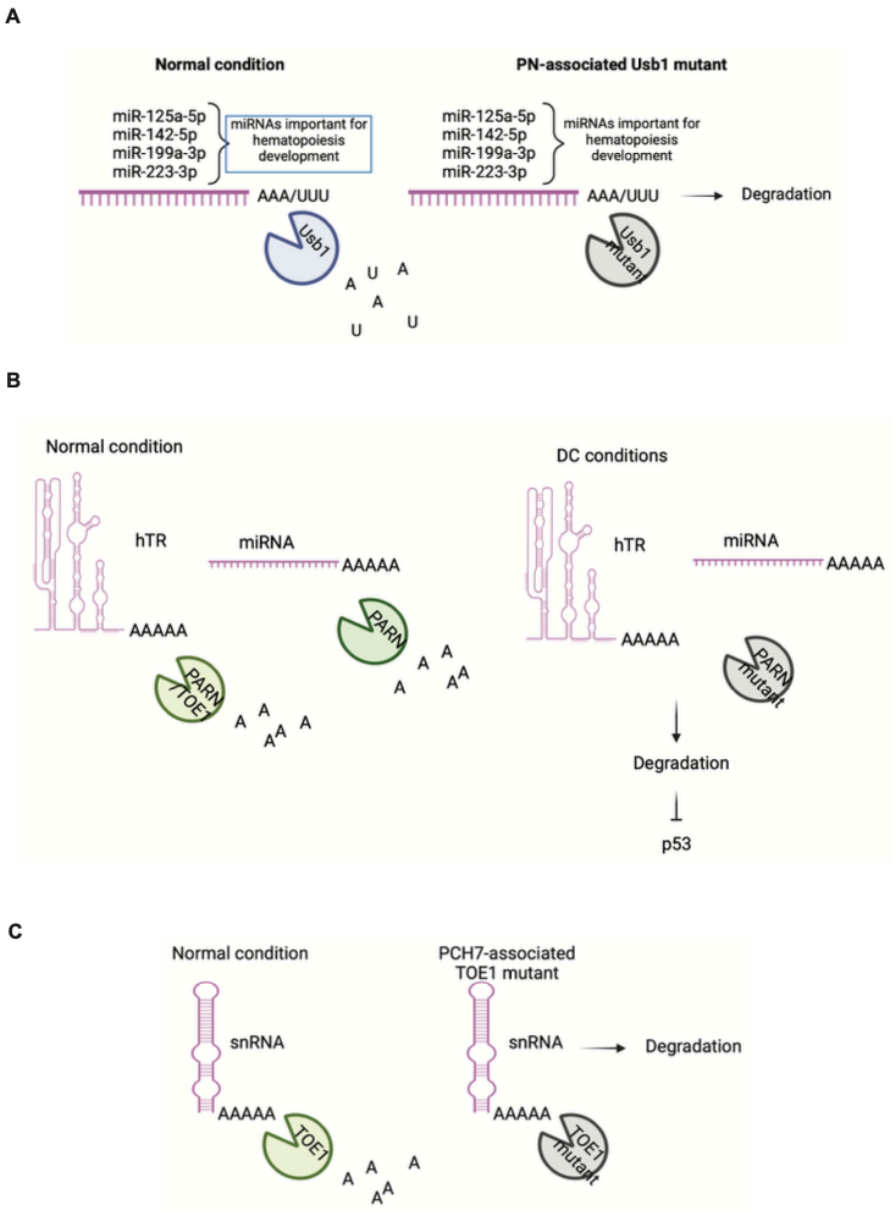

Figure 1.5. Model depicting the regulation of ncRNA stability through ribonucleases in different diseases.

(**A**) miRNAs that are important for hematopoiesis development are stabilized by Usb1 in normal condition while are targeted for degradation in Poikiloderma with Neutropenia disease where Usb1 is mutated [31]. (**B**) hTR and miRNAs are stabilized by PARN and/or TOE1 in normal condition while are targeted for degradation in Dyskeratosis Congenita disease where PARN is mutated [22,24,25-27,34,38-41,47]. (**C**) snRNAs are stabilized by TOE1 in normal condition while are targeted for degradation in Pontocerebellar Hypoplasia 7 where TOE1 is mutated [32].

Inhibition of PAPD5/7 may be a potential therapy for PN and DC. Dysregulated miRNA and hTR levels in Usb1 and PARN mutants contribute to hematopoietic failure, due to a failure to remove 3' end adenylated tails added by PAPD5/7. Previous studies showed that modulation of miRNA 3' end adenylation through genetic or chemical inhibition of PAPD5/7 rescues hematopoietic in Usb1 mutants [31]. Likewise, PAPD5 KD can rescue telomerase activity in PARN-deficient cells and restore defects in hematopoiesis [22,162]. Though there is no data of how PAPD5/7 affects snRNAs and PCH7 phenotypes, these studies suggest that inhibitors of PAPD5/7 might be a potential treatment for PN and DC, and possibly PCH7.

1.4. Regulation of RNAs in RNP granules

1.4.1. General properties of RNAs in RNP granules

RNAs are needed for the formation of SGs and other RNP assemblies such as PBs and paraspeckles. For example, the transcription and presence of *NEAT1* lncRNA are required for paraspeckle formation [163,164]. Likewise, SGs and PBs require nontranslating mRNAs for their formation since limited translation initiation and ribosome runoff are required for SG assembly and accumulation while trapping mRNAs in polysomes reduces SG assembly [165-169]. The common model for how RNAs contribute to RNP granule assembly is that RNAs offer direct RNA-RNA interactions and provide scaffolds for multi-valent RBPs to form individual RNPs, which through RNA-RNA, RNA-protein, and protein-protein interactions, link together into higher order assemblies and form RNP granules [51].

Recent studies of SG transcriptome from yeast and mammalian cells have revealed the nature of mRNAs in SGs. A study showed that >99% of individual mRNA species can go to SGs although the targeting efficiency varies from <1% to >95% [170]. It has been shown that globally, mRNAs with longer coding and UTR regions and poor translatability accumulate to a higher degree in SGs, and have longer interaction times with SGs than shorter transcripts [170-172]. Likewise, mammalian SG-enriched non-coding RNAs (ncRNAs) tend to be longer compared to SG-depleted ncRNAs [170]. The same principle is applied to mRNA accumulation in other RNP assemblies such as PBs and P-granules [173-175]. This suggests a model wherein long mRNAs that exit translation can form numerous interactions with other long non-translating mRNAs, leading to the formation of SGs. In contrast, it was also shown that membrane association limits SG partitioning of mRNAs [170]. Specifically, they observed that SG-enriched mRNAs in both yeast and human are distinct from the subset of mRNAs encoding proteins that localize to the mitochondria. This suggested that mRNA localization to other organelles may preclude mRNA from efficiently accumulating in SGs.

1.4.2. RNAs can be recruited to SGs by RNA-binding proteins

SGs contain a diverse proteome including vast numbers of RNA-binding proteins (RBPs). SGs are thought to contain a highly dynamic ‘shell’-like region that surrounds a highly stable ‘core’ region. Purification and proteomic analysis of SG cores led to the discovery of a diverse SG proteome consisting of numerous RBPs which form a dense protein-protein interaction network [176]. This suggests that the recruitment of proteins to

SGs is through protein-protein interactions, which may also recruit RNA bound to those RBPs.

Proteins have also been shown to interact with RNA and form other assemblies. Studies have shown that intrinsically disordered domains in proteins or disordered proteins, such as MEG-3, can interact with RNAs and form RNA condensates *in vitro* [173,177,178]. *In vivo*, P granules are shown to recruit mRNAs by condensation with the disordered protein MEG-3 [173]. These findings reveal that intrinsically disordered proteins can act as drivers of RNA assemblies. Moreover, *in vitro* and *in vivo* experiments indicated that oskar protein interacts with germ-granule-enriched mRNAs *nos*, *gcl*, *pgc*, and its own mRNAs. This suggested that oskar may help recruit mRNAs to germ granules via its RNA-binding domain [179-181].

In line with this, some SG-RBPs such as G3BP and TIA are sufficient to target mRNAs into SGs. Matheny et. al. showed that artificially tethering of G3BP1 and TIA-1, SG proteins, to firefly *luciferase* reporter with a λN-BoxB system increases *luciferase* recruitment to SGs in a dose-dependent manner [50,182]. Moreover, the evidence argues that many interactions are required to get noticable changes in SG enricment and RNA enriching in SGs. This suggests that targeting mRNPs to SGs is likely a summation of multiple interactions. This study also suggests that individual protein interactions have little effects on RNA partitioning to SGs, which is supported by no statistical difference between SG transcriptomes of wild-type and double knockout G3BP1/2 cells. Together, this study provided the first demonstration showing that RBPs can target mRNAs to SGs.

In constrast to the model proposed in Matheny et. al., recent papers proposed that N^6-methyladenosine (m6A) modifications can enhance the phase separation potential of mRNAs and SG formation [50,183,184]. m6A is the most prevalent modified nucleotide in mRNA, with roughly 25% of mRNAs containing at least one m6A [183,185,186]. Ries et. al. showed that m6A RNAs enhance liquid-liquid phase separation (LLPS) of the m6A-reader proteins, YTHDF proteins [183]. The papers suggested a model wherein m6A-binding YTFDH proteins can bind to the polymethylated transcript and increase the valency of that transcript, thereby increases its accumulation in SGs [183,184].

However, these findings that m6A acts as a dominant element driving mRNAs to SGs are controversial. Even though m6A is the most prevalent modification of mRNAs, the degree of modification on individual mRNAs is suspected to barely affect their localization to SGs based on Matheny et. al. model. For example, U-2 OS m6A mapping data set showed that the number of mapped m6A sites/gene is less than 13 with most genes having only 1-3 mapped sites [187]. Based on these numbers, the model would predict that m6A is not likely to play a major role in targeting RNAs to SGs. Moreover, Ries et. al. and Fu and Zhuang both showed a correlation between numbers of m6A on transcripts and SG enrichment of those transcripts [183, 184]. It is noted that SG enrichment is correlated with length and number of m6A sites is also correlated with length. Thus, when normalized with length, Khong et. al. showed there is a negative correlation [188]. Additionally, in cells lacking m6A methylation due to a knockout of METTL3, a m6A writer protein, there are minimal changes in SG accumulation of all polymethylated,

monomethylated, and unmethylated transcripts [188]. This latter observation argues that m6A has little or no effect on RNA partitioning to SGs.

1.4.3. RNAs can be targeted to SGs via RNA-RNA interactions

An additional possibility for RNA targeting to SGs is through RNA-RNA interactions. Recent studies showed that globally, longer transcripts accumulate to a higher degree in SGs, and have longer interaction times with SGs than shorter transcripts [170-172]. One explanation is that long RNAs accumulate in SGs because they can form more specific and non-specific RNA-RNA interactions in *trans* [189]. This is suggested by 1) RNA can robustly form assemblies *in vitro*, even in the absence of protein, and these assemblies largely recapitulate the SG transcriptome [189,190]. 2) There is a limited correlation of the binding of SG proteins and RNA enrichment in SGs [170]. 3) The *NORAD* lncRNA, which contains at least 17 SG-component, Pumilio, binding sites, accumulates in SGs independent of Pumilio [171,191]. 4) The abundant RNA helicase eIF4A can limit RNA assembly and SG formation potentially by limiting thermodynamically favored intermolecular RNA-RNA interactions [192].

RNA-RNA interactions required for RNA targeting to RNP assemblies can be specific and unspecific [51,193]. Langdon et. Al. Showed that aspects of RNA secondary structure can affect the specificity of RNA targeting to RNP granules in *Ashbya gossypii* [193]. Moreover, specific base-pairing *in trans* between *oskar* mRNAs and *bicoid* mRNAs are required for their recruitment to RNP granules during *Drosophila* oocyte development [194,195]. Likewise, partial complementarity between piRNAs and target mRNAs is sufficient

to initially recruit and anchor a variety of transcripts in germ granules [196]. In contrast, SGs, PBs, and P-granules are heavily biased toward longer mRNAs, it is possible that some RNP granules may form in part through random interactions between RNAs. An average length of mRNAs to be enriched in SGs is ~7.5 kb [170,171,173-175]. One can estimate that a 7.5 kb mRNA would have approximately 14,000 possible 6 base pair interactions of perfect complementation simply by chance [51].

1.4.4. SGs are formed by a summation of multiple interactions

Recent studies raised the hypothesis that when translation initiation is limited, RNAs are released from ribosomes which creates a large pool of “naked” RNA that forms multivalent interactions with other RBPs and RNAs and promote RNP assemblies. For example, SG, PB, and P-granule transcriptomes all favor longer RNAs that are ribosomes depleted [170,171,173-175]. These observations suggested that longer RNAs simply have more sites for RBP binding and/or RNA-RNA interactions to promote RNP granule formation. Moon et. al. showed that both translating and untranslating mRNAs can interact with SGs [172]. While translating mRNAs interact transiently with SGs, untranslating mRNAs exhibit both stable and transient interaction with SGs. Similarly, Pitchiaya et. al. Demonstrated that translation potential of an mRNA inversely correlates with PB localization [198]. In model assemblies, exchange rates of the component are dependent on both the strength of individual interactions and their valency, with higher valency having more stable interactions [197,198]. Altogether, these data supported the model wherein untranslating mRNAs can form more multivalent interactions and promote their association with RNP granules.

1.4.5. SG and other RNP granule formation is expected to affect mRNA regulation

mRNAs are exchangeable between SGs and PBs. PBs and SGs are two cytoplasmic mRNP granules which can dock and/or overlap in both yeast and mammalian cells [167,199]. A general model is that after translational shutoff, mRNAs first associate with SGs, and then can be sorted to targeting PBs [199]. In contrast, mRNAs have been proposed to move from PBs to SGs upon glucose deprivation in yeast [200]. Multicolor single-molecule imaging revealed that mRNAs that interact transiently with PBs can interact transiently with SGs and vice versa, indicating that there is no specific order of RNA transport from one granule to another. This finding also suggested that an individual mRNA and its associated proteins can interact with either SGs or PBs, or exchange proteins that enables SGs and PBs interaction within seconds [172]. Moreover, mRNAs within PBs can be targeted for decapping and degradation but mRNAs can also be degraded outside of PBs [201]. These observations suggested a dynamic mRNA cycle wherein mRNPs can be remodeled within these assemblies and exchange between SGs and PBs. During RNP granule disassembly, mRNPs within these granules can return to translation or be targeted for autophagy, another system for SG clearance [60,202,203].

SGs are proposed to affect the biological reactions by limiting the interactions of sequestered components with their targets. For example, Laver et. al. showed that in unstressed cells, *Drosophila* G3BP Rasputin (RIN) associates with polysomes and stabilize and upregulate the translation of its target mRNAs [204]. They proposed a model where incorporation of RIN/G3BP into SGs sequesters them away from their short target mRNAs, thus downregulates the expression of these transcripts. Moreover, SGs are

suggested to sequester UBAP2L, an negative regulator of paraspeckle formation, thus regulate their assembly [205].

On the other hand, some RNP granules, such as germ and neuronal RNP granules, can serve as RNA storage sites and play roles in controlling cell fate specificity, RNA transport and localization. For example, in *C. elegans*, P-granules are not essential for translational repression or preferential RNA stability [173]. They are thought to act as a storage for enrichment of maternal mRNAs in the germline founder cell P4 to maximize robustness of germ cell fate specification [173]. Similarly, neuronal RNA granules are suggested to be a local storage compartment for local mRNAs under translational arrest but poised for release to actively translated pool [58]. The local release of mRNAs from the granules may serve as a macromolecular mechanism linking RNA localization to translation and synaptic plasticity [58]. Moreover, RNA granules are shown to hitchhike on moving lysosomes for long-distant transport using annexin A11 protein as a molecular tether and knocking down of this protein reduces delivery of essential mRNAs to distal region of the neuron, suggesting that impaired RNA transport could, over time, affect the synaptic activity [206].

1.5. Conclusions

RNA regulation control can be achieved through multiple pathways, including RNA localization and/or specific ribonucleases such as Usb1, PARN, and TOE1. RNA dysregulation is involved in cell survival, developmental defects in animals, and various human diseases. Therefore, studying the mechanisms of how RNAs are regulated is

crucial for fundamental understandings of numerous biological processes and may provide insights into potential therapeutic treatments for certain diseases.

CHAPTER II

RNA partitioning into stress granules is based on the summation of multiple interactions

Contribution statement: This chapter is adapted from the following manuscript which was co-first authored with Dr. Tyler Matheny and Dr. Briana Van Treeck and was a highly collaborative manuscript. T.M., B.V.T, T.N.H., and R.P. designed the research, T.M., B.V.T, and T.N.H conducted the experimental research, T.M performed computational analyses of RNA sequencing and mathematical modeling, T.M., B.V.T., T.N.H., and R.P. analyzed the data, T.M., B.V.T., T.N.H., and R.P. wrote the paper.

Matheny T*, Van Treeck B*, Huynh TN*, Parker R. RNA partitioning into stress granules is based on the summation of multiple interactions. *RNA*. 2021 Feb;27(2):174-189. doi: 10.1261/rna.078204.120. Epub 2020 Nov 16. PMID: 33199441; PMCID: PMC7812873. *: Authors contributed equally.

2.1. Abstract

Stress granules (SGs) are stress-induced RNA-protein assemblies formed from a complex transcriptome of untranslating ribonucleoproteins (RNPs). Although RNAs can be either enriched or depleted from SGs, the rules that dictate RNA partitioning into SGs are unknown. We demonstrate that the SG-enriched *NORAD* RNA is sufficient to enrich a reporter RNA within SGs through the combined effects of multiple elements. Moreover, artificial tethering of G3BP1, TIA1, or FMRP can target mRNAs into SGs in a dose-dependent manner with numerous interactions required for efficient SG partitioning, which suggests individual protein interactions have small effects on the SG partitioning of mRNPs. This is supported by the observation that the SG transcriptome is largely unchanged in cell lines lacking the abundant SG RNA-binding proteins G3BP1 and G3BP2. We suggest the targeting of RNPs into SGs is due to a summation of potential RNA-protein, protein-protein, and RNA-RNA interactions with no single interaction dominating RNP recruitment into SGs.

2.2. Introduction

Stress granules (SGs) are ribonucleoprotein (RNP) assemblies that form during stress when translation initiation is limited [53,207]. SGs are of interest because they play roles in the stress response, are related to similar RNP granules in neurons and embryos, share components with toxic aggregates observed in degenerative disease, and affect viral infections as well as cancer progression [62,63,208-211].

Based on super-resolution microscopy, mammalian SGs formed during arsenite stress are non-uniform in nature and contain local regions of protein and RNA concentration, referred to as SG cores [176,212,213]. In addition to this imaging criteria, cores are defined by their biochemical stability in cell lysates [176,213]. This has allowed for SG core purification from U-2 OS cells expressing GFP-G3BP through differential centrifugation and GFP pulldown [214,215]. Purification of SG cores led to the discovery of a diverse SG proteome composed of numerous RNA-binding proteins (RBPs) forming a dense protein-protein interaction network [176]. Similar SG protein composition was also detected by proximity labeling methods [216,217]. The fact that SGs include a protein-protein interaction network is consistent with the recruitment of proteins to SGs through protein-protein interactions, which might recruit specific mRNAs bound to those RBPs.

An additional possibility is that RNA-RNA interactions contribute to defining the RNA composition of SGs. Consistent with this model, the transcriptome of protein-free *in vitro* RNA assemblies, formed from total yeast RNA, shows remarkable overlap with the transcriptome of yeast SGs [189]. Moreover, the abundant RNA helicase eIF4A functions to limit RNA condensation and SG formation by binding RNA [192]. This suggests a model wherein RNPs are partitioned into SGs by both RNA-RNA and protein-protein interactions [51].

A striking feature of the SG transcriptome is that there are dramatic differences in the partitioning of RNPs into SGs. For example, RNA sequencing of immunopurified SGs revealed that some RNAs, such as *AHNAK* or *NORAD*, are strongly enriched in SGs,

while other mRNAs, such as *GAPDH*, are largely depleted from SGs [170]. Differential partitioning of RNPs into SGs and/or P-bodies has also been seen when RNP granules are fractioned based on particle sorting or differential centrifugation [171,174,175]. These analyses revealed that long, poorly translated transcripts preferentially enrich in SGs [170], that AU-rich elements correlated with SG granule fractionation [171], and that decreased translational efficiency correlated with increased SG and P-body enrichment [170,174,175]. Taken together, these observations suggest that partitioning of RNPs into SGs could be promoted by protein- or RNA-based interactions, affected by overall length of the RNA, and inhibited by the association with ribosomes. However, the relative importance of these interactions, their required valency, and how they might contribute to the RNA composition of, and organization within, SGs is unknown.

Herein, we examine the rules that affect the partitioning of RNAs into SGs. We first show enrichment into SGs is a dominant property as a chimera between the highly enriched *NORAD* RNA and a SG excluded reporter RNA is enriched in SGs. Deletion analysis revealed the enrichment of *NORAD* in SGs is due to multiple sequence elements that act in an additive manner. In addition, we examined how proteins influence the recruitment of RNAs to SGs by determining how tethering of RBPs found in SGs to a reporter transcript affects mRNA enrichment in SGs and how deletion of the major SG RBPs G3BP1 and G3BP2 affects RNA recruitment to SGs. We show that artificially tethering multiple G3BP1, FMRP, or TIA1 proteins to a *luciferase* reporter transcript increases the SG localization of a *luciferase* RNA reporter in a dose-dependent manner. However, based on curve fitting of these tethering experiments, we predicted that removal

of G3BP proteins from the cell would only have a limited effect on the RNA composition of SGs. Testing this hypothesis, we demonstrate that the RNA composition of sorbitol-induced SGs is very similar in wild type (WT) and ΔΔG3BP1/2 cell lines. Taken together, our results indicate that while G3BP1 binding can promote RNA targeting to SGs, it is not required for SG localization. We suggest a model in which RNA localization to SGs arises through the summation of many RNA-RBP and RNA-RNA interactions, which each individually play a small role in localization, but through synergistic effects lead to the observed RNP partitioning into RNP granules.

2.3. Results

Luciferase mRNA as a reporter for SG partitioning in mammalian cells

The firefly *luciferase* was used as an RNA reporter to assess how different elements affect RNP partitioning into SGs for two reasons. First, *luciferase* is not endogenous in mammalian cells, thus, we can eliminate the endogenous background in our analysis. Second, single molecule fluorescent *in situ* hybridization (smFISH) analyses revealed that *luciferase* mRNA is poorly enriched in SGs, with approximately 15% of its cytoplasmic RNA molecules in SGs upon an hour of sodium arsenite treatment (**Appendix Figure A.1**). Using this reporter system, with a downstream SV40 poly(A) signal, we examined how adding sequences or binding sites for RBPs affected SG partitioning.

NORAD RNA contains dominant elements that dictate SG partitioning

While it is assumed that partitioning of RNPs into SGs is a dominant trait, to our knowledge this has never been tested. To determine if SG partitioning is a dominant trait we inserted the SG-enriched *NORAD* RNA into the 3' UTR of the *luciferase* reporter mRNA. As assessed by smFISH, we observed that ~71% of the chimeric *luciferase-NORAD* RNAs were recruited to SGs, similar to the endogenous *NORAD* RNA (76.7%) and significantly increased compared to the *luciferase* reporter (16.7%) (**Figure 2.1A-C**). Thus, SG recruitment of RNPs is a dominant property of non-translating, cytoplasmic RNAs.

To determine whether one or more elements in the *NORAD* RNA were promoting SG partitioning, we constructed *luciferase* mRNAs with either each half, each of the four quarters, or each eighth of the *NORAD* RNA inserted into the same site in the 3' UTR.

We observed that essentially any piece of *NORAD* could increase the recruitment of the *luciferase* reporter into SGs with the average increase correlating with the size of the insert (**Appendix Table A.1**). For example, either half of *NORAD* yielded ~60% reporter enrichment within SGs, each quarter gave between ~55% and 35% recruitment, and each eighth gave between 22% and 50% recruitment (**Appendix Table A.1**). These increases are not solely due to increased length since insertion of additional luciferase sequences of similar lengths in the same position within the 3' UTR gave only limited increases in SG recruitment (**Appendix Table A.1**). Indeed, the relationship between length and SG enrichment only gave a small positive slope, suggesting that length, per se, is not the major driving force in SG enrichment and that the previously defined length

dependence is likely due to long transcripts harboring more RBP sites and/or RNA-RNA interaction motifs. Similarly, insertion of antisense sequences from *NORAD* typically resulted in less recruitment of the reporter into SGs than corresponding sense-strand inserts (**Appendix Table A.1**). The limited correlation with length is consistent with the SG transcriptome in which there is an overall length determinant, however mRNAs of similar length can show differences in their partitioning into SGs [170]. This suggests that *NORAD* contains multiple sequence-specific elements, independent of overall length, that can increase partitioning into SGs. These elements may increase SG localization through interaction with multivalent RBPs, or through increased propensity of these RNA sequences to undergo RNA-mediated assembly.

We compared the features of the *NORAD-luciferase* chimeric RNAs to determine if any feature strongly correlated with SG enrichment. We observed only a limited correlation between SG recruitment and length or GC content (**Appendix Figure A.2**). In the *NORAD* RNA there are 13 AU-rich elements (AREs) with an AUUUA motif and 19 Pumilio recognition elements (PREs), which can bind Pumilio and other RBPs [191,218]. We observed some correlation of SG enrichment in each construct with either the numbers of AREs, PREs, or their summation (**Figure 2.1D-F**). There are likely multiple RBP binding sites in these segments that lead to differential localization. The presence of correlation implied that ARE- and PRE-binding proteins may contribute to the SG enrichment of *NORAD*.

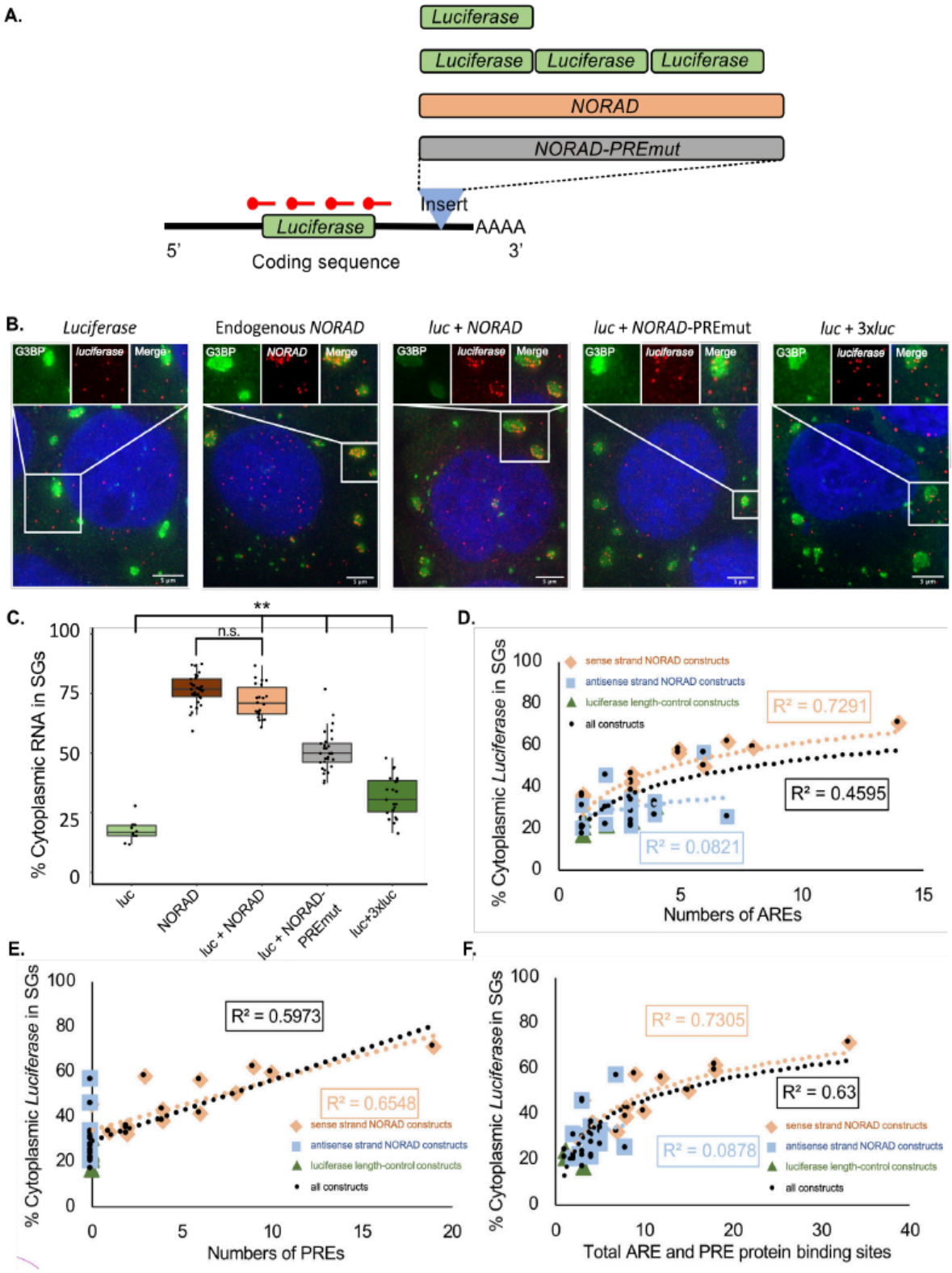
A.
Luciferase
Luciferase
Luciferase
Luciferase
NORAD
NORAD-PREmut
Insert
Luciferase
AAAA
5'
Coding sequence
3'
B.
Luciferase
Endogenous NORAD
luc + NORAD
luc + NORAD-PREmut
luc + 3xluc
G3BP
luciferase
NORAD
Merge
C.
% Cytoplasmic RNA in SGs
**
n.s.
luc
NORAD
luc + NORAD
luc + NORAD-PREmut
luc+3xluc
D.
% Cytoplasmic Luciferase in SGs
Numbers of AREs
sense strand NORAD constructs
antisense strand NORAD constructs
luciferase length-control constructs
all constructs
R² = 0.7291
R² = 0.4595
R² = 0.0821
E.
% Cytoplasmic Luciferase in SGs
Numbers of PREs
R² = 0.5973
R² = 0.6548
F.
% Cytoplasmic Luciferase in SGs
Total ARE and PRE protein binding sites
R² = 0.7305
R² = 0.63
R² = 0.0878

Figure 2.1. *NORAD* increases *luciferase* RNA enrichment within SGs.

(**A**) Cartoon depicting chimeric *luciferase* reporter constructs with different inserts in the 3' UTR. PREmut is the *NORAD* sequence with 18 of the PREs mutated. The 3x luciferase was inserted as an approximate length control for *NORAD*. (**B**) smFISH of *luciferase* RNA for different constructs during arsenite stress. The endogenous *NORAD* RNA was imaged with smFISH probes to *NORAD*, all other constructs were imaged with smFISH probes to *luciferase*. Scale bar = 5 μm. (**C**) Boxplot of the enrichment of endogenous *NORAD* and luciferase with different 3' UTR inserts in SGs. **$p<1\times10^{-4}$. Each dot represents a single cell. (**D**) Correlation between SG enrichment and number of AREs. (**E**) Correlation between SG enrichment and number of PREs. (**F**) Correlation between SG enrichment and total number of AREs and PREs. For (**D**-**F**): Orange diamonds are sense-*NORAD* constructs, light blue squares are antisense-*NORAD* constructs, dark green triangles are luciferase length control constructs, and black circles are all the constructs.

To test whether the 19 PREs are important for *NORAD* recruitment in SGs, we generated a chimeric mRNA with the *NORAD* sequence with 18 PREs mutated to limit Pumilio (and possibly other proteins) binding, into the *luciferase* 3' UTR. We observed a significant decrease in *luciferase* reporter, from 71% to 50%, in SGs (**Figure 2.1B and C**). Since cells lacking Pumilio proteins can still robustly accumulate *NORAD* in SGs [171], this suggests that the PREs can promote SG enrichment either as an RNA element, or potentially by binding other RBPs in addition to Pumilio, such as SAM68, which has binding sites in or near many of the PREs [219].

Taken together, these observations argue that *NORAD* contains multiple elements that can increase an mRNAs partitioning into SGs. Moreover, the correlation of enrichment with protein binding sites suggests that at least some of the SG enrichment will be due to RBPs targeting mRNAs to SGs.

Tethering G3BP1 to a reporter mRNA increases the reporter RNA's enrichment within SGs

To directly examine how the interactions with mRNA-binding proteins affect mRNA partitioning into SGs, we next focused on G3BP1 for three reasons. First, G3BP1 is one of the most abundant cytoplasmic RBPs [182]. Second, G3BP1 partitions strongly into SGs [214]. Third, G3BP1, and its paralog G3BP2, are required for SG formation under certain stresses [220,221]. We hypothesized that if protein-RNA interactions of RBPs play a critical role in localizing transcripts to SGs, increasing the number of G3BP1 molecules bound to

a specific mRNA by artificial tethering should lead to increased targeting of that mRNA to SGs.

To determine if G3BP1 could increase a given RNA's localization to SGs, smFISH was used to monitor localization of the *luciferase* RNA reporter with and without G3BP1 tethering sites. We used the λN-BoxB system to artificially tether G3BP1 to the *luciferase* mRNA [222]. λN was fused to G3BP1-GFP as well as a GFP control (**Figure 2.2A**). *Luciferase* mRNA reporters were created with 0, 7, and 25, BoxB sequences in their 3' UTR and were genomically incorporated into the AAVS locus of U-2 OS cells (**Figure 2.2A**). Reporter RNA localization was assayed in cells transfected with either G3BP1-GFP-λN or GFP-λN and in non-transfected cells.

A key observation was that upon mild to moderate G3BP1-GFP-λN expression, *luciferase* RNAs with 7 or 25 λN binding sites shifted *luciferase* from a median of 14% partitioning in SGs to ~36% or ~62% partitioning, respectively (**Figure 2.2B-D**). Notably, this effect is dose-dependent since mRNAs with 25 BoxB sequences showed increased SG partitioning as compared to mRNAs with 7 BoxB sequences (**Figure 2.2B and D**). Addition of BoxB repeats to *luciferase* did not affect RNA partitioning to SGs when expressed without any λN protein or when co-expressed with GFP-λN (**Figure 2.2B**). Thus, the observed effect is due to the ability of the transcript to interact with G3BP1 and is not simply due to the increased length of the transcript. Examination of individual transfected cells showed that the reporter partitioning into SGs was similar over a range of G3BP1 concentrations (**Appendix Figure A.3**), suggesting the effect is not a result of

G3BP1 overexpression. Cells that highly over-expressed G3BP1, which leads to the formation of constitutive SGs [220], were not included in this analysis. Taken together, these observations demonstrate that, at least during arsenite stress, the presence of multiple G3BP1 proteins on an mRNP can alter the partitioning of that mRNA to SGs in a dose-dependent manner. Therefore, at least some SG RBPs can influence the partitioning of client RNAs to SGs.

To determine if this effect was unique to G3BP1-GFP-λN, we also tethered GFP-λN or Halo-λN tagged versions of the stress granule components TIA1 or FMRP, and a G3BP1-Halo control to *luciferase* mRNAs with 5, 7, or 25 BoxB sites. We observed that TIA1 and FMRP could recruit the reporter mRNA into SGs to the same extent as G3BP1 and with a similar dose dependent effect (**Figure 2.3**). We observed that tethering FMRP to an mRNA with 25 boxB sites also increased SG partitioning, but there was also a decrease in the number of RNAs we could examine, making this observation of less confidence. This observation suggests that some SG-enriched RBPs can actively recruit client RNAs to SGs or, by creating a high local concentration of SG components and RNA, seed SGs.

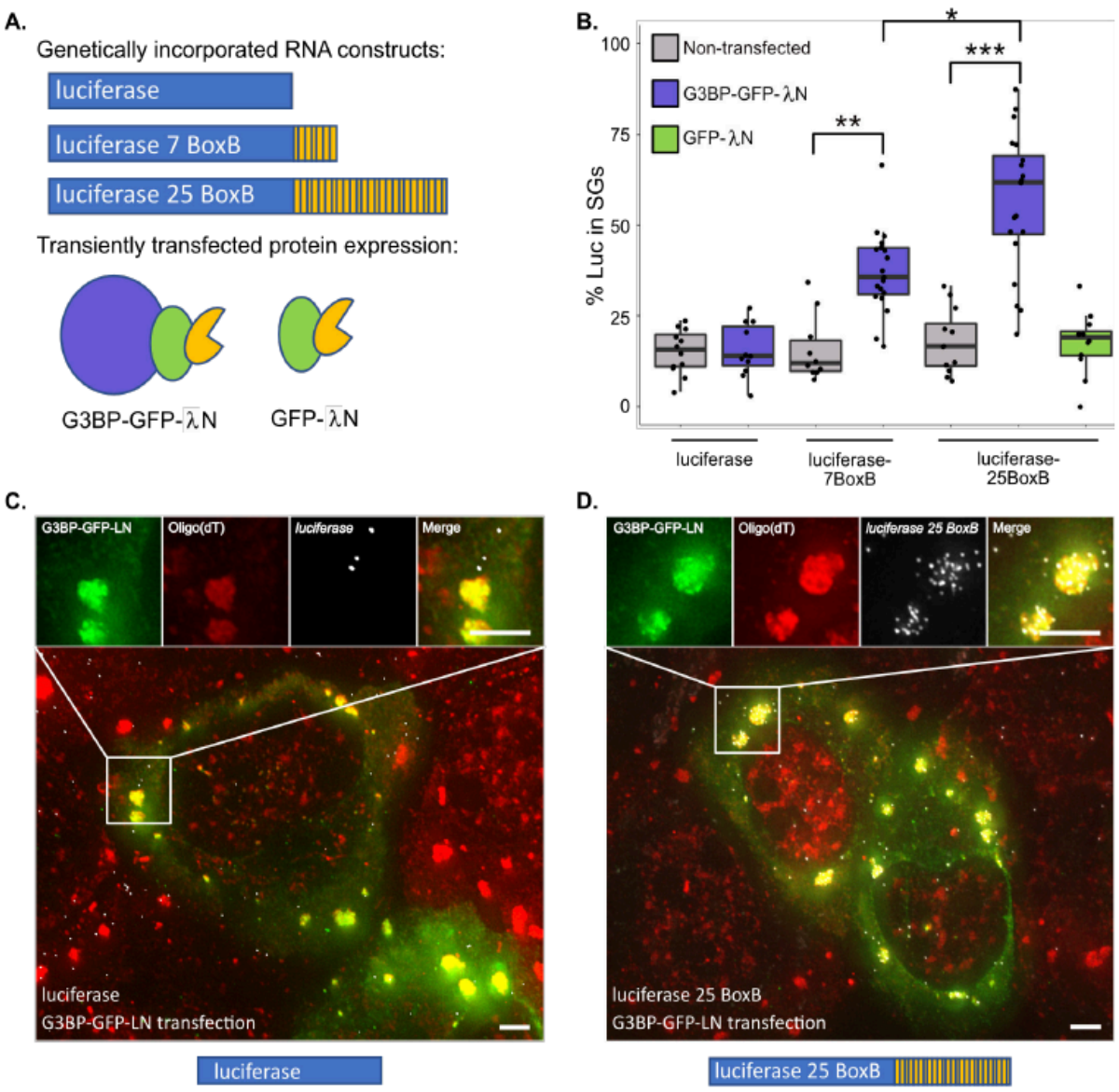

Figure 2.2. G3BP tethering increases *luciferase* RNA enrichment within SGs.

(**A**) *Top:* Cartoon depicting genomically incorporated *luciferase* RNA constructs with 0, 7, and 25 BoxB sites in the 3'UTR. *Bottom:* Cartoon depicting G3BP-GFP-λN and GFP-λN used in tethering experiments. (**B**) Boxplot of the enrichment of *luciferase* 0 BoxB, 7 BoxB, and 25 BoxB RNA in non-transfected, G3BP-GFP-λN and GFP-λN transfected cells. *p<0.001, **p<1×10^{-4}, ***p<1×10^{-7}. Each dot represents a single cell. (**C**) smFISH of *luciferase* RNA in G3BP-GFP-λN transfected cells during arsenite stress. Scale bars = 2 μm. (**D**) smFISH of *luciferase* 25 BoxB RNA in G3BP-GFP-λN transfected cells during arsenite stress. Scale bars = 2 μm.

Quantitative estimation of the number of SG interactions with mRNAs

Based on our G3BP1 and TIA1 tethering experiments, we performed mathematical modeling of SG recruitment as a function of the number of RNA-RBP interactions. In our modeling, for a first approximation, we assume all BoxB sites are occupied by G3BP-GFP-λN or TIA1-GFP-λN. Thus, the unmodified *luciferase* reporter mRNA has an unknown number of interactions, *n*, with SGs, and each BoxB-luciferase reporter has a number of SG interactions that is equal to the sum of the unmodified luciferase SG interactions, *n*, and the number of BoxB sites on that transcript.

We performed curve fitting analysis allowing *n* to vary from 1 to 10 *luciferase* interactions with SG RBPs prior to the addition of any BoxB sequences. Upon qualitative examination of the data, and given the implicit ceiling of 100% enrichment, we reasoned that a non-linear fit would be most appropriate **(Appendix Figure A.4A and B)**. To estimate pearson's r value for each fit, we linearized the data by performing a logarithmic transformation **(Appendix Figure A.4C and D)**. For both TIA1 and G3BP tethering experiments, curve fitting yielded a fit that showed a maximum R value of for the fit in which n = 2 (**Figure 2.4A and B**). We observed similar curves for both G3BP1 and TIA1, suggesting that these two proteins have a similar ability to concentrate client RNAs withing SGs **(Figure 2.4C and D).**

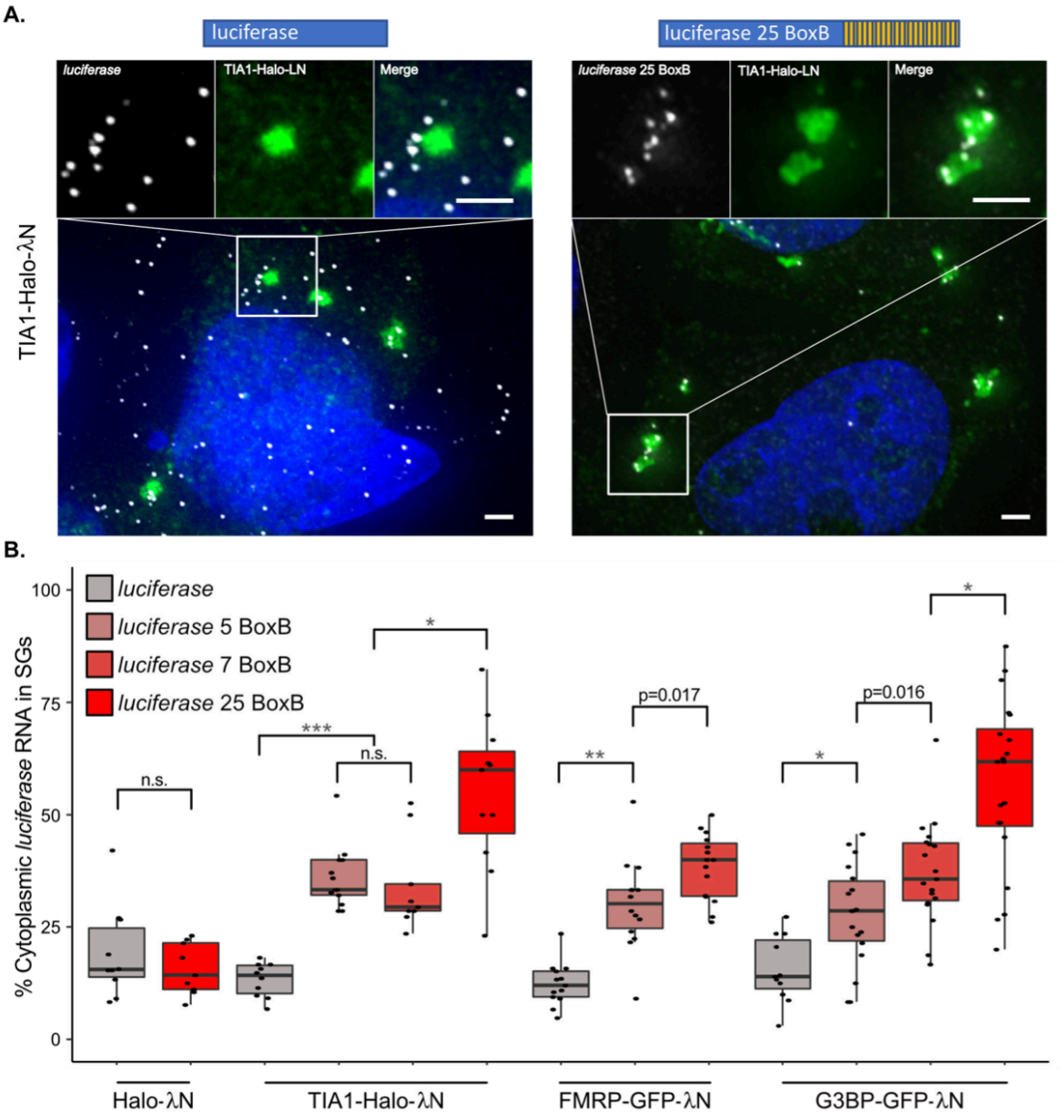

Figure 2.3. Tethering of TIA1, FMRP, or G3BP increases *luciferase* RNA enrichment in SGs.

(**A**) smFISH of *luciferase* and *luciferase* 25 BoxB RNA co-expressed with TIA1-Halo-λN. Scale bars = 2 μm. (**B**) Boxplots depicting enrichment of *luciferase* 0 BoxB, 5 BoxB, 7 BoxB, and 25 BoxB RNA when tethered to G3BP, FMRP, and TIA1 through λN-BoxB interactions. Tethering of Halo-λN to *luciferase* RNA serves as a negative control. *p<0.01, **p<1×10^{-4}, ***p<1×10^{-7}. Each dot represents a single cell.

This analysis highlights a few key principles in RNA recruitment to SGs. First, this result suggests that RNP interactions with a SG will not affect the recruitment of all transcripts to SGs equally. For example, loss of a single SG interaction from an mRNP with 27 total SG interactions would only reduce the expected proportion of mRNAs in SGs from 62% to 61%. In contrast, the loss of one interaction for an mRNP with three SG interactions should reduce its accumulation in SGs from ~18% to ~14%. These observations highlight the key point that RNPs with small numbers of interactions with SGs should be affected to a greater extent by changing a single interaction, while RNPs

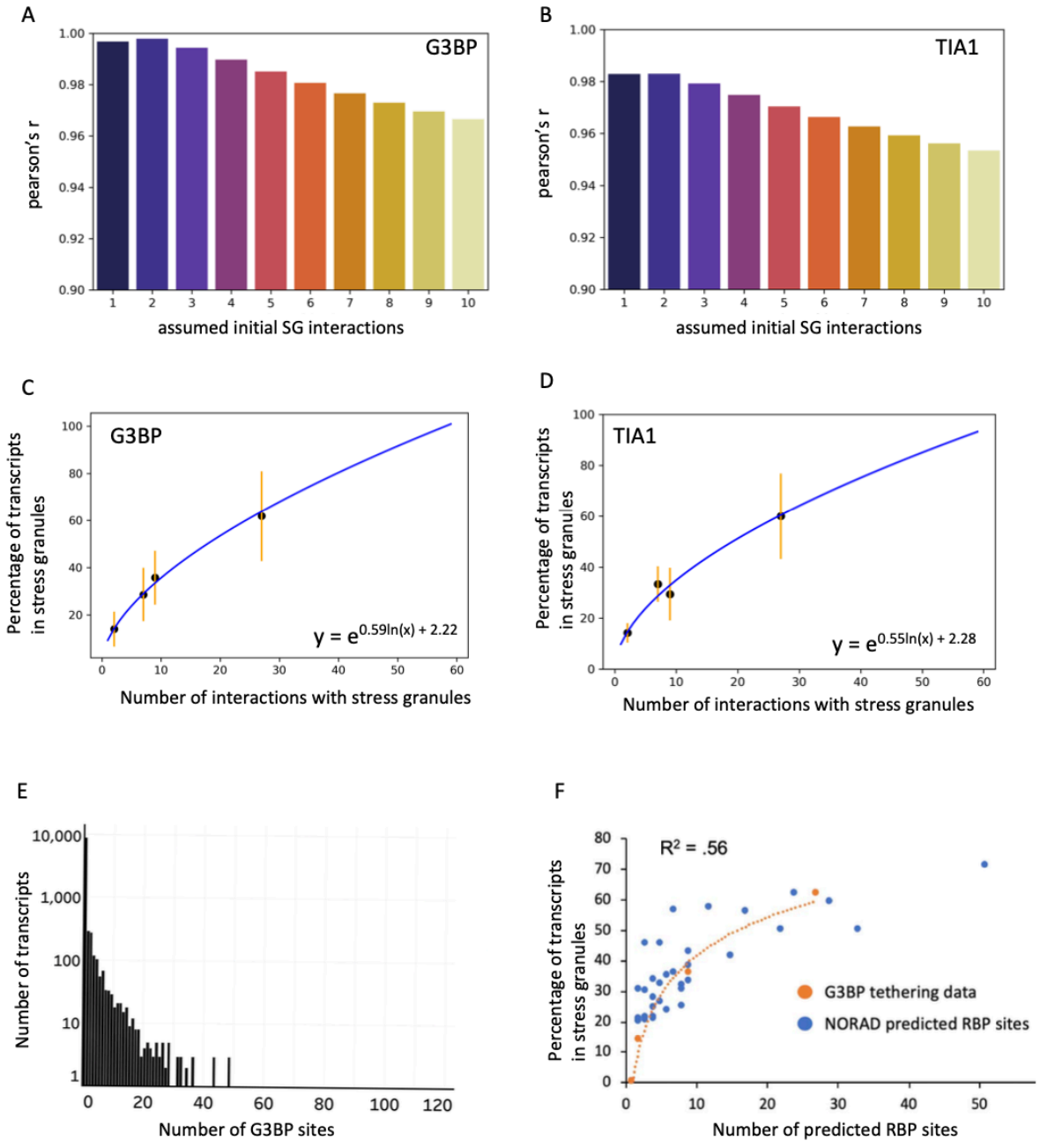
A
G3BP
pearson's r
1.00
0.98
0.96
0.94
0.92
0.90
1 2 3 4 5 6 7 8 9 10
assumed initial SG interactions
B
TIA1
pearson's r
1.00
0.98
0.96
0.94
0.92
0.90
1 2 3 4 5 6 7 8 9 10
assumed initial SG interactions
C
G3BP
Percentage of transcripts in stress granules
100
80
60
40
20
0 10 20 30 40 50 60
y = e^0.59ln(x) + 2.22
Number of interactions with stress granules
D
TIA1
Percentage of transcripts in stress granules
100
80
60
40
20
0
0 10 20 30 40 50 60
y = e^0.55ln(x) + 2.28
Number of interactions with stress granules
E
Number of transcripts
10,000
1,000
100
10
1
0 20 40 60 80 100 120
Number of G3BP sites
F
R² = .56
Percentage of transcripts in stress granules
80
70
60
50
40
30
20
10
0
0 10 20 30 40 50
G3BP tethering data
NORAD predicted RBP sites
Number of predicted RBP sites

Figure 2.4. Mathematical modeling of RBP interactions suggest deletion of G3BP may have a limited effect on RNA enrichment in SGs.

(**A**) Boxplot depicting Pearson's R values for G3BP curve fitting performed using various values of n (initial luciferase-SG interactions prior to the addition of any BoxB sites). (**B**) Same as (**A**), but for TIA1 tethering data. (**C**) Curve of best fit for G3BP data. Black dots represent median values of SG enrichment. Orange error bars represent the standard deviation of the data. (**D**) Curve of best fit for TIA1 data. Black dots represent median values of SG enrichment. Orange error bars represent the standard deviation of the data. (**E**) Histogram depicting the number of transcripts that contain different amounts of G3BP eCLIP peaks. Note that y-axis is on a log scale. (**F**) Curve fitting overlaying the predicted summation of PRE, ARE, and SAM68 sites for NORAD fragment transcripts and G3BP tethering experiments.

with large numbers of SG interactions should be less affected by loss of a single RNA-RBP interaction.

Second, the maximum effect of a given RBP-RNA interaction on SG partitioning should be relatively small, and much less for RNAs which have many non-redundant RNA-RBP interactions. This second observation is important because eCLIP analysis shows that the majority of transcripts in the cell have 0-3 G3BP binding sites (**Figure 2.4E**) [223].

Third, assuming all SG-targeting interactions are similar, one can make an estimate for the number of interactions a given mRNA has with SGs. From this curve, we made a transcriptome-wide first approximation of the number of interactions a given mRNA forms with SGs [50]. Given the assumptions in this model and the cell-to-cell variation in SG enrichment, these numbers should not be taken literally, but should be used as "ballpark" estimates.

One assumption in this modeling is that every BoxB site is directly interacting with a G3BP1 or TIA1 molecule. If we assume that only half of the sites are occupied at a given time, then our estimates for the number of interactions would be correspondingly reduced. However, the logic remains valid that the higher the number of interactions an RNA can form with SGs, the less sensitive that RNA will be to perturbations of individual interactions.

Modeling Explains Behavior of the NORAD-luciferase constructs

To see if we can understand the *NORAD-luciferase* chimeric RNA results in terms of different numbers of RBPs, we first estimated the number of proteins bound to each region (**Appendix Table A.1**). In this analysis, we counted PREs, which serve as binding sites for Pumilio [191,218], AREs, which can bind a diverse number of different ARE-binding proteins and have been shown to correlate with SG enrichment [171], and SAM68 binding sites, which have also been mapped to NORAD [219]. We then plotted the number of predicted RBPs bound to each construct versus the SG enrichment. Remarkably, this set of data points fit the curve derived from the tethered G3BP1 RNAs quite well (**Figure 2.4F**). Moreover, this analysis would predict that the PRE mutant, which has 18 deleted RBP binding sites, should change the recruitment of the *luciferase* reporter from 71% to 61%, near the observed 50%. The deviation between recruitment of the PRE mutant and the predicted value may be due to the PRE mutations disturbing other protein binding sites. Thus, the behavior of both the tethered G3BP1 reporters, and the *luciferase-NORAD* chimeric mRNAs, can be explained as being due to the summation of multiple interactions that together increase the partitioning of RNPs into SGs.

We also estimated the number of RBPs bound to *NORAD* segments based on CLIP sites from a database containing a meta-analysis of RBP CLIP studies (**Appendix Figure A.5A**) [224]. We found that SG RBP CLIP sites showed a qualitative correlation with the enrichment of individual *NORAD* segments within SGs (**Appendix Figure A.5B**), and that when we summed the total number of SG RBPs for each segment of *NORAD* there was a good correlation between SG CLIP sites and *NORAD* segment enrichment

(**Appendix Figure A.5C**). Taken together, these results are consistent with a model in which RBPs can act in tandem to define the RNA composition of SGs.

Loss of G3BP1&2 does not globally affect RNA localization to SGs

Our modeling of SG-mRNA interactions suggests that RBPs act in tandem to contribute to RNP enrichment within SGs. If this model is true, we would anticipate that deletion of individual SG RBPs, such as G3BP, should have a limited effect on the recruitment of transcripts. To test this prediction, we desired to purify and determine the SG transcriptome from cells with and without G3BP1/G3BP2. In order to perform this experiment, we needed to purify SGs using a different SG component than G3BP1, which was used in earlier work [170], and under sorbitol stress condition, where G3BP1 and G3BP2 are not required for SG formation [221]. Thus, we first tested whether immunopurification using an antibody to the SG component PABPC1 yielded a similar SG transcriptome as that seen with GFP-G3BP1 under arsenite stress (**Figure 2.5A-D**) [170].

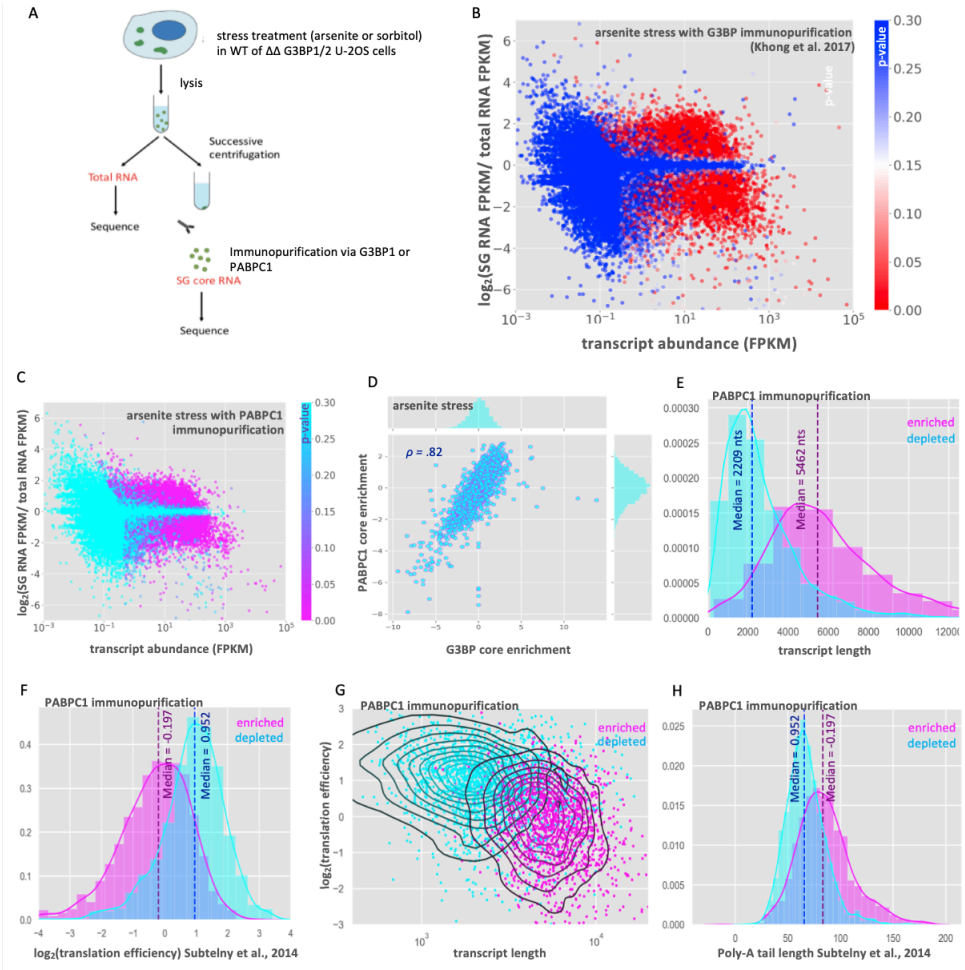

Figure 2.5. RNA-Seq of the PABPC1 stress granule core transcriptome.

(**A**) Schematic of SG core purification strategy in WT or ΔΔG3BP1/2 cells treated with either arsenite or sorbitol stress and using G3BP1 or PABPC1 for immunopurificaiton. (**B**) MA-plot showing stress granule enrichment vs. abundance from previous work examining the SG transcriptome via G3BP1 immunopurification during arsenite stress [170]. (**C**) MA-plot showing stress granule enrichment vs. abundance from PABPC1 immunopurification during arsenite stress. (**D**) Scatterplot of RNA enrichment in PABPC1 cores vs. enrichment in G3BP cores during arsenite stress. (**E**) Histogram showing distribution of SG-enriched and SG-depleted transcripts with respect to transcript length (purified with PABPC1). (**F**) Same as E but for translation efficiency. (**G**) Scatterplot of translation efficiency vs. transcript length with kernel density estimate overlay. Color-coded by enrichment/depletion in SGs. (**H**) Same as E, but for poly-A tail length.

Comparison of the RNAs enriched in SG cores showed that enrichment scores from PABPC1-purified cores and GFP-G3BP1-purified cores had a strong linear correlation (**Figure 2.5D,** Pearson's r = 0.82). Total RNA and SG core purification via PABPC1 pulldown yielded reproducible transcriptomes (**Appendix Figure A.6**). SG RNA transcriptomes based on the purification of SG cores with PABPC1 antibody showed little similarity to total RNA transcriptomes**,** with 3251 transcripts enriched in SGs ($p < 0.01$), and 3693 transcripts depleted from SGs ($p < 0.01$) (**Figure 2.5C**). Thus, PABPC1 pulldown identifies a population of RNAs that strongly overlaps with the SG transcriptome identified by GFP-G3BP1 pulldown. Consistent with PABPC1 and GFP-G3BP1 purification identifying similar RNAs, we observed that in both cases, RNAs enriched in PABPC1-containing SGs are biased towards long, poorly translated RNAs (**Figure 2.5E-G**) [170,225]. Additionally, we observe that enriched RNAs tend to have longer poly-A tails (data obtained from Subtelny et al. 2014) [225], which could be explained by transcripts with longer poly-A tails having less efficient translation rates, lower overall abundance, or by the increased length of these transcripts (**Figures 2.5H, Appendix Figure A.7**) [226]. Taken together our findings suggest that PABPC1 and G3BP1 SG cores share a similar RNA composition and that the RNAs that co-purify with PABPC1 and G3BP1 cores have similar physical properties.

Since ΔΔG3BP1/2 cell lines form SGs during sorbitol treatment, we planned on analyzing SG transcriptomes from sorbitol-treated cells with and without G3BP1/2 expression. Before sequencing PABP-containing SGs from WT and ΔΔG3BP1/2 cells during sorbitol stress, we first examined whether the RNA composition of sorbitol-induced

SGs was similar to arsenite-induced SGs. Thus, we compared the transcriptome of SG cores purified via PABPC1 and GFP-G3BP1 immunopurification during hyperosmotic stress induced by sorbitol (**Figure 2.6, Appendix Figure A.8 and A.9**) [221,227].

Purification of GFP-G3BP1 SGs under sorbitol stress yielded a very similar transcriptome to that observed under arsenite stress**,** with 2829 significantly enriched and 3721 significantly depleted transcripts (**Figure 2.6A and B**). This is in agreement with the previous observations that the SG transcriptome is conserved between multiple stresses [170,171]. We also observed that the SG transcriptome based on PABPC1 immunopurification is largely conserved between arsenite and sorbitol stresses and is similar to the SG transcriptomes defined by G3BP1 immunopurification (**Figure 2.6C-E**). Taken together, our results indicate that the SG transcriptome is highly similar between arsenite and sorbitol stress conditions, and that the mRNAs pulled down are independent of the SG protein used for the affinity purification.

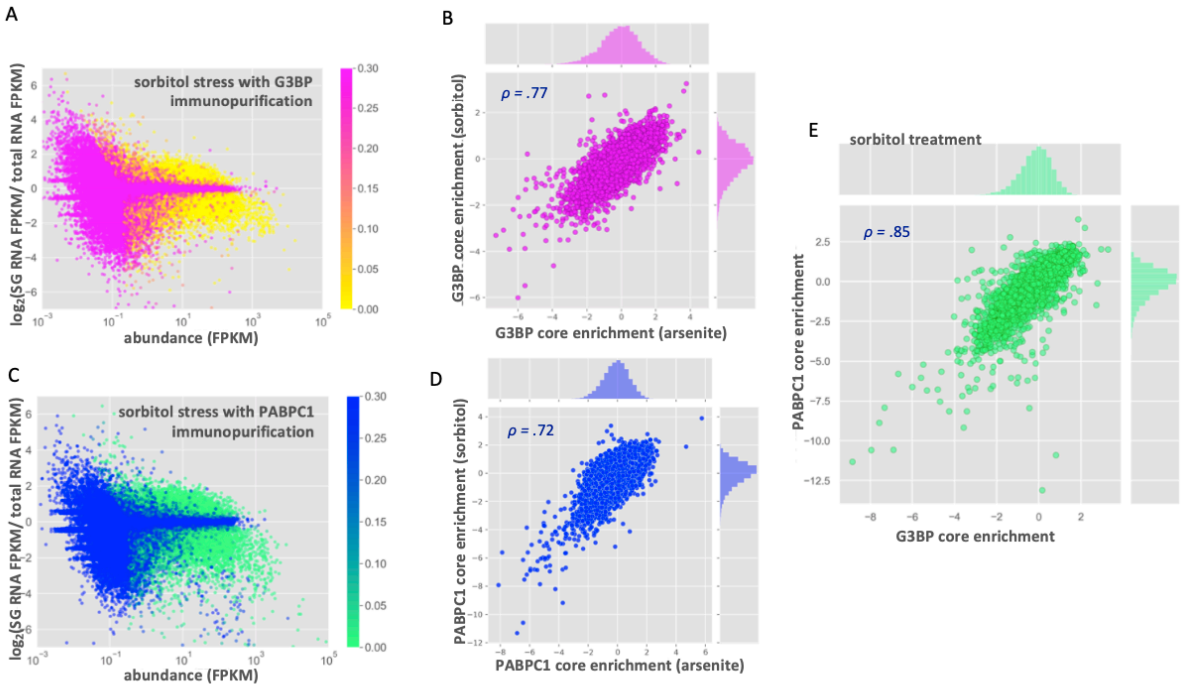

Figure 2.6. RNA localization to stress granule cores is conserved between sorbitol and arsenite stress.

(**A**) MA-plot showing stress granule enrichment vs. abundance for G3BP1 purified SGs during sorbitol treatment. (**B**) Scatterplot showing correlation between G3BP core enrichment scores in sorbitol vs. arsenite stress. (**C**) MA-plot showing stress granule enrichment vs. abundance for PABPC1 purified SGs during sorbitol treatment. (**D**) Scatterplot showing correlation between RNA enrichment scores from PABPC1 core purification in sorbitol vs. arsenite stress. (**E**) Scatterplot showing correlation between enrichment scores from PABPC1- and G3BP- purified SG cores during sorbitol stress.

We then examined whether G3BP1 and G3BP2 affected the mRNAs partitioning into SGs during sorbitol stress. To test this possibility, we purified sorbitol-induced SG cores from WT and ΔΔG3BP1/2 U-2 OS cells using antibodies to PABPC1 (**Appendix Figures A.9 and A.10**). Strikingly, sorbitol-induced SGs contained a similar transcriptome regardless of whether cells expressed or lacked G3BP1 & G3BP2 (**Figure 2.7A and B**). The enrichment scores for these transcriptomes showed a strong linear correlation (R = 0.94), suggesting that the enrichment of RNA in SGs is largely independent of G3BP during sorbitol stress. We interpret this observation to argue that G3BP1 and G3BP2 do not generally affect the mRNAs recruited to SGs.

Interactions between G3BP and mRNA might act in concert with other RBP-RNA, or RNA-RNA interactions to drive RNAs into SGs [170,189]. In this view, G3BP would only affect the recruitment of mRNAs to SGs that were on the cusp of SG enrichment. In order to examine this possibility, we calculated the change in ΔΔG3BP1/2 SG enrichment scores vs. WT enrichment scores as a function of RNA length. If G3BP acted in concert with other RNA-RNA and RNA-RBP interactions to drive localization to SGs, one would anticipate that G3BP would only have an observable effect for transcripts of shorter lengths, which have fewer interactions. We observed similar SG enrichment between WT and ΔΔG3BP1/2 cell lines for RNAs of any length (**Figure 2.7C**). Thus, we observed no significant impact of G3BP1 and G3BP2 on mRNA targeting to SGs even when binning for different lengths of mRNAs.

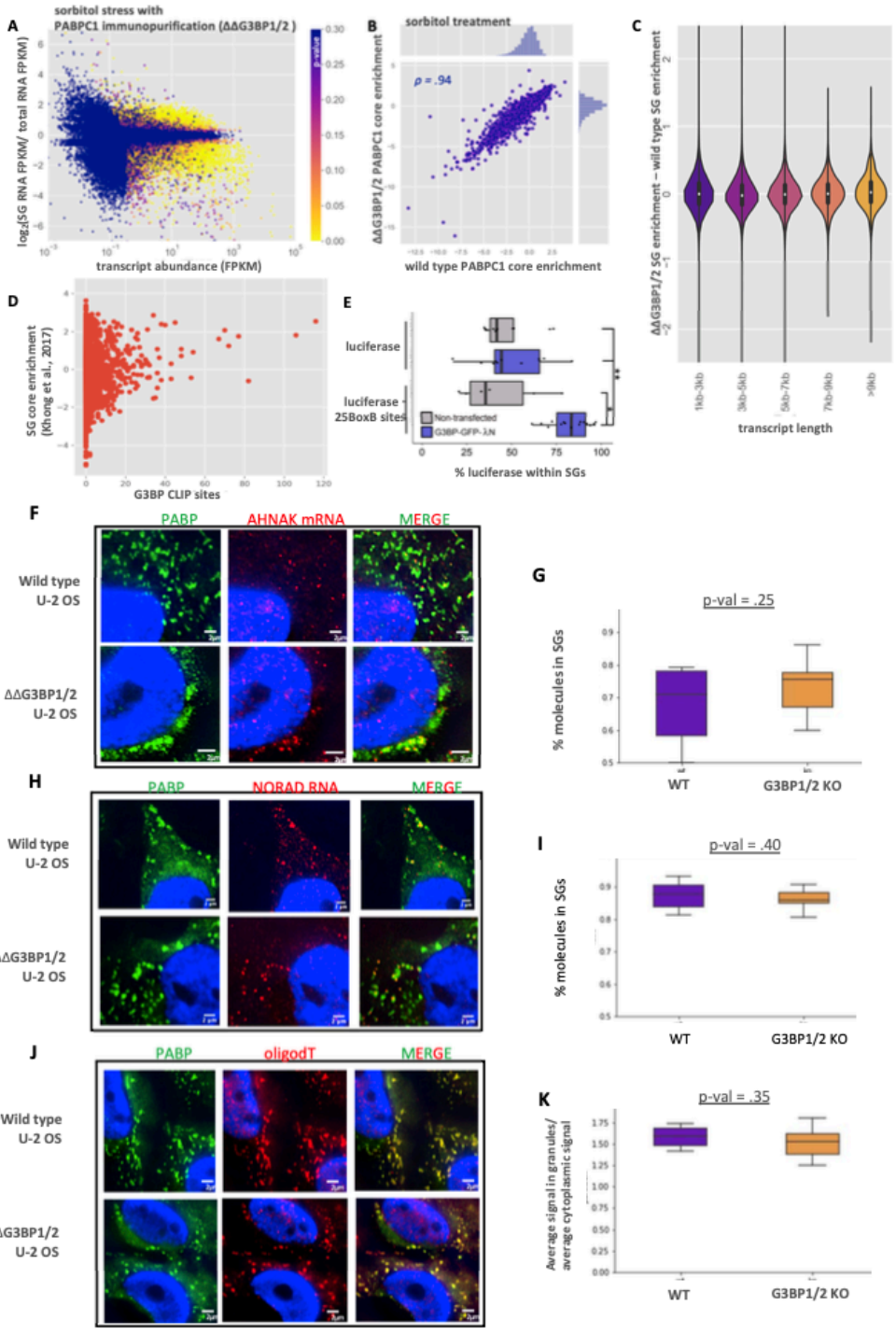
A
sorbitol stress with
PABPC1 immunopurification (ΔΔG3BP1/2)
log2[SG RNA FPKM/ total RNA FPKM)
transcript abundance (FPKM)
p-value
B
sorbitol treatment
p = .94
ΔΔG3BP1/2 PABPC1 core enrichment
wild type PABPC1 core enrichment
C
ΔΔG3BP1/2 SG enrichment – wild type SG enrichment
1kb-3kb
3kb-5kb
5kb-7kb
7kb-9kb
>9kb
transcript length
D
SG core enrichment
(Khong et al., 2017)
G3BP CLIP sites
E
luciferase
luciferase-
25BoxB sites
Non-transfected
G3BP-GFP-λN
% luciferase within SGs
F
PABP
AHNAK mRNA
MERGE
Wild type
U-2 OS
ΔΔG3BP1/2
U-2 OS
G
p-val = .25
% molecules in SGs
WT
G3BP1/2 KO
H
PABP
NORAD RNA
MERGE
Wild type
U-2 OS
ΔΔG3BP1/2
U-2 OS
I
p-val = .40
% molecules in SGs
WT
G3BP1/2 KO
J
PABP
oligodT
MERGE
Wild type
U-2 OS
ΔΔG3BP1/2
U-2 OS
K
p-val = .35
Average signal in granules/
average cytoplasmic signal
WT
G3BP1/2 KO

Figure 2.7. Global RNA localization to stress granule cores is independent of G3BP.

(**A**) MA-plot showing stress granule enrichment vs. abundance for PABPC1 purified SGs during sorbitol treatment in ΔΔG3BP1/2 cells. (**B**) Scatterplot depicting the enrichment of transcripts in PABPC1 stress granule cores in ΔΔG3BP1/2 vs WT U-2 OS cells during sorbitol stress. (**C**) Violin plots depicting ΔΔG3BP1/2 - WT stress granule enrichment ratios for all transcripts, binned by length. (**D**) Scatterplot depicting the fraction of a transcript that is localized to SGs during arsenite stress vs. the number of G3BP eCLIP peaks for that transcript. (**E**) Boxplot showing the localization to SGs of *luciferase* reporter RNAs with 0 or 25 BoxB sites during sorbitol stress in non-transfected and G3BP-GFP-λN transfected cells. *p<0.01, **p<0.001. (**F**) smFISH of *AHNAK* mRNA during sorbitol stress in WT and ΔΔG3BP1/2 cells. (**G**) Boxplot quantifying the fraction of *AHNAK* cytoplasmic transcripts in SGs in WT and ΔΔG3BP1/2 cells**.** (**H**) smFISH of *NORAD* mRNA during sorbitol stress in WT and ΔΔG3BP1/2 cells. **(I)** Boxplot quantifying the fraction of *NORAD* in SGs in WT and ΔΔG3BP1/2 cells**.** (**J**) FISH of poly(A) RNA during sorbitol stress in WT and ΔΔG3BP1/2 cells. (**K**) Boxplot quantifying average intensity of poly(A) signal inside SGs vs. average intensity of poly(A) signal in the cytoplasm.

Another possibility is that only transcripts that exhibit G3BP binding capability would show differential recruitment to SGs. Thus, we utilized data from a recent eCLIP study which examined G3BP eCLIP targets [223]. However, we observed that G3BP binding as assessed by eCLIP and SG enrichment were only weakly positively correlated (**Figure 2.7D**). Moreover, G3BP target transcripts showed no altered localization in ΔΔG3BP1/2 cells, nor when we limited the analysis to short transcripts (**Appendix Figure A.11**).

G3BP is required for SG formation during arsenite stress, but not sorbitol stress. Thus, one possibility is that G3BP simply does not have any influence over the partitioning of RNAs during sorbitol stress. To test this possibility, we examined if tethered G3BP1 could target the *luciferase* mRNA to SGs under sorbitol stress in a manner similar to what was observed under arsenite stress. We observed that G3BP1 tethering led to a significant and reproducible increase in *luciferase* localization to SGs during sorbitol stress (**Figure 2.7E**). Thus, G3BP1 can still artificially drive SG enrichment of a reporter mRNA even in sorbitol stress wherein G3BP is not required for SG formation.

A final possibility for why the SG transcriptome does not change in the ΔΔG3BP1/2 cell lines is that depletion of G3BP affects all transcripts equally, which might be missed in our sequencing data. Thus, we examined whether global RNA recruitment to SGs was altered in ΔΔG3BP1/2 cells. By smFISH, we detected no discernable difference in the localization of *AHNAK* (**Figure 2.7F and G**). This is in spite of the fact that *AHNAK* has over 70 predicted G3BP CLIP sites (**Figure 2.7D**). This suggests that even transcripts with many G3BP sites may see modest changes in partitioning, likely

due to compensating interactions that extremely large mRNAs like *AHNAK* (18 kb) are capable of forming. Both *NORAD* and total poly(A)+ signal showed a slight reduction in SG partitioning in ΔΔG3BP1/2 cells (**Figure 2.7H-K**), although these reductions did not achieve statistical significance. Both AHNAK and NORAD transcripts lie in the plateau region of our mathematical model of SG interactions **(Figure 2.4)**. Thus, as we predicted from our previous mathematical modeling of SG enrichment, SG-enriched transcripts containing large numbers of interactions with SG-enriched RBPs should be insensitive to deletion of any single RBP. These findings argue that G3BP does not strongly affect the SG transcriptome. More broadly, this suggests that individual interactions between an mRNP and a SG that are of a similar strength as G3BP interactions with SGs will have minimal effects on mRNP partitioning into SGs. Therefore, RNA localization to SGs largely arises through the synergistic effects of multiple interactions acting in concert.

2.4. Discussion

In this work we present evidence that specific RNA-binding proteins can localize mRNPs into SGs. The critical observation is that tethered G3BP1, TIA1, or FMRP can increase the partitioning of the *luciferase* mRNA into SGs (**Figures 2.2 and 2.3**). Although it has been widely anticipated that RBPs can target mRNAs to SGs, to our knowledge this observation provides the first demonstration of this principle. We cannot rule out the possibility that the increased localization of reporter RNAs within SGs may also be due to seeding of SGs at the site of the reporter RNA due to the creation of a high local concentration of a SG component. We anticipate that both seeding and active recruitment contribute to enhanced localization of our reporter RNAs in SGs. Possible mechanisms by which mRNAs could be targeted to SGs by G3BP1 or TIA1 specifically include the formation of G3BP1 dimers [221], or interactions between the TIA1 prion-like domain [228].

We present two lines of evidence that the partitioning of an mRNP into SGs will be based on multiple elements acting in an additive manner. First, we observed that multiple elements within the *NORAD* RNA were sufficient to increase the SG enrichment of a *luciferase* reporter RNA (**Figure 2.1**). Second, we demonstrated that the ability of tethered G3BP1 to target the reporter mRNA to SGs was dose-dependent (**Figure 2.2**). The ability of protein interactions to target mRNPs to SGs suggests that the partitioning of an mRNP into a SG will be a summation of protein-protein, protein-RNA and RNA-RNA interactions between an individual mRNP and the SG. This is directly analogous to the hypothesis that SGs form through various combinations of interactions between different mRNPs [189].

Thus, the recruitment of mRNPs into SGs reflects the summation of a number of interactions between individual mRNPs.

The recruitment of RNPs can be considered a simple equilibrium binding reaction with the partitioning of the RNP (K_{eq}) being proportional to $e^{-\Delta G/RT}$. Moreover, we observed that the SG enrichment of individual RNPs was correlated with the number of interactions in a logarithmic manner (**Figure 2.4**). This is consistent with the model where the energetics of each individual interaction sum together to give an overall ΔG for SG partitioning as predicted by simple equilibrium binding.

By using some reasonable assumptions, we are able to make estimations of the number of interactions a given RNP will have with SGs and its partition coefficient. In this analysis, we estimate the number of interactions based on their similarity to a G3BP1 interaction. While this is undoubtedly an over-simplification, it allows for the first estimation of how many interactions RNPs have within SGs. Moreover, we note that tethered G3BP1 and TIA1 gave similar degrees of SG partitioning of the *luciferase* mRNA with 25 BoxB sites, suggesting that at least these two proteins have similar interactions with SGs. These estimates suggest that mRNAs with less than 20% of their mRNAs in SGs have 1-5 predicted RNP-SG interactions, while mRNAs that partition greater than 50% of their mRNAs in SGs have over 15 predicted RNP-SG interactions. Although these are crude estimates these numbers make two important points. First, the number of interactions a highly enriched RNP has in SGs is quite high. For example, we estimate that *AHNAK* mRNA will have 97 predicted RNP-SG interactions. This highlights the

second important conclusion: any given interaction only makes a small contribution to the overall enrichment of mRNAs in SGs. For example, for the *AHNAK* mRNA we estimate removing a single interaction between the mRNP and SG would alter the enrichment by 0.2%.

As a test of this rationale, we examined the global RNA composition of SGs in cells lacking the highly abundant SG RBPs G3BP1&2. In agreement with our hypothesis, we found that WT and ΔΔG3BP1/2 cell lines contain a similar SG transcriptome (**Figure 2.7**). This observation was confirmed by smFISH for *AHNAK*, *NORAD*, and by oligodT staining.

Taken together, we propose a model in which multiple RBP-RNA and RNA-RNA interactions act synergistically to define the RNA composition of SGs (**Figure 2.8**). In this model, deletion, or depletion of any single RBP would have a negligible effect on RNA localization to SGs. which is supported by the evidence that G3BP1 & G3BP2 deletions had essentially no effect on the SG transcriptome (**Figure 2.7**). Similarly, cells lacking Pumilio proteins can still accumulate *NORAD* in SGs, based on the sequencing of a heavy RNP containing fraction [171]. This is likely due to the ability of other RBPs and RNA-RNA interactions to compensate for the absence of G3BP or Pumilio. It remains a challenging and technical feat to distinguish between the role of each type of interaction and SG partitioning. We presume that some RNPs will be driven to SGs primarily through RNA-RNA interactions while others may depend more heavily on the multivalent interactions of their constituent proteins. The fact that the RNA composition of SGs is largely conserved between different stresses (**Figure 2.6**) also supports our estimations [170,171].

Since some proteins are only recruited to SGs under specific stresses [217,229], the loss of these potential interactions in SGs has little effect on the global RNA composition of SGs. Thus, there are likely multiple synergistic/redundant interactions that lead to RNA enrichment in SGs. This is not to say that individual RBPs cannot modulate the ability of an RNA to enrich in SGs. Indeed, increasing the number of RBPs on a transcript can lead to the enhanced enrichment of that transcript in SGs (**Figure 2.2 and 2.3**). We hypothesize that other SG RBPs should also be able to modulate the recruitment of transcripts similarly to G3BP tethering. It remains possible that there will be some molecular interactions between RNPs and SGs that are much stronger than the average G3BP1-SG or TIA1-SG interaction we define here and will therefore have a larger effect on the SG partitioning of an individual mRNP.

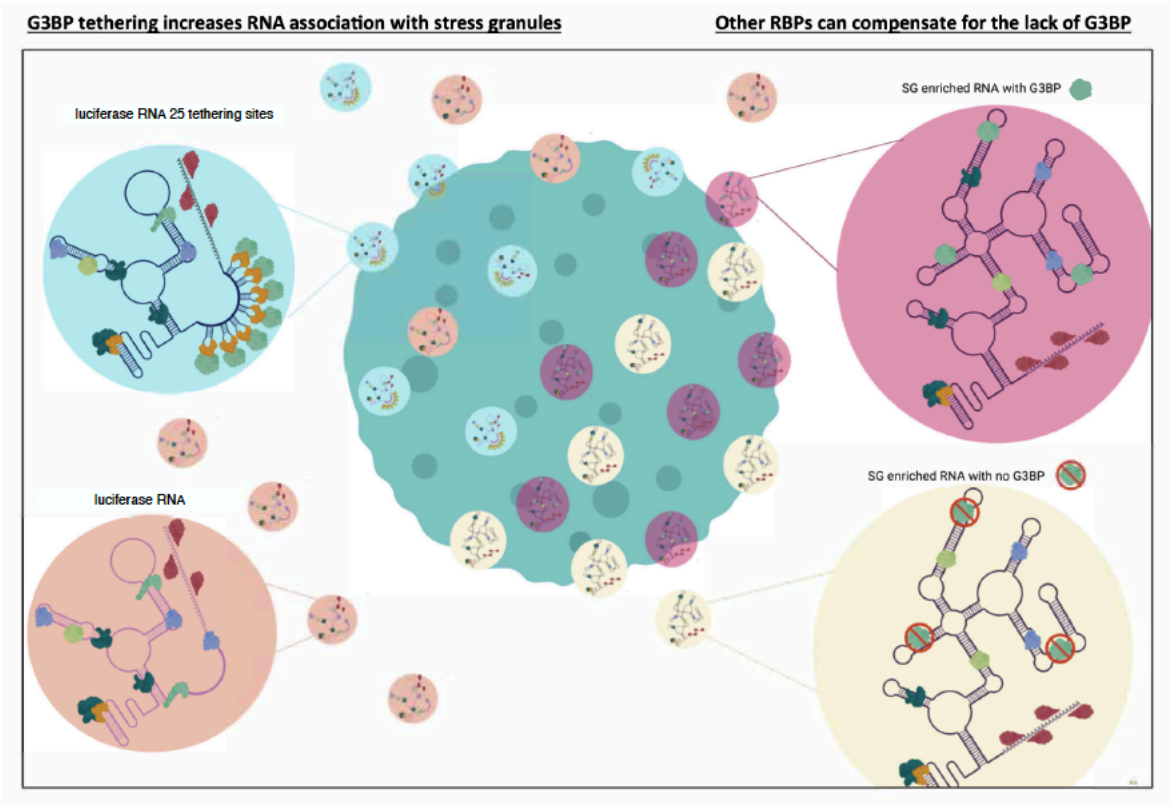

Figure 2.8. Synergistic recruitment of mRNPs to SGs based on the number of SG interactions. Model for RNA recruitment for stress granules. ***Left:*** Tethering, e.g. G3BP to RNAs that contain few SG interactions, can increase an RNA's association with stress granules. ***Right:*** Deletion of individual interactions from RNPs with many interactions with stress granules leads to limited changes in RNA recruitment to SGs since other interactions can compensate.

Three recent studies focused on the importance of G3BP in the formation of stress granules [230-232]. All three commented on the ability of G3BP to modulate valency either through RNA-induced conformational switching of the protein through intramolecular interactions featuring the IDR and RBD [230,232] or through valence capping via the interaction of G3BP with other less-valent proteins [231]. An apparent conundrum from these observations is that G3BP1 is required for stress granule formation in many stresses, but its absence does not notably alter the transcriptome of SGs. We suggest that the resolution to this conundrum is due to the fundamental differences in the kinetics of stress granule assembly as compared to the recruitment of individual mRNPs into SGs. The formation of SGs is a cooperative process wherein the average interaction between mRNPs will set a critical threshold above which mRNP nucleation into SGs will initiate, followed by recruitment of additional mRNPs to form SG cores. If the average interaction between mRNPs is altered even by 10% this can shift the system into a region of non-assembly due to the highly cooperative nature of SG cores, which contain 20-70 mRNAs [170]. Thus, SG assembly is highly cooperative and very sensitive to the average interaction strength between individual mRNPs. Such highly cooperative assembly, and sensitivity to small changes in average interactions is a general property of any large assembly made up of multiple components, which provides numerous opportunities for the regulation of higher scale assembly. In contrast, the recruitment of an individual mRNP into an existing SG can be considered a simple equilibrium binding reaction without a cooperative effect of changes in mRNP affinities such that changes in K_Ds have modest effects on mRNA partitioning.

This analysis makes several predictions. First, components required for SG formation can halt overall assembly without substantially affecting the transcriptome of SGs in cases where they do form. Second, increasing SG formation artificially (e.g. by inhibiting eIF4A) [192]; or by over-expressing TIA1 will still generally lead to the same mRNAs accumulating in SG. Third, genetic or pharmacological manipulations that alter the initiation events, or average interactions between mRNPs, even by a small amount, can prevent SG formation.

2.5. Materials and Methods

Plasmid Construction

For a list of plasmids constructed for use in this manuscript, as well as oligos used for plasmid construction, please see **Appendix Table A.2**. Tet-inducible Luciferase reporter was a gift from Moritoshi Sato (Addgene plasmid # 64127; http://n2t.net/addgene:64127; RRID:Addgene_64127) [233]. BoxB repeats were cloned out of pCMV5-25BoxB, which was a gift from Maria Carmo-Fonseca (Addgene plasmid # 60817; http://n2t.net/addgene:60817; RRID:Addgene_60817) [234] and placed into the 3'UTR of the luciferase reporter. Vector used as the backbone for AAVS targeting of Cas9 was pRP2855, an AAVS-TDP43 plasmid, in which the TDP43 was excised by restriction digest and replaced with *luciferase* constructs. G3BP-GFP-λN and GFP-λN plasmids were gifts from Richard Lloyd's lab. FMRP was cloned out of pFRT-TODestFLAGHAhFMRPiso1, a gift from Thomas Tuschl (Addgene plasmid # 48690; http://n2t.net/addgene:48690: RRID:Addgene_48690) [235]. NORAD-PREmut plasmid was a gift from Josh Mendel's lab and placed into the 3' UTR of the *luciferase* reporter.

Genomic integration into AAVS locus

Cells were transfected with 1 μg CRISPR/Cas9 plasmid (pRP2854) in conjunction with 1 μg appropriate *luciferase* reporter construct (pRP2856, pRP2873 and pRP2874) using Jet Prime reagent. Transfection of pRP2854 alone was used as a negative control. 24 hours following transfection, cells were split from a 6-well plate to a 10 cm dish. After another 24 hours, media was replaced with new media containing 1 μg/mL puromycin to begin selection for cells with genomic integration. Following 24 hours with puromycin

selection, media was replaced with fresh puromycin. After all cells were dead in the negative control plate, media was replaced with fresh media lacking puromycin for 48 hours. This is an optional step to help get rid of any residual plasmid. Puromycin was then added for another 48 hours to finalize the selection. Single colony selection was not done for these experiments.

Stellaris smFISH probes

Custom Stellaris smFISH probes against *AHNAK*, *NORAD* and firefly *luciferase* transcripts were designed with Stellaris RNA FISH Probe Designer (Biosearch Technologies, Petaluma, CA), available online at http://www.biosearchtech.com/stellaris-designer (version 4.2). AHNAK and *NORAD* smFISH probes, labeled with Quasar 670 dye, and firefly *luciferase* probes, labeled with Quasar 570, were ordered from Stellaris (Biosearch Technologies, Petaluma, CA).

Sequential IF and FISH

Sequential immunofluorescence and smFISH on fixed U-2 OS cells was performed with Stellaris buffers or homemade buffers [236] according to the manufacturer's protocol: (https://biosearchassets.blob.core.windows.net/assets/bti_custom_stellaris_immunofluorescence_seq_protocol.pdf).

Briefly, U-2 OS cells were seeded on sterilized coverslips in 6-well tissue culture plates. At ~80% confluency, media was exchanged 1 hour before experimentation with fresh media. After stressing cells (see stress conditions), the media was aspirated, and

the cells were washed with pre-warmed 1×PBS. The cells were fixed with 500 μL 4% paraformaldehyde for ten minutes at room temperature. After fixation, cells were washed twice with 1×PBS, permeabilized in 0.1% Triton X-100 in 1×PBS for five minutes and washed once with 1×PBS.

For IF detection, coverslips were incubated in primary antibody for 1 hour. Coverslips were washed three times with 1×PBS for 10 minutes each wash. Then cells were incubated in secondary antibody (Thermo Fisher Scientific A-31553). Again, coverslips were washed three times with 1×PBS for 10 minutes each wash. Then, cells were treated with smFISH Buffer A for 5 min. Coverslips were transferred to a humidifying chamber with smFISH probes and placed in the dark at 37°C for 16 hours. Coverslips were placed in Buffer A for 30 minutes in the dark, washed with Buffer B for 5 minutes and placed onto a slide with VECTASHIELD Antifade Mounting Medium with DAPI (Vector Labs, H-1200). For assays requiring quantification of smFISH probes in stress granules, VECTASHIELD Antifade Mounting Medium without DAPI was used (Vector Labs, H-1000).

In order to maintain consistency, the same protocol was utilized in IF only experiments, however the portions of the protocol calling for smFISH were omitted. Antibodies that were used include PABP (Abcam ab21060), G3BP (Abcam ab56574). In all imaging experiments at least 10 cells were imaged.

smFISH probes were labeled based on a recent protocol [237]. Oligonucleotides used for smFISH were designed using the Stellaris Probe Designer (https://www.biosearchtech.com/support/education/stellaris-rna-fish). Briefly, oligos were labeled by incubating 4 μL of 200 μM pooled oligonucleotides (Integrated DNA Technologies), 1 μL of TdT (Thermo Fischer Scientific EP0161) and 6 μL of ddUTP (Axxora JBS-NU-1619-633**)** fluorophore for eight hours. After 8 hours, another 1 μL of TdT enzyme was added and the reaction was allowed to continue overnight. Probes were then ethanol precipitated by adding 164.5 μL of nuclease free water, 0.5 μL of 0.5 mg/ml linear acrylamide, 20 μL of 3 M sodium acetate (pH 5.5) and 800 μL of pre-chilled 100% ethanol. This mixture was then placed at -80°C for at least 20 minutes. Labeled oligos were pelleted by centrifugation at 16,000 ×g at 4°C. Probes were then washed 3 times by adding 1 mL of 80% ethanol and centrifugation at 16,000 ×g at 4°C. After washing, the pellet was allowed to air dry for 10 minutes and probes were resuspended in 25 μL of nuclease free water.

Microscopy

Fixed U-2 OS cells stained by immunofluorescence and smFISH, were imaged using a wide field DeltaVision Elite microscope (Applied Biosystems) with a 100× objective and a PCO Edge sCMOS camera. At least five images with 20 Z-sections were taken for each experiment. All images in the manuscript are processed by FIJI [238] or Imaris (Bitplane).

Imaris identification of smFISH spots

To measure the fraction of smFISH spots in stress granules, deconvolved images were analyzed using Bitplane Imaris image analysis software as described in detail in a previous *Methods* manuscript [215]. In short, images were first renamed so that the tallying of cells was blind. This accounts for the variability in the number of cells counted for each condition. We did ensure that at least 10 cells were counted for each condition. Cells were manually segmented to ensure counting of transfected and non-transfected cells. Cells that were saturated in the GFP channel under our imaging conditions were considered to be overexpressing G3BP, e.g., and were excluded from analysis. Imaris can be used to automatically segment SGs as well as identify smFISH spots from each cell taking into account the Z-plane.

U-2 OS growth conditions and reagents

Human osteosarcoma U-2 OS cells expressing G3BP1-GFP (Paul Taylor Lab), U-2 OS cells and U-2 OS ΔΔG3BP1/2 were used in all experiments [221]. All cells were maintained in DMEM with high glucose, 10% fetal bovine serum, and 1% penicillin/streptomycin at 37°C/ 5% CO_2.

Isolation of RNA from U-2 OS cells and SG cores for RNA-sequencing

Parental and ΔΔG3BP1/2 U-2 OS cells expressing G3BP1-GFP were grown to 85% confluency in three 500 cm^2 TC-treated culture dishes (Thermo Fisher Scientific, 07-200-599). One hour prior to stress, cell culture media was exchanged with fresh media. Cells were then stressed with either $NaAsO_2$ or sorbitol (see 'Stress Conditions'). After stress, cells were washed once with media, transferred to falcon tubes, and pelleted at

1,500 ×g for 3 mins. Upon aspirating the media, the pellets were immediately flash-frozen in liquid N_2 and stored at -80°C until isolation of mammalian SG cores was performed. PABPC1 SG cores were purified as previously described for the purification of G3BP cores, however instead of using anti-GFP for the pulldown of SG cores, 20 μL of anti-PABPC1 (ab21060) was used [170,215]. For all experiments, biological triplicates were acquired for both SG-purified RNA and total RNA except in the case of PABPC1 SG RNA purified during sorbitol stress, in which duplicates were acquired (One of the replicates was excluded because it showed little similarity to the other biological replicates).

Stress conditions

To examine mRNA localization during stress, we used the following stress conditions. For arsenite stress experiments, cells were treated with 0.5 mM sodium arsenite (Sigma-Aldrich S7400) for 1 hour. For osmotic stress, cells were stressed in 0.5M D-sorbitol (Sigma-Aldrich S1876) for 2.5 hours. Cells were fixed after the completion of each stress with 4% paraformaldehyde (Fisher Scientific NC0179595).

Library construction and RNA-sequencing

RNA quality was assessed by TapeStation analysis at the Biofrontiers Institute Sequencing Facility. Paired-end cDNA libraries were prepared at the Biofrontiers Institute Sequencing Facility using the KAPA HyperPrep with RiboErase. cDNA libraries were sequenced on a NextSeq High output 150 cycle (2×75).

Sequencing data analysis

Read quality was assessed using fastqc. An index genome was acquired from GENCODE (Release 19 GRCh37.p13). Reads were aligned using hisat2. Differential expression analysis was performed using Cuffdiff (version 2.2.1) with the default parameters [239]. Gene Ontology analysis was performed using the gene ontology consortium (http://www.geneontology.org/). Transcript lengths were acquired from Ensembl's Biomart Tool. All sequencing data can be found at NCBI GEO GSE119977.

Mathematical Modeling

Curve fitting was performed using in Python. The median percent enrichment within stress granules was plotted against the number of box-b sites. The initial number of potential interactions the luciferase can form with SGs, which we refer to as *n*, was allowed to vary from 1 to 10 and the best fit was chosen by examining the pearson's r value of each line. The data was linearized by performing a log-transformation of the data and r values, slope, and intercept positions were calculated using the sklearn package in python. The code for this analysis is available at the following github repository: https://github.com/tmatheny/stress_granule.

2.6. Acknowledgements

We would like to thank Dr. Amber Sorenson, Katelyn Hammond, and Caitlin Poling at the Biofrontiers Next Generation Sequencing Facility for the preparation and sequencing of RNA-Seq libraries. We would like to thank Matthew Deater and Richard Lloyd for the G3BP-GFP-λN and GFP-λN plasmids. Thanks to Joshua Mendel for the NORAD-PRE plasmid. We would like to thank Nancy Kedersha and Paul Anderson for

the ΔΔG3BP1/2 U-2 OS cell line as well as WT U-2 OS cells. The data analysis and visualization work were performed at the BioFrontiers Institute Advanced Light Microscopy Core. The Analysis Workstation and the software package Imaris were supported by NIH 1S10RR026680-01A1. We would also like to thank Paul Taylor for the G3BP1-GFP U-2 OS cells. This work was funded by the NIH (GM045443) and the Howard Hughes Medical Institute. B.V.T was supported by NSF SCR Training Grant T32GM08759.

CHAPTER III

Identification of PARN nuclease activity inhibitors by computational-based docking and high-throughput screening

Contribution statement: This chapter is adapted from the following manuscript. S.S. and R.P. conceived the project. T.N.H. performed the experiments. P.R. performed computational-based docking between human PARN and drugs. T.N.H and R.P. interpreted data. T.N.H. and R.P. wrote the manuscript. All authors edited the manuscript.

Huynh, T. N., Shukla, S., Reigan, P., and Roy, P. (2023) Identification of PARN nuclease activity inhibitors by computational-based docking and high-throughput screening. *Scientific Reports*. 2023. doi: 10.1038/s41598-023-32039-z.

3.1. Abstract

Poly(A)-specific ribonuclease (PARN) is a 3'-exoribonuclease that removes poly(A) tails from the 3' end of RNAs. PARN is known to deadenylate some ncRNAs, including hTR, Y RNAs, and some miRNAs and thereby enhance their stability by limiting the access of 3' to 5' exonucleases recruited by oligo(A) tails. Several PARN-regulated miRNAs target p53 mRNA, and PARN knockdown leads to an increase of p53 protein levels in human cells. Thus, PARN inhibitors might be used to induce p53 levels in some human tumors and act as a therapeutic strategy to treat cancers caused by repressed p53 protein. Herein, we used computational-based molecular docking and high-throughput screening (HTS) to identify small molecule inhibitors of PARN. Validation with *in vitro* and cell-based assays, identified 4 compounds, including 3 novel compounds and pyrimidopyrimidin-2-one GNF-7, previously shown to be a Bcr-Abl inhibitor, as PARN inhibitors. These inhibitors can be used as tool compounds and as lead compounds for the development of improved PARN inhibitors.

3.2. Introduction

Poly(A)-specific ribonuclease (PARN) is a 3' to 5' exonuclease that removes poly(A) or oligo(A) tails from the 3' ends of RNAs [107,109-111]. PARN is expressed ubiquitously in almost all tissues of eukaryotic organisms [106] and has multiple functions in eukaryotes. For example, during early development PARN plays a role in mRNA deadenylation in Xenopus [106,116,240].

In human cells, PARN primarily functions in an adenylation/deadenylation regulatory pathway that regulates the decay rate of ncRNAs (**Figure 3.1**) [29]. In this pathway, Y RNAs, snoRNAs, the human telomerase RNA (hTR), and some miRNAs can be oligoadenylated by noncanonical poly(A) polymerases, such as paralogs PAPD5 and PAPD7 [22-24,29,129]. The presence of the oligo(A) tail can then recruit processive sequence-independent 3' to 5' exonucleases to degrade ncRNAs [12,19,22,24,26,33,35]. Alternatively, the oligoadenylated tail can be removed by adenosine specific 3' to 5' exonucleases such as PARN to maintain stability of ncRNAs. Thus, when PARN is inhibited or defective, some ncRNAs are prematurely degraded, including hTR [22-24,26,27,30,129,241].

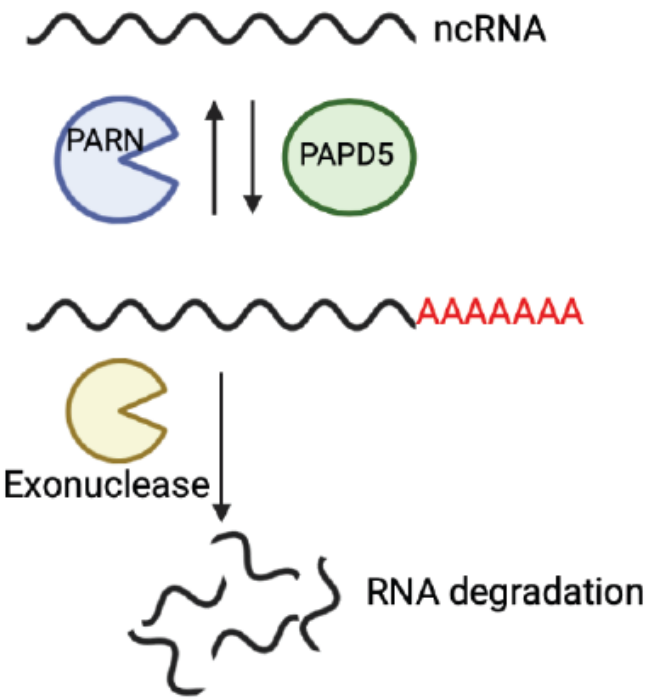

Figure 3.1. PARN functions in an adenylation/deadenylation regulatory pathway that regulates the decay rate of ncRNAs.

ncRNAs could be targeted to adenylation by PAPD5 or deadenylation by PARN [29]. In PARN-deficient cells, the presence of oligo(A) tail can recruit 3' to 5' exonucleases to degrade ncRNAs.

PARN also stabilizes some miRNAs by removing poly(A) tails added by PAPD5, which prevents the recruitment of exonucleases DIS3L or DIS3L2 to degrade miRNAs [22,24]. Importantly, several PARN-regulated miRNAs (miR-380-5p, miR-1285, miR-92, miR-214, miR-485, miR-331, miR-665, miR-3126, and miR-25) either have been shown, or are predicted, to target the TP53 mRNA [242-246]. p53 is tumor suppressor that prevents outgrowth of aberrant cells by inducing cell-cycle arrest, DNA repair or programmed cell death [247]. It has been shown that numerous human cancers increase proliferation and resistance to DNA-damage agents by downregulating the p53 pathway [248,249]. Moreover, depletion of PARN upregulates p53 and sensitizes cells to chemotherapeutic agents [24,250]. Thus, inhibition of PARN might be an effective intervention to induce the expression of p53 in some tumors and thereby limit tumor progression.

Currently, only a limited number of PARN inhibitors exist [251-255]. To identify potential inhibitors of PARN, we performed computational-based docking between human PARN and a small molecule library of adenosine analogs and performed high-throughput screening (HTS) of a small molecule library. The combination of these two approaches allowed us to identify four compounds that inhibit PARN *in vitro* and also repress PARN activity in Hela cells.

4.3. Results

Purification of PARN for *in vitro* assay

To test the effects of compounds on PARN, we purified the enzyme and developed an *in vitro* assay for PARN activity. Expression of full-length PARN led to aggregation, but expression of the C-terminal truncated protein (1-430 aa of PARN) was soluble. Previous work has shown that the D28A and F31A mutations in PARN inhibit PARN activity [90]. Given this, we expressed and purified the catalytic mutant PARN D28A F31A (PARNmut) as a negative control. Purification (see **METHODS**) yielded a dominant band for $PARN_{1-430}$ and PARNmut on SDS-PAGE gels (**Figure 3.2A and B**).

We found that purified $PARN_{1-430}$ shows enzymatic activity on the poly(A) tail of test substrates. $PARN_{1-430}$ was incubated with a fluorescently labeled RNA with a CCUUUCC sequence followed by a 9 nucleotide-long poly(A) tail and the reaction product was visualized on denaturing acrylamide gels. We observed that PARN removed the 3' oligo(A) tail from the RNA substrate (**Figure 3.2C and D**). The activity was dependent on PARN since PARNmut protein showed no removal of the 3' adenosines (**Figure 3.2C**). Moreover, we observed that PARN is inhibited when treated with adenosine monophosphate (AMP), as has been reported previously [252]. $PARN_{1-430}$ showed reduced activity when incubated with an unadenylated RNA (**Figure 3.2D**), consistent with the finding that $PARN_{1-430}$ preferentially degrades poly(A) tail [108].

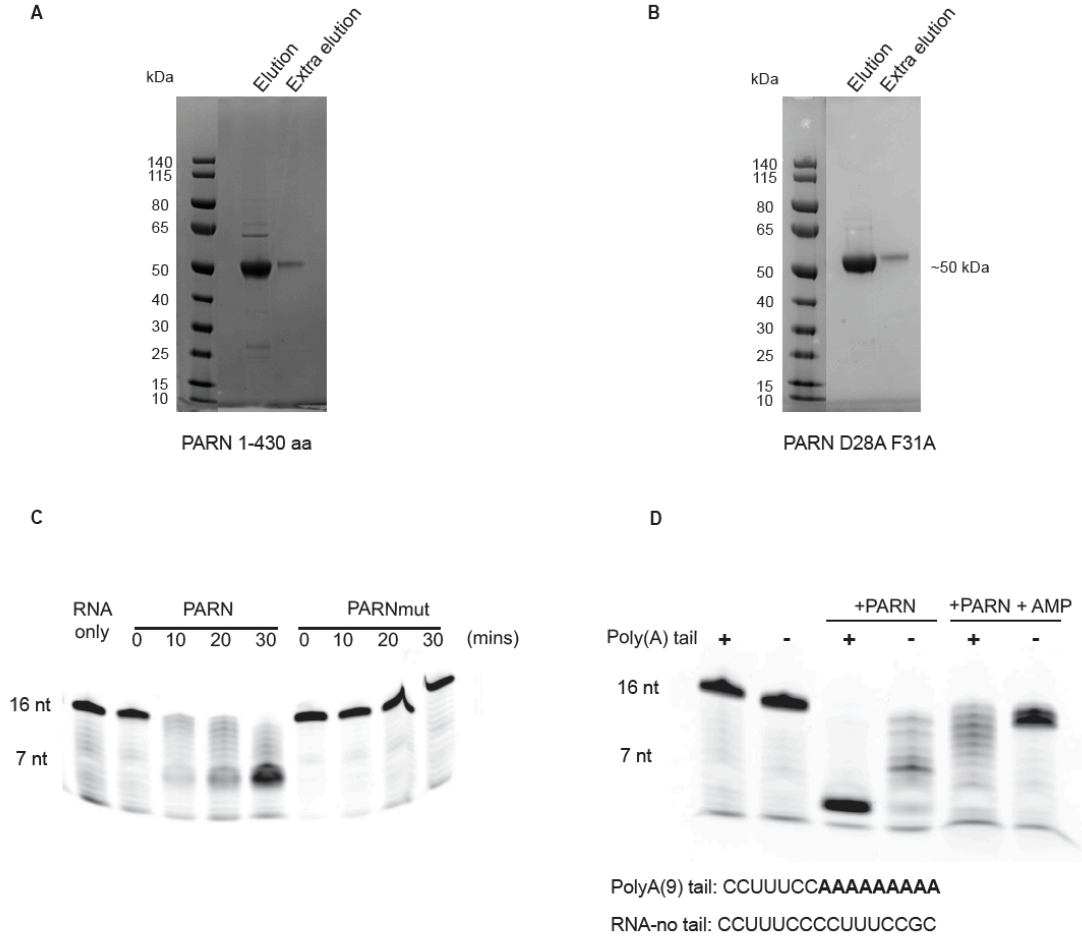

Figure 3.2. PARN purification and validation.

(**A**) SDS-PAGE gel of the fractions during $PARN_{1-430}$ purification. (**B**) SDS-PAGE gel of the fractions during PARNmut purification. (**C**) Gel assay showing $PARN_{1-430}$ and PARNmut's activity activity on poly(A) tail RNA at different time points (0-, 10-, 20-, and 30-minute post incubation), PARNmut shows no enzymatic activity on poly(A) RNA. (**D**) Representative gel confirming PARN activity on poly(A) RNA and non-poly(A) RNA after 20 minutes of incubation. Poly(A) tail RNA sequence is a fluorescently labeled RNA with a CCUUUCC followed by a 9 nucleotides oligo(A) tail. Non-poly(a) RNA is a fluorescently labeled RNA with a CCUUUCCGC tail instead of 9 nucleotides oligo(A) tail. Full gels are presented in **Appendix Figure A.13**.

Developing a high-throughput PARN inhibition assay

To easily screen compounds for inhibition of PARN activity, we developed an assay in which fluorescence was used as the readout for monitoring $PARN_{1-430}$'s activity (**Figure 3.3A**). This assay was modeled on a similar assay developed for Caf1/CNOT7 deadenylase [256]. In this assay, $PARN_{1-430}$ was incubated with a 5'-fluorescently labeled oligoadenylated RNA. In the absence of deadenylation, this substrate RNA can effectively hybridize to a complementary DNA oligonucleotide with a quencher on its 3' end leading to a loss of fluorescence (**Figure 3.3A**). When the RNA substrate is deadenylated, the quenching oligonucleotide is no longer able to stably hybridize leading to an increase in fluorescence in the reaction.

This assay has several features that make it useful for assessing PARN activity. First, it is time-dependent (**Figure 3.3B and D**). Second, it is dependent on PARN concentration (**Figure 3.3C**). Third, we observed that AMP, which is a product of PARN activity and can inhibit $PARN_{1-430}$ at high concentrations (>1 mM), effectively inhibited $PARN_{1-430}$ (**Figure 3.3B**) [252]. Finally, we observed that fluorescence correlates with shortening of the 3' oligo A tail on the substrate by running the material on a gel and observing shortening of the substrate with $PARN_{1-430}$, but no shortening with PARNmut (**Figure 3.2C and 3.3D**). In this assay, $PARN_{1-430}$ inhibition is inversely proportional to the reaction fluorescence measured as output, which we can use to test possible PARN inhibitors.

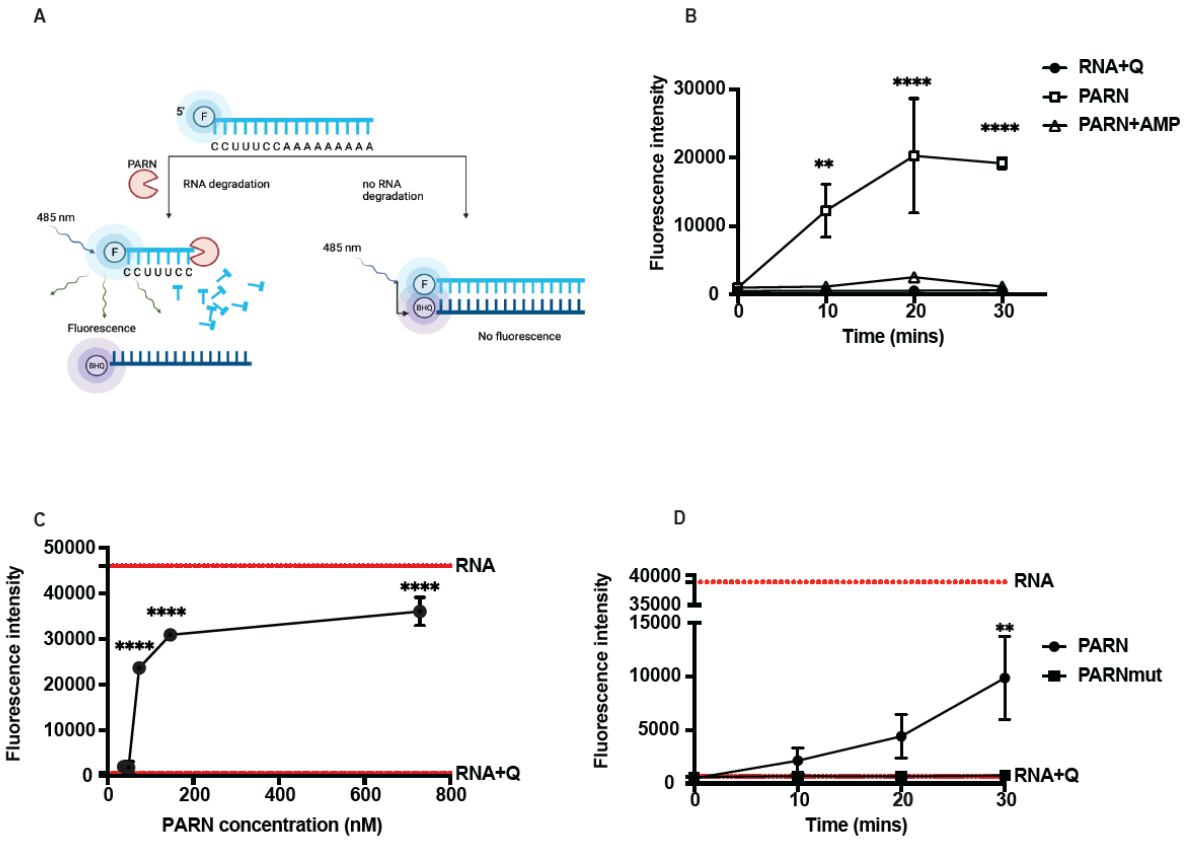
A
5'
F
CCUUUCCAAAAAAAAA
PARN
RNA degradation
no RNA degradation
485 nm
CCUUUCC
Fluorescence
BHQ
485 nm
No fluorescence
B
RNA+Q
PARN
PARN+AMP
Fluorescence intensity
30000
20000
10000
0
**
****
****
0
10
20
30
Time (mins)
C
Fluorescence intensity
50000
40000
30000
20000
10000
0
RNA
RNA+Q
****
****
****
0
200
400
600
800
PARN concentration (nM)
D
Fluorescence intensity
40000
35000
15000
10000
5000
0
RNA
RNA+Q
**
PARN
PARNmut
0
10
20
30
Time (mins)

Figure 3.3. Developing a fluorescence assay for PARN inhibition.

(**A**) Cartoon depicting the inhibition fluorescence assay [256]. Schematic diagram of the fluorescence-based deadenylase assay. The assay is based on a 5′ FAM-labelled RNA oligonucleotide substrate. After incubation of the substrate in the presence of $PARN_{1-430}$, the reaction is stopped and a 3′ BHQ-labelled DNA oligonucleotide probe complementary to the RNA substrate is added. The fluorescence of intact substrate is quenched upon probe hybridization because of the proximity of the BHQ fluorophore. In contrast, the BHQ-labelled probe cannot hybridize to the FAM-labelled reaction product allowing detection of FAM fluorescence. (**B**) $PARN_{1-430}$ inhibition assay with fluorescence as a readout with time course for $PARN_{1-430}$ treatment (73 nM), $PARN_{1-430}$ inhibition with 2.5 mM AMP, and no-enzyme control. 2-way ANOVA, multiple comparisons test, average +/- SD, n=3 replicates. *P<0.05, **P<0.005, ***P<0.001, ****P<0.0001, n.s. was not indicated (**C**) Dose-response curve of $PARN_{1-430}$ enzymatic activity using different $PARN_{1-430}$ concentrations (36.5 nM-730 nM). Dotted-line represents RNA and RNA+Quencher data. One-way ANOVA, multiple comparisons test, average +/- SD, n≥3 replicates. *P<0.05, **P<0.005, ***P<0.001, ****P<0.0001, n.s. was not indicated (**D**) $PARN_{1-430}$ and PARNmut enzymatic activity measured at different time points. PARN showed an increase in activity versus time while PARNmut showed no activity up to 30 minutes incubation. Dotted-line represents RNA and RNA+Quencher data. 2-way ANOVA, multiple comparisons test, average +/- SD, n=3 replicates. *P<0.05, **P<0.005, ***P<0.001, ****P<0.0001, n.s. was not indicated.

Computational-based library docking to identify potential PARN inhibitors

To identify potential small molecule PARN inhibitors, we first used a computational-based docking approach to screen a library of 1820 adenosine analogs from the SelleckChem kinase inhibitor library against the crystal structure of the PARN nuclease domain (PDB: 2A1R) [90]. This library was utilized as the kinase inhibitors are ATP-mimetics and the PARN active site binds adenosine. The PARN nuclease domain includes the four conserved residues among DEDD superfamily, Asp28, Glu30, Asp292, and Asp382, that are important for the catalytic activity of PARN and are required for the binding of divalent metal ions [89]. Mutations of these residues lead to loss of function in PARN [89,134,257]. Therefore, based on this information, we targeted this catalytic site of PARN and selected high-ranking compounds by XP GScore, an approximation of ligand binding free energy, and by interaction with the Asp28-Phe31 region. Analysis of the docking simulation identified several structurally distinct compounds predicted to dock into the PARN catalytic pocket (**Figure 3.4**).

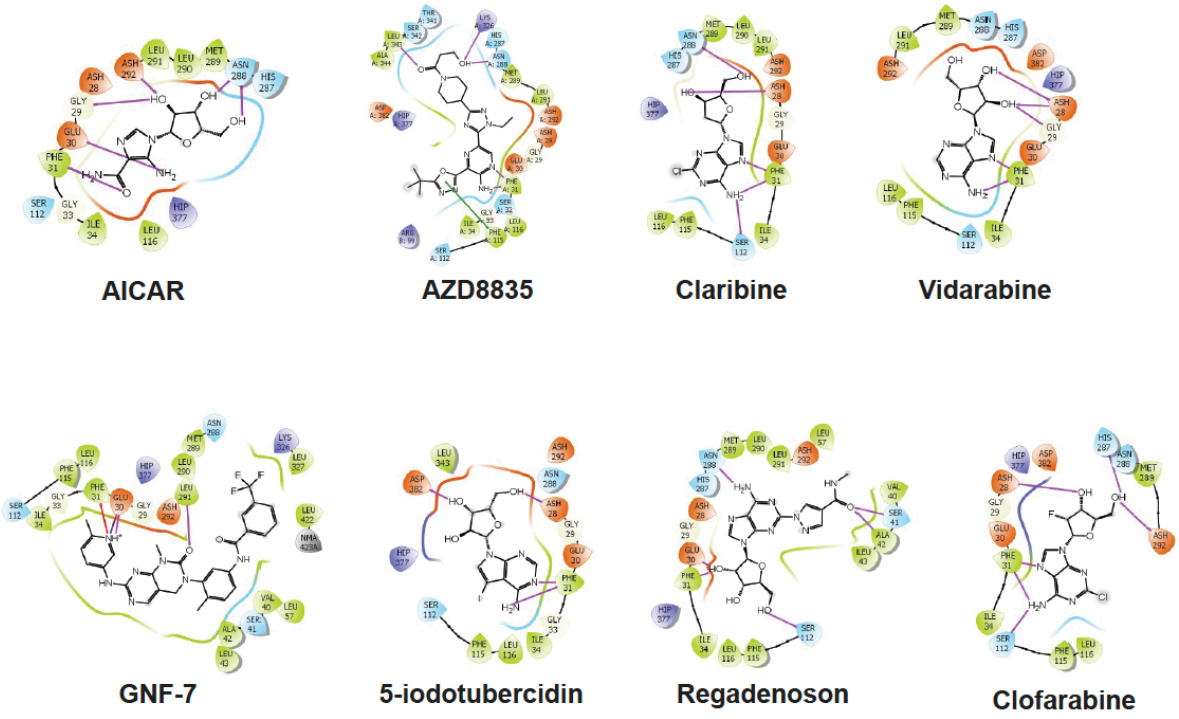

Figure 3.4. Docking of small molecule adenosine analogs into the PARN catalytic site.

Ligand interaction map of the predicted binding mode of AICAR, AZD8835, Claribine, Vidarabine, GNF-7, 5-Iodotubercidin, Regadenson, and Clofarabine, where red residues are charged negative, purple residues are charged positive, green residues are hydrophobic, and blue residues are polar, magenta arrows indicate H-bonds, violet lines indicate salt bridges, and gray spheres represent areas of solvent exposure. HIP represents the ND1 and NE2 protonation state of His and NMA represents N-methyl amide of a capped termini. At least one H-bond interaction was observed between the docked small molecule and amino acid residues Asp28-Phe31.

Testing compounds predicted to interact with PARN

To determine if any of the compounds predicted to dock to PARN showed effects on $PARN_{1-430}$, we tested 15 compounds based on their docking ranks and commercial availability using the fluorescence assay and gels (**Figure 3.5 and Appendix Table A.3**). This screen identified 7 compounds that showed $PARN_{1-430}$ inhibition. GNF-7 (labeled as 5o) has the strongest inhibitory effect on $PARN_{1-430}$ (**Figure 3.5A**). In agreement with the fluorescence assay results, the gel assay also revealed GNF-7 (**Figure 3.5C**), a Bcr-Abl inhibitor [258], as the most effective $PARN_{1-430}$ inhibitor (**Figure 3.5B**). GNF-7 inhibits $PARN_{1-430}$ with a lower concentration compared to AMP (2.5 mM) (**Figure 3.5A and B**).

A dose response curve and kinetic analysis demonstrated that GNF-7 inhibits $PARN_{1-430}$ in a dose-dependent manner (**Figure 3.5D)**. The IC50 of GNF-7 on $PARN_{1-430}$ was determined by non-linear fit to be 35 ± 13 μM. This identified GNF-7 as a potential inhibitor of $PARN_{1-430}$ based on *in vitro* analyses.

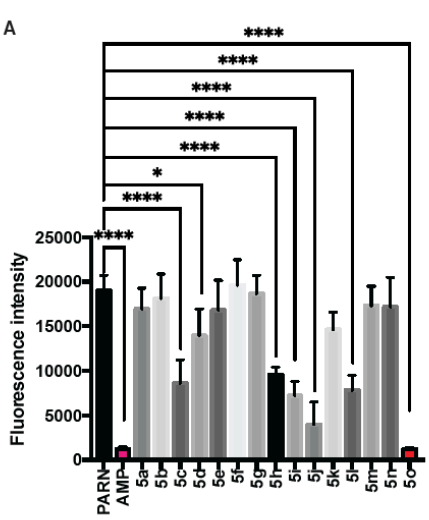
A
****
****
****
****
****
*
****
****
25000
20000
15000
10000
5000
0
Fluorescence intensity
PARN
AMP
5a
5b
5c
5d
5e
5f
5g
5h
5i
5j
5k
5l
5m
5n
5o

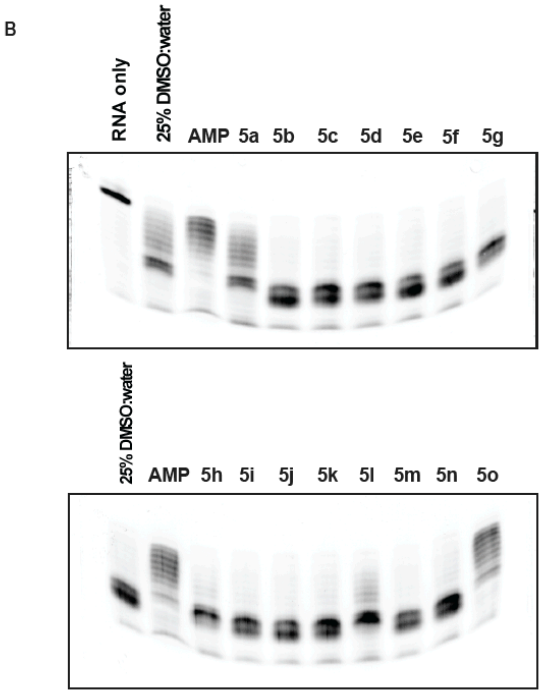
B
RNA only
25% DMSO:water
AMP
5a
5b
5c
5d
5e
5f
5g
25% DMSO:water
AMP
5h
5i
5j
5k
5l
5m
5n
5o

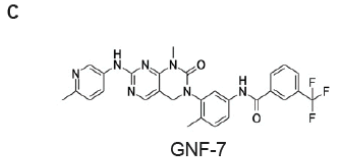
C
GNF-7

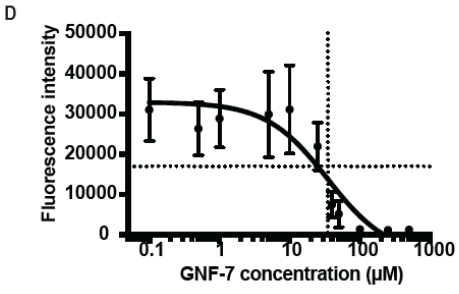
D
50000
40000
30000
20000
10000
0
Fluorescence intensity
0.1
1
10
100
1000
GNF-7 concentration (μM)

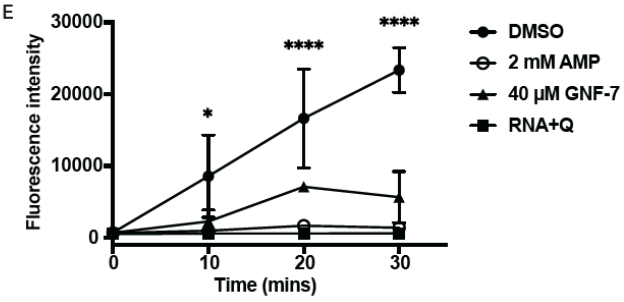
E
30000
20000
10000
0
Fluorescence intensity
*
****
****
0
10
20
30
Time (mins)
DMSO
2 mM AMP
40 μM GNF-7
RNA+Q

Figure 3.5. Testing drugs on activity of PARN using miRNA substrates *in vitro*.

(**A**) Inhibition fluorescence assay showing effects of different drugs on $PARN_{1-430}$. $PARN_{1-430}$ was pretreated with drugs at room temperature for 10 minutes before adding RNA substrate. AMP and GNF-7 were shown in pink and red, respectively. One-way ANOVA, multiple comparisons test, average +/- SD, n≥3 replicates. *P<0.05, **P<0.005, ***P<0.001, ****P<0.0001, n.s. was not indicated. (**B**) Gels illustrating inhibitory effects of different drugs on $PARN_{1-430}$. The reaction was performed the same as the fluorescence assay, heat inactivated, then loaded and visualized on gels. Full gels are presented in **Appendix Figure A.13**. (**C**) Molecular structure of GNF-7. (**D**) Dose-response curve of GNF-7 on $PARN_{1-430}$. $PARN_{1-430}$ was pre-treated with different concentrations of GNF-7 for 10 minutes and incubated with RNA substrate. The reaction was quenched with DNA quencher and fluorescence intensity was measured. The IC50 was determined to be 34.56 μM. The vertical dotted line marks the fitted IC50 of GNF-7 and the horizonal dotted line marks 50% inhibition. (**E**) Kinetic analysis of AMP and GNF-7 effects on $PARN_{1-430}$ and a no-enzyme control. Pretreated $PARN_{1-430}$ was incubated with RNA substrate for 0, 10, 20, and 30 minutes and the fluorescence intensity were measured at each time point. 2-way ANOVA, multiple comparisons, average +/- SD, n=3 replicates. *P<0.05, **P<0.005, ***P<0.001, ****P<0.0001, n.s. was not indicated.

High throughput screening of Enamine kinase library

To identify PARN inhibitors in a high-throughput manner, 24000 compounds from the Enamine kinase library were tested in a HTS utilizing the fluorescence assay (**Figure 3.3A**). The top 18 compounds with IC50s of less than 10 μM based on testing at different concentrations (**Appendix Table A.3**) were then selected for further testing.

To visualize the inhibitory effects of these compounds on PARN, the reactions were run on gels. We showed all compounds could inhibit PARN at 20 μM, except for TH18 (**Figure 3.6**). This result was consistent with the fluorescence assay, suggesting that these compounds can inhibit PARN *in vitro*.

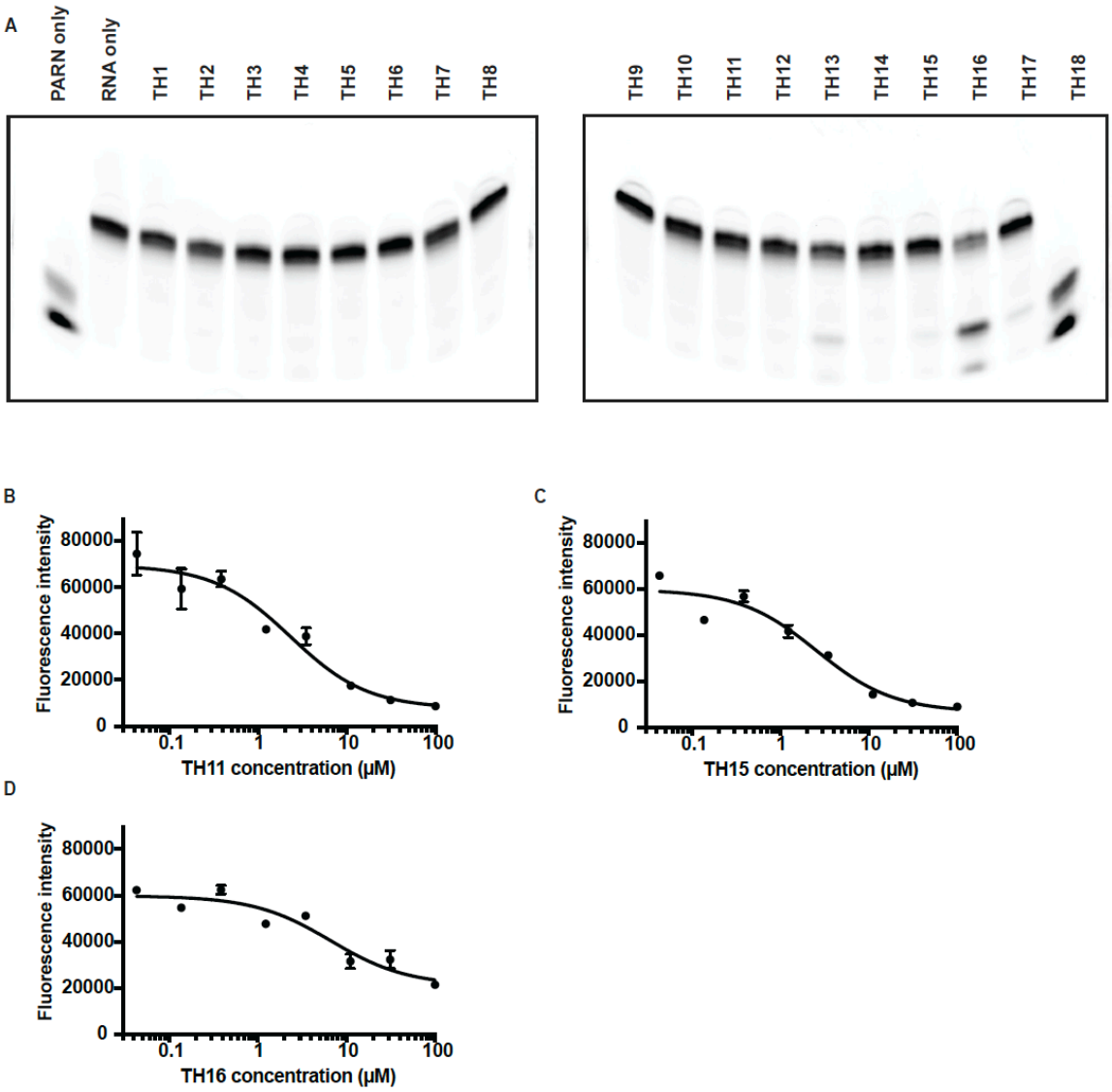

Figure 3.6. Testing high-throughput screening hits using gel assay.

Gels illustrating inhibitory effects of different drugs on $PARN_{1-430}$. (**A**)The reaction was performed the same as the fluorescence assay, heat inactivated, then loaded and visualized on gels. Full gels are presented in **Appendix Figure A.13.** (**B**) Dose-response curve of TH11 on $PARN_{1-430}$. (**C**) Dose-response curve of TH15 on $PARN_{1-430}$. (**D**) Dose-response curve of TH11 on $PARN_{1-430}$.

Examine inhibitory effects of identified compounds on PARN in cells

To test if the compounds identified by docking and HTS affect PARN in cells, we examined the effect of GNF-7, and the compounds from the HTS on RNAs previously known to be affected by PARN activity. Specifically, previous studies showed the levels of telomerase RNA, hTR, and several miRNAs, including miR-21-5p, decreased when PARN is depleted in Hela cells [22,24]. Therefore, we treated Hela cells with all the compounds (50 μM for GNF-7 and 10 μM for TH1-18) for 2 days and measured the levels of these RNAs using northern blotting and/or RT-qPCR.

We observed that treatment with GNF-7 reduced miR-21-5p levels to ~35% compared to the controls when using northern blotting (**Figure 3.7C and D**). Of the compounds from the HTS, TH11, 15, and 16 showed the strongest effects and reduced miR-21-5p levels to ~50% compared to the controls (**Figure 3.7F and G**). These effects were similar to a PARN KD, which reduced miR-21-5p levels to ~75% compared with siRNA controls. None of the compounds reduced PARN protein levels in Hela cells (**Figure 3.7A and B**). Moreover, RT-qPCR was done to examine the changes in hTR levels of the compounds, which confirmed a decrease in levels of hTR with compounds or siPARN treatments, compared to the controls, (**Figure 3.7E and H**). This suggested that GNF-7, TH11, TH15, and TH16 treatments can inhibit PARN activity in cells and thereby decrease specific RNA levels.

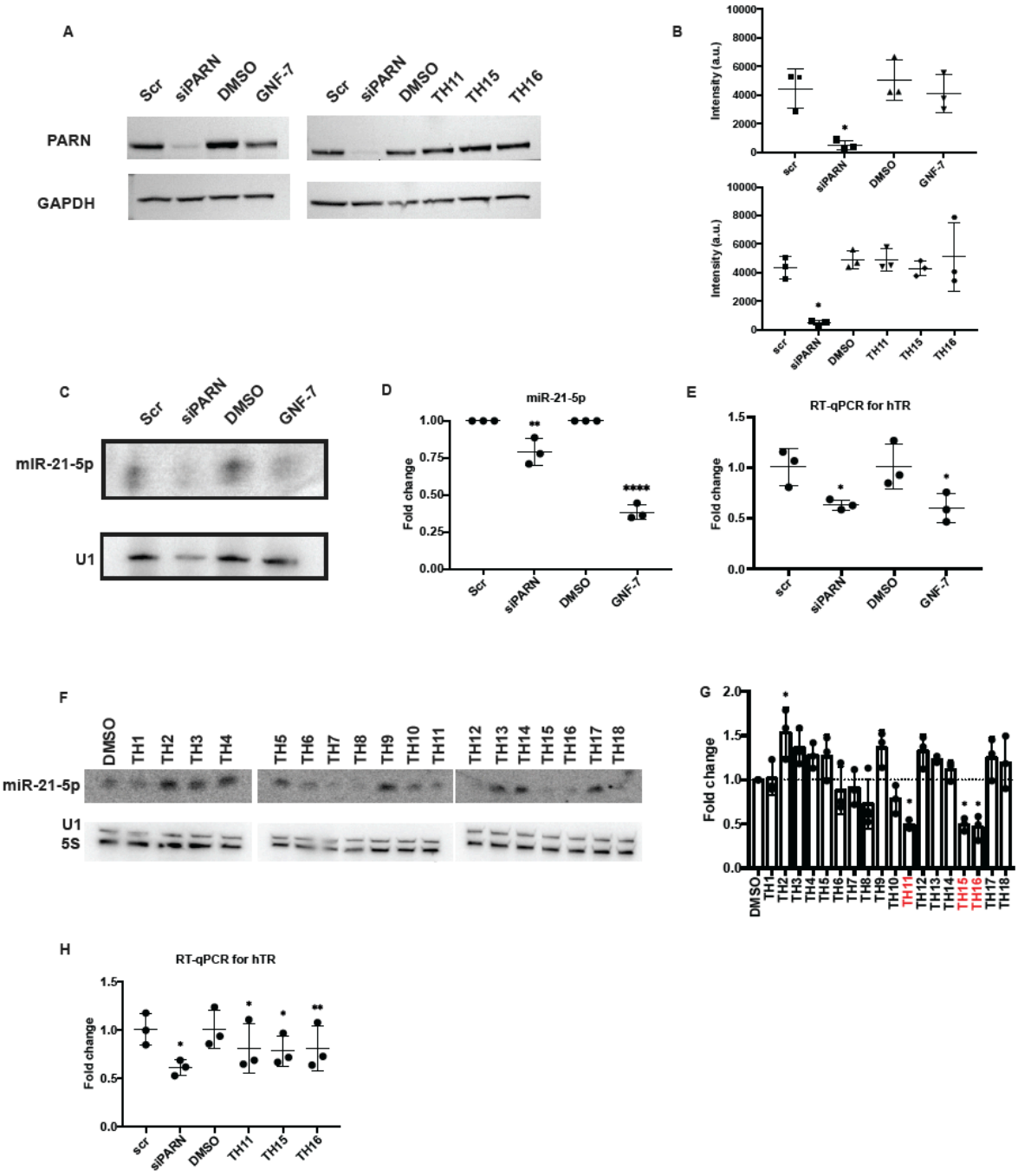
A
Scr
siPARN
DMSO
GNF-7
Scr
siPARN
DMSO
TH11
TH15
TH16
PARN
GAPDH
B
Intensity (a.u.)
scr
siPARN
DMSO
GNF-7
Intensity (a.u.)
scr
siPARN
DMSO
TH11
TH15
TH16
C
Scr
siPARN
DMSO
GNF-7
miR-21-5p
U1
D
miR-21-5p
Fold change
Scr
siPARN
DMSO
GNF-7
E
RT-qPCR for hTR
Fold change
scr
siPARN
DMSO
GNF-7
F
DMSO
TH1
TH2
TH3
TH4
TH5
TH6
TH7
TH8
TH9
TH10
TH11
TH12
TH13
TH14
TH15
TH16
TH17
TH18
miR-21-5p
U1
5S
G
Fold change
DMSO
TH1
TH2
TH3
TH4
TH5
TH6
TH7
TH8
TH9
TH10
TH11
TH12
TH13
TH14
TH15
TH16
TH17
TH18
H
RT-qPCR for hTR
Fold change
scr
siPARN
DMSO
TH11
TH15
TH16

Figure 3.7. GNF-7, TH11, TH15, and TH16 inhibit PARN in cells.

(**A**) Representative western blots showing GNF-7, TH11, TH15, and TH16 treatments do not affect PARN level. Hela cells were treated with siPARN and 50 μM GNF-7 (or 10 μM TH11, TH15, or TH16) (scramble siRNA and DMSO as controls) for 2 days before lysed. The blot was blotted against anti-PARN antibody. (**B**) Quantification of the changes in PARN levels of western blot using GAPDH as loading controls. siPARN and drug treatments were normalized to scramble siRNA and DMSO controls, respectively. siPARN and drug treatment data were compared to scr and DMSO data, respectively. One-way ANOVA, multiple comparisons test. Average +/-SD, N=3 biological replicates, n=1. (**C**) Representative northern blot showing that miR-21-5p levels decreased in both PARN KD and GNF-7 treatment. Hela cells were treated with siPARN and 50 μM GNF-7 (scramble siRNA and DMSO as controls) for 2 days before RNA extraction. (**D**) Quantification of miR-21-5p levels normalized to U1 RNA. One-way ANOVA, multiple comparisons test, average +/- SD, N=3 biological replicates, n=1. (**E**) RT-qPCR showing that hTR levels reduced in siPARN and GNF-7 treatments compared to scr and DMSO controls, respectively. One-way ANOVA, multiple comparisons test, average +/- SD, N=3 biological replicates, n=2. (**F**) Representative northern blot showing that miR-21-5p levels decreased in TH11, TH15, and TH16 treatments. Hela cells were treated with 10 μM of TH1-TH18 (DMSO as control) for 2 days before RNA extraction. (**G**) Quantification of miR-21-5p levels normalized to U1 RNA. One-way ANOVA, multiple comparisons test, average +/- SD, N=3 biological replicates, n=1. (**H**) RT-qPCR showing that hTR levels reduced in siPARN and drug treatments compared to scr and DMSO controls, respectively. One-way ANOVA, multiple comparisons test, average +/- SD, N=3 biological replicates, n=2. For nothern blot and RT-qPCR quantifications, Scr and DMSO controls were independently set to 1 and used as control for siPARN and drug treatments, respectively. *P<0.05, **P<0.005, ***P<0.001, ****P<0.0001, n.s. was not indicated. Full blots are presented in **Appendix Figure A.13**.

Previous work has shown that PARN inhibition leads to cell death in combination with DNA damaging agent, which has been interpreted to occur through the induction of p53 [24]. Given this, we examined if GNF-7, TH11, TH15, or TH16 affected cell growth either by themselves or in combination with the chemotherapeutic agent, doxorubicin. We observed that at 25 μM GNF-7 and 10 μM of TH11, TH15, and TH16, Hela cells showed growth defects compared to DMSO treatment (**Figure 3.8A and C**). More importantly, we observed that both PARN KD (as previously shown) and cells treated with these compounds showed increased cell death after 24 hours of doxorubicin treatment compared to the scramble siRNA and DMSO controls (**Figure 3.8B and D**). This indicates that GNF-7, TH11, TH15, and TH16 increase the sensitivity of cells to the chemotherapeutic agent, possibly through upregulating p53.

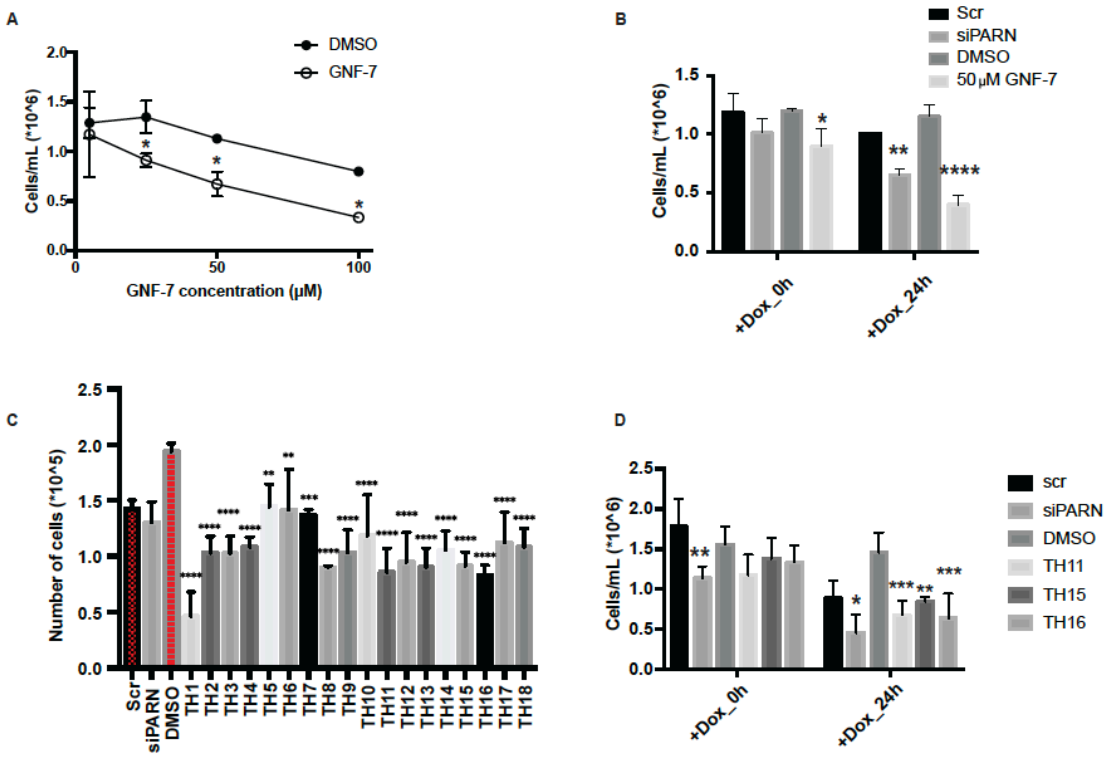

Figure 3.8. Cell death assay for GNF-7 treatment.

(**A**) Numbers of cells at 2 days after DMSO and GNF-7 treatment. 2-way ANOVA, multiple comparisons test, average +/- SD, N=3 biological replicates, n =1. (**B**) Numbers of cells at 0 and 24h-post doxorubicin treatment. Hela cells were treated with siPARN or GNF-7 for 2 days (scramble siRNA and DMSO as controls) before adding doxorubicin. Cells were collected for quantification after 0- and 24-h post doxorubicin treatment. 2-way ANOVA, multiple comparisons test, average +/- SD, N=3 biological replicates, n =1. *P<0.05, **P<0.005, ***P<0.001, ****P<0.0001, n.s. was not indicated. (**C**) Numbers of cells at 2 days after DMSO and TH1-TH18 treatment. One-way ANOVA, multiple comparisons test, average +/- SD, N=3 biological replicates, n =1. (**D**) Numbers of cells at 0 and 24h-post doxorubicin treatment. Hela cells were treated with siPARN, TH11, TH15, or TH16 for 2 days (scramble siRNA and DMSO as controls) before adding doxorubicin. Cells were collected for quantification after 0- and 24-h post doxorubicin treatment. 2-way ANOVA, multiple comparisons test, average +/- SD, N=3 biological replicates, n =1. *P<0.05, **P<0.005, ***P<0.001, ****P<0.0001, n.s. was not indicated.

3.4. Discussion

Herein, we report the identification of PARN inhibitors *in vitro* and in cells. PARN was purified and its poly(A) trimming activity was shown to be dose-dependent, which can be measured by a simple fluorescence assay (**Figure 3.3C**). This assay is a useful tool for determining PARN enzymatic activity and for possible drug screen. In computational modeling, we identified several compounds predicted to dock with PARN and tested them using *in vitro* assays (**Figure 3.4 and 3.5**). Moreover, with HTS, we found multiples PARN inhibitors using the fluorescence assay. These together identified GNF-7, a Bcr-Abl inhibitor, TH11, TH15, and TH16 as compounds that inhibit PARN. GNF-7, TH11, TH15, and TH16 were showed to inhibit PARN in a dose-dependent manner with a IC50 of 35 $\pm$ 13, 3.36, 2, and 7.9 μM, respectively, which are significantly lower compared to AMP (**Figure 3.5D, 3.6B-D**) [252]. We also observed these compounds cause phenotypes consistent with PARN inhibition in cells with a reduction in hTR and miR-21-5p RNA levels similar to PARN KD (**Figure 3.7C-H**).

The discovery and development of a selective and effective PARN inhibitor could be a useful tool for cancer treatment. PARN is a processive deadenylase and PARN KD has been shown to upregulate p53 protein in cancer cells, which causes cell-cycle arrest and prevents cell growth and development [24,250]. Thus, targeting PARN may offer a potential therapeutic approach for repressed p53-induced cancers. Previous reports have described aminoglycosides, synthetic nucleotides with fluoro-glucopyranosyl sugar moiety and benzoyl-modified cytosine or adenine, glucopyranosyl analogs bearing uracil, 5-fluorouracil, or thymine as base moiety, and purine-2,6-dione derivatives as possible

PARN inhibitors (**Appendix Table A.3**), although these compounds required relatively high concentrations and/or have not been shown to inhibit PARN activity in cells [251,253-255]. While some purine-2,6-dione derivatives showed PARN inhibition at relatively low concentrations: 30 μM (5b, 8a-d, and 8f), 10 μM (5j and 5k), and 3 μM (8e and 8j) using a similar fluorescence assay, only five IC50 values were reported with the lowest value of 23.9 ± 3.7 μM (compound 8j) (**Appendix Table A.3**) [255]. The IC50 of compound 8j is slightly lower than that of GNF-7, suggesting compound 8j may be a good candidate for PARN inhibitor as well. The remainder of these previously identified PARN inhibitors were either tested with a different substrate (poly(A) or their IC50s were not determined making a direct comparison between the effectiveness of these inhibitors on the activity of PARN difficult [251,253-255].

From our assays, we identified the pyrimidopyrimidin-2-one GNF-7, TH11, TH15, and TH16 as PARN inhibitors. All the compounds are kinase inhibitors. GNF-7 is considered a multi-kinase inhibitor, but it is not a broad-spectrum kinase inhibitor [259]. GNF-7 is a potent inhibitor of Bcr-Abl tyrosine kinase, ACK1 (activated CDC42 kinase 1), and GCK (germinal center kinase) with IC50s of 133 nM, 25 nM, and 8 nM, respectively [258,260]. This is not unexpected since most kinase inhibitors are ATP mimetics; however, our studies support that GNF-7, TH11, TH15, and TH16 inhibit PARN activity and could be used as lead compounds for structure-activity study to develop PARN inhibitors with improved potency and selectivity.

Several observations argue GNF-7, TH11, TH15, and TH16 can inhibit PARN in

cells. First, these drug treatments of cells decreased the levels of hTR and miR-21-5p (**Figure 3.7C-H**), as is seen in PARN- deficient cells [22,24,26,27,129]. Second, we observed that GNF-7, TH11, TH15, and TH16 acted similarly to siRNA KD of PARN at increasing cell death in the presence of doxorubicin (**Figure 3.8B and D**). Taken together, we propose that GNF-7, TH11, TH15, and TH16 can be used as chemical tools for the inhibition of PARN both *in vitro* and in cells. However, since these compounds can inhibit a range of kinases, finding additional PARN inhibitors, or developing derivatives of these compounds with more selectivity for PARN is an important future area of future research.

3.5. Materials and Methods

Computational-based library docking

The SelleckChem kinase inhibitor library (SelleckChem, Cat. No. L1200) consisting of 1,820 compounds was docked into active site of the 2.6 Å human PARN nuclease domain crystal structure (PDB: 2A1R) [90], using the Glide module within Schrödinger (Release 2020-3, Schrödinger LLC, New York, NY) [261-263]. Prior to docking, the water molecules were removed, and the proteins were prepared by assigning bond orders, adding hydrogens, and repairing any side chains or missing amino acid sequences. To complete protein preparation a restrained minimization of the protein structure was performed using the default constraint of 0.30 Å RMSD and the OPLS_2005 force field [264]. The prepared protein was subjected to SiteMap analysis [263], that identified the catalytic binding site and docking grids were generated using Receptor Grid Generation. The compounds in the SelleckChem kinase inhibitor library were prepared using LigPrep by generating possible states at the target pH 7.0 using Epik and minimized

by applying the OPLS_2005 force field [264]. Molecular docking simulations were performed using the Glide ligand docking module in XP (extra precision) mode and included post-docking minimization [262]. The docked structures were examined and high-ranked compounds with favorable XP GScores for ligand binding, that displayed interaction with residues Asp28-Phe31, the divalent metal cation binding site within the active site (**Figure 3.4**), were selected for evaluation. The XP GScore is an empirical scoring function that approximates the ligand binding free energy; therefore, a more negative value represents favorable binding.

High-throughput screening

2 µL of protein (100 nM final concentration) (stock protein was diluted in 1X lysis buffer (HEPES KOH, pH 7.4, 30 mM, KOAc 100 mM, and $Mg(OAc)_2$ 2 mM) was added to wells using offline Multidrop Combi nL. The reaction was pre-incubated with 12.5 nL of Sygnature library (Enamine kinase library (HBL-24) (31.25 µM) for 15 minutes before 2 µL of RNA (10 µM) was added (DMSO was added to control wells using Echo 655). The reaction was incubated at 22°C for 20 minutes in Cytomat automatic incubator. After the incubation, the reaction was quenched by adding 4 µL of quencher solution (30 µM of 3'-BHQ labeled quench DNA in 1% SDS) using Multidrop Combi nL. The quenched reaction was incubated at room temperature for 10 minutes and fluorescence was measured using PHERAstar FSX (λ485/520). For the counter screen, no protein was added to the reaction.

For active potency, dilution series of 10 mM of kinase library compounds (8 points 1:3 dilution, final top concentration was 100 μM) was used to generate IC50 curves. Curves were fitted within Genedata using SmartFit algorithm.

Plasmids and Purification of recombinant PARN

Human PARN ORF was codon-optimized using iDT codon optimizer tool for bacterial expression and the corresponding gene block fragment was purchased from iDT. PcoldI-PARN plasmid with Chloramphenicol resistance containing the full-length human PARN ORF was a kind gift from Professor Yukihide Tomari [241]. Full-length PARN ORF was cut from the Pcold-PARN plasmid using NdeI-XhoI restriction digest and the native vector was gel purified. PARN 1-430 ORF fragment was PCR amplified from the gene block using the following primers and gel purified.

Fwd primer: TAAGCACATATGATGGAAATCATTCGCTCC

Rev primer: TGCTTACTCGAGTTAAATGTCCATCACACGCA

The purified PCR product was ligated to the PcoldI NdeI-XhoI digest vector using T4 DNA ligase I (NEB M0202S) and correct insertion was verified using Sanger sequencing. PARN D28A F31A double mutant was created by site-directed mutagenesis of the PARN 1-430 expressing plasmid using the following primers and mutation insertion was verified using sanger sequencing.

Fwd primer: TTTTTTGCAATTGCAGGGGAGGCTTCCGGTATTTCC

Rev primer: GGAAATACCGGAAGCCTCCCCTGCAATTGCAAAAAA

For recombinant protein purification, the vector was expressed in Rosetta 2 DE at 37^{o}C overnight with Amp-Camp (50 µg/mL). The starter culture was transferred into 1 L of TB culture and incubated at 37^{o}C to reach O.D. of 1. The proteins were induced with 1 mM IPTG for 2 days at 15^{o}C. The proteins were purified using Ni-NTA column and buffer exchanged into storage buffer (30 mM Hepes KOH, pH 7.4, 100 mM KOAc, 2 mM $Mg(OAc)_2$, 30% glycerol, 1 mM TCEP). Proteins were verified on SDS gels and stored at -80^{o}C.

siRNAs

siRNAs targeting PARN (siGenome) was purchased from Dharmacon in the Smartpool formulation (M-011348-00-0005). All-stars negative control siRNA from QIAGEN (SI03650318) was used as negative control.

Cell culture

HeLa cells were purchased from ATCC (CCL2) and verified for absence of mycoplasma contamination. HeLa cells were cultured in DMEM containing 10% FBS, 1% Pen/Strep, at 37^{o}C under ambient conditions.

HeLa cells were seeded ~100,000 cells/well in a six-well plate 24 hours before transfection/GNF-7 (50 µM) treatment. siRNA transfection was performed using Lipofectamin RNAiMAX (Thermo Fisher Scientific) as per manufacturer's protocol. 48 hours after transfection/drug treatment, cells were collected for either RNA or protein analysis.

RNA extraction and Northern blotting

Total RNA was extracted from cell lysates using TriZol as per manufacturer's protocol and DNAse treated. After quantification on Nanodrop, total RNA was separated on an acrylamide 7 M Urea gel. RNA was transferred to a nylon membrane (Nytran SPC, GE Healthcare) using semiwet transfer. After UV/EDC crosslinking, the blot was pre-hybridized and hybridized in PerfectHyb Plus Hybridization Buffer (Sigma Aldrich) at 42^{o}C. Northern probes have been previously described [24,265]. After hybridization and washing in 2×SSC 0.1% SDS wash buffer, blots were exposed to a cassette and imaged on a Typhoon FLA 9500 Phosphoimager. Band intensities were quantified using ImageJ and normalized to the U1 levels under each condition.

RT-qPCR

Extracted total RNA was reverse transcribed using Mir-X miRNA first strand synthesis kit (Taraka, Cat # 638315) to make cDNA and qPCR was perfomred with iQ SYBR Green Supermix (BioRad, Cat. No. 1708880) with CGCTGTTTTTCTCGCTGACT (forward primer) and GCTCTAGAATGAACGGTGGAA (reverse primer) for hTR. The RNA levels were normalized using 5S rRNA as a housekeeping gene.

Western blotting

Cells was lysed with 2X lysis buffer (2.5% SDS, 4% BME, protease inhibitor) and was separated on a 4%–12% Bis-Tris NuPage gel (ThermoFisher) and transferred to protran membrane (Amer- sham). After blocking in 5% non-fat milk in 1×TBST, blots were probed with anti-PARN (Abcam, ab188333, 1:1000 dilution) overnight at 4^{o}C and HRP

anti-rabbit goat (Cell Signaling Technology,7074S, 1:1000 dilution) secondary antibody for one hour. Blot was quantified using ImageJ and normalized to GAPDH levels (GAPDH antibody (0411) HRP) (Santa Cruz Biotechnology, sc-47724 HRP).

Inhibition fluorescence assay

1 µL of protein (73 nM as final concentration) (stock protein is diluted in 1X lysis buffer (HEPES KOH, pH 7.4, 30 mM, KOAc 100 mM, and $Mg(Oac)_2$ 2 mM) was added to 4 µL of 2.5X reaction buffer (Tris-HCl pH 7.4, 10 mM, KCl 50 mM, $MgCl_2$ 5 mM). If drug was added, reaction was pre-incubated with drugs for 10 minutes before 5 µL of RNA (5 µM as final concentration) was added. The reaction was incubated at 37^{o}C for 20 minutes. After the incubation, the reaction was either diluted with 2X loading buffer and heated to 95^{o}C for 5 minutes for gel or quenched by adding 10 µL of quencher solution (30 µM of 3'-BHQ labeled quench DNA in 1% SDS). Quenched reaction was incubated at room temperature for 10-60 minutes and fluorescence was measured using Fluorescein wavelength measurement.

Gels

15% TBE-Urea gel (Thermo Fisher Scientific) was prerun at 20W for 30 minutes. RNAs from the reaction was loaded into 15% TBE gels and run at 300 V for 35 minutes. The gel was visualized using iBright (Invitrogen FL1500).

Cell death assay

The same number of Hela cells were seed into 6 well-plates and treated with GNF-7 (SelleckChem, S8140) or transfected for 2 days. Cell counting were done 2 days post-treatment. For doxorubicin (EMD Millipore, 504042) treatment, doxorubicin (1 μM) was added to cells. Cells were collected and counted at 0h and 24h after treatment.

3.6. Acknowledgements

The authors thank members of the Parker lab for their suggestions and feed-back and Cell Culture Core for technical assistance. This work was supported by funds from HHMI and funds from the Colorado Office of Economic Development (DO-2020-2463).

CHAPTER IV

Summary and Future directions

4.1. Summary

In this thesis, we examined two different aspects of RNA regulation. The first was to further our understanding of the molecular mechanisms for how mRNAs are targeted to SGs and the second one was to identify potential inhibitors for PARN, a deadenylase that is involved in ncRNA regulation in mammalian cells.

RNA partitioning into stress granules is based on a summation of multiple interactions (Chapter II)

Stress granules (SGs) are membrane-less organelles which form when translation initiation is inhibited. While there is model suggesting that mRNAs are selectively sorted into SGs for gene expression regulation, the rules that dictate RNA partitioning into SGs are unknown. Here, we showed several observations which suggest that SG recruitment of an RNA is based on the summative effects of RNA-RNA, RNA-protein, and protein-protein interactions.

First, we showed that SG enrichment is a dominant effect. By inserting SG-enriched *NORAD* RNA into the 3' UTR of SG-depleted *luciferase* RNA reporter, we observed that *NORAD* RNA can target reporter RNA to SGs efficiently. This suggests that *NORAD* contains one or more elements that promote SG recruitment of an RNP. Second, there is a correlation between SG RNA-binding proteins (RBPs) and RNA recruitment to SGs, suggesting that RBPs play a role in targeting RNA to SGs. Third, tethering reporter RNA to SG RNA-binding proteins, G3PB1, TIA-1, or FMRP, can increase its SG recruitment in a dose-dependent manner. We also discovered that SG transcriptome is

largely unchanged upon G3BP1/2 DKO. Altogether, the data indicates that RNP partitioning into SGs is insensitive to individual protein but rather based on the summation of RNA-RNA, RNA-protein, and protein-protein interactions.

Identification of PARN nuclease activity inhibitors by computational-based docking and high-throughput screening (Chapter III)

Poly(A)-specific ribonuclease (PARN) is a 3' to 5' exoribonuclease that removes the 3' end of RNAs. PARN enhances the stability of ncRNAs including hTR, Y RNAs, and miRNAs by removing 3' oligo(A) tails, thus limiting the access of exonucleases. A recent study showed that PARN depletion leads to the destabilization of multiple miRNAs that target p53, thus upregulating p53. Since p53 is a tumor suppressor, PARN inhibitors can be a useful therapeutic treatment for cancers caused by repressed p53. In this thesis, we identified and validated four novel PARN inhibitors *in vitro* and in cells.

By utilizing computational docking and fluorescence and gel-based assays, we identified GNF-7, TH1-17 as PARN inhibitors *in vitro.* When we tested them in cells, we showed that GNF-7, TH11, TH15, and TH16 reduce hTR and miR-21-5p RNA levels, similar to PARN KD. Moreover, we also showed that GNF-7, TH11, TH15, and TH16 treatments sensitize Hela cells to the chemotherapeutic agent, doxorubicin, similar to PARN KD. These data suggest that these compounds also inhibit PARN in cells.

This study discovered four compounds that can be used as lead compounds for development of PARN inhibitors with improved selectivity and potency. PARN inhibitors

are useful since they can be used as cancer therapeutic treatments or as a tool to study PARN's functions in cells.

4.2. Future directions

The mechanism for how RNA-RNA interactions recruit RNAs to SGs (Chapter II)

There is emerging evidence suggesting that RNA targeting to SGs is protein-independent (Chapter I). One of the most striking pieces of evidence is that RNAs can form self-assembly in yeast and interestingly, the assembly's transcriptome recapitulates SG's transcriptome (Chapter I). However, while there are studies suggesting that *trans* RNA-RNA interactions are crucial for SG formation and RNA targeting to SGs, there is no direct evidence for *trans* RNA-RNA interactions in SGs. Therefore, further investigation of RNA-RNA interactions in SGs will be essential for understanding how SGs and other RNP granules assemble. For example, one unresolved question is what RNA-RNA interactions exist in SGs and whether there is any specificity to them. Similarly, how this works in more programmed granules, such as neuronal granules, might be of interest.

Development of PARN inhibitors as a cancer therapeutic treatment.

The goal of the work completed in Chapter III was to identify potential PARN inhibitors which can be used for the development of therapeutic treatments to suppress tumor progression by inducing p53 protein levels. Thus, one next step is to test how these compounds affect p53 protein levels in cells. Interestingly, given that telomere length and telomerase activity is crucial for cancer initiation and tumor survival in the large majority of cancer cells [266], and PARN KD leads to reduced hTR levels (Chapter III) [22], PARN's inhibitors may also be used to reduce the growth of multiple cancer cell types. Moreover, since the standard recommendations for chemical probes are that 1) they have 30-fold selectivity compared to other enzymes in the same category, 2) potency is better than

100 nM in vitro, and 3) they display on-target activity in cells at a concentration of 1 μM or better (Structural Genomics Consortium, www.thesgc.org), it will be important to do medicinal chemistry on these compounds to increase their affinity and decrease any potential off-target effects.

REFERENCES

1 Lu, P., Vogel, C., Wang, R., Yao, X. & Marcotte, E. M. Absolute protein expression profiling estimates the relative contributions of transcriptional and translational regulation. *Nat Biotechnol* **25**, 117-124, doi:10.1038/nbt1270 (2007).

2 Yan, Y. B. Deadenylation: enzymes, regulation, and functional implications. *Wiley Interdiscip Rev RNA* **5**, 421-443, doi:10.1002/wrna.1221 (2014).

3 Darnell, J. E., Philipson, L., Wall, R. & Adesnik, M. Polyadenylic acid sequences: role in conversion of nuclear RNA into messenger RNA. *Science* **174**, 507-510, doi:10.1126/science.174.4008.507 (1971).

4 Edmonds, M., Vaughan, M. H. & Nakazato, H. Polyadenylic acid sequences in the heterogeneous nuclear RNA and rapidly-labeled polyribosomal RNA of HeLa cells: possible evidence for a precursor relationship. *Proc Natl Acad Sci U S A* **68**, 1336-1340, doi:10.1073/pnas.68.6.1336 (1971).

5 Niwa, M., Rose, S. D. & Berget, S. M. In vitro polyadenylation is stimulated by the presence of an upstream intron. *Genes Dev* **4**, 1552-1559, doi:10.1101/gad.4.9.1552 (1990).

6 Wassarman, K. M. & Steitz, J. A. Association with terminal exons in pre-mRNAs: a new role for the U1 snRNP? *Genes Dev* **7**, 647-659, doi:10.1101/gad.7.4.647 (1993).

7 Dreyfus, M. & Régnier, P. The poly(A) tail of mRNAs: bodyguard in eukaryotes, scavenger in bacteria. *Cell* **111**, 611-613, doi:10.1016/s0092-8674(02)01137-6 (2002).

8 Łabno, A., Tomecki, R. & Dziembowski, A. Cytoplasmic RNA decay pathways - Enzymes and mechanisms. *Biochim Biophys Acta* **1863**, 3125-3147, doi:10.1016/j.bbamcr.2016.09.023 (2016).

9 Sprinzl, M. & Cramer, F. The -C-C-A end of tRNA and its role in protein biosynthesis. *Prog Nucleic Acid Res Mol Biol* **22**, 1-69, doi:10.1016/s0079-6603(08)60798-9 (1979).

10 Deutscher, M. P. & Ni, R. C. Purification of a low molecular weight form of rat liver arginyl-tRNA synthetase. *J Biol Chem* **257**, 6003-6006 (1982).

11 Reddy, R., Henning, D., Das, G., Harless, M. & Wright, D. The capped U6 small nuclear RNA is transcribed by RNA polymerase III. *J Biol Chem* **262**, 75-81 (1987).

12 Heo, I. *et al.* Lin28 mediates the terminal uridylation of let-7 precursor MicroRNA. *Mol Cell* **32**, 276-284, doi:10.1016/j.molcel.2008.09.014 (2008).

13 LaCava, J. *et al.* RNA degradation by the exosome is promoted by a nuclear polyadenylation complex. *Cell* **121**, 713-724, doi:10.1016/j.cell.2005.04.029 (2005).

14 Vanácová, S. *et al.* A new yeast poly(A) polymerase complex involved in RNA quality control. *PLoS Biol* **3**, e189, doi:10.1371/journal.pbio.0030189 (2005).

15 Wyers, F. *et al.* Cryptic pol II transcripts are degraded by a nuclear quality control pathway involving a new poly(A) polymerase. *Cell* **121**, 725-737, doi:10.1016/j.cell.2005.04.030 (2005).

16 Marzluff, W. F. & Koreski, K. P. Birth and Death of Histone mRNAs. *Trends Genet* **33**, 745-759, doi:10.1016/j.tig.2017.07.014 (2017).

17 Jia, H. *et al.* The RNA helicase Mtr4p modulates polyadenylation in the TRAMP complex. *Cell* **145**, 890-901, doi:10.1016/j.cell.2011.05.010 (2011).

18 Hagan, J. P., Piskounova, E. & Gregory, R. I. Lin28 recruits the TUTase Zcchc11 to inhibit let-7 maturation in mouse embryonic stem cells. *Nat Struct Mol Biol* **16**, 1021-1025, doi:10.1038/nsmb.1676 (2009).

19 Chang, H. M., Triboulet, R., Thornton, J. E. & Gregory, R. I. A role for the Perlman syndrome exonuclease Dis3l2 in the Lin28-let-7 pathway. *Nature* **497**, 244-248, doi:10.1038/nature12119 (2013).

20 Ustianenko, D. *et al.* Mammalian DIS3L2 exoribonuclease targets the uridylated precursors of let-7 miRNAs. *RNA* **19**, 1632-1638, doi:10.1261/rna.040055.113 (2013).

21 Rissland, O. S. & Norbury, C. J. Decapping is preceded by 3' uridylation in a novel pathway of bulk mRNA turnover. *Nat Struct Mol Biol* **16**, 616-623, doi:10.1038/nsmb.1601 (2009).

22 Shukla, S., Schmidt, J. C., Goldfarb, K. C., Cech, T. R. & Parker, R. Inhibition of telomerase RNA decay rescues telomerase deficiency caused by dyskerin or PARN defects. *Nat Struct Mol Biol* **23**, 286-292, doi:10.1038/nsmb.3184 (2016).

23 Shukla, S. & Parker, R. PARN Modulates Y RNA Stability and Its 3'-End Formation. *Mol Cell Biol* **37**, doi:10.1128/MCB.00264-17 (2017).

24 Shukla, S., Bjerke, G. A., Muhlrad, D., Yi, R. & Parker, R. The RNase PARN Controls the Levels of Specific miRNAs that Contribute to p53 Regulation. *Mol Cell* **73**, 1204-1216.e1204, doi:10.1016/j.molcel.2019.01.010 (2019).

25 Nguyen, D. *et al.* A Polyadenylation-Dependent 3' End Maturation Pathway Is Required for the Synthesis of the Human Telomerase RNA. *Cell Rep* **13**, 2244-2257, doi:10.1016/j.celrep.2015.11.003 (2015).

26 Tseng, C. K. *et al.* Human Telomerase RNA Processing and Quality Control. *Cell Rep* **13**, 2232-2243, doi:10.1016/j.celrep.2015.10.075 (2015).

27 Moon, D. H. *et al.* Poly(A)-specific ribonuclease (PARN) mediates 3'-end maturation of the telomerase RNA component. *Nat Genet* **47**, 1482-1488, doi:10.1038/ng.3423 (2015).

28 Boele, J. *et al.* PAPD5-mediated 3' adenylation and subsequent degradation of miR-21 is disrupted in proliferative disease. *Proc Natl Acad Sci U S A* **111**, 11467-11472, doi:10.1073/pnas.1317751111 (2014).

29 Berndt, H. *et al.* Maturation of mammalian H/ACA box snoRNAs: PAPD5-dependent adenylation and PARN-dependent trimming. *RNA* **18**, 958-972, doi:10.1261/rna.032292.112 (2012).

30 Son, A., Park, J. E. & Kim, V. N. PARN and TOE1 Constitute a 3' End Maturation Module for Nuclear Non-coding RNAs. *Cell Rep* **23**, 888-898, doi:10.1016/j.celrep.2018.03.089 (2018).

31 Jeong, H. C. *et al.* USB1 is a miRNA deadenylase that regulates hematopoietic development. *Science* **379**, 901-907, doi:10.1126/science.abj8379 (2023).

32 Lardelli, R. M. *et al.* Biallelic mutations in the 3' exonuclease TOE1 cause pontocerebellar hypoplasia and uncover a role in snRNA processing. *Nat Genet* **49**, 457-464, doi:10.1038/ng.3762 (2017).

33 Lardelli, R. M. & Lykke-Andersen, J. Competition between maturation and degradation drives human snRNA 3' end quality control. *Genes Dev* **34**, 989-1001, doi:10.1101/gad.336891.120 (2020).

34 Deng, T. *et al.* TOE1 acts as a 3' exonuclease for telomerase RNA and regulates telomere maintenance. *Nucleic Acids Res* **47**, 391-405, doi:10.1093/nar/gky1019 (2019).

35 Ustianenko, D. *et al.* TUT-DIS3L2 is a mammalian surveillance pathway for aberrant structured non-coding RNAs. *EMBO J* **35**, 2179-2191, doi:10.15252/embj.201694857 (2016).

36 Izumi, N. *et al.* Identification and Functional Analysis of the Pre-piRNA 3' Trimmer in Silkworms. *Cell* **164**, 962-973, doi:10.1016/j.cell.2016.01.008 (2016).

37 Tang, W., Tu, S., Lee, H. C., Weng, Z. & Mello, C. C. The RNase PARN-1 Trims piRNA 3' Ends to Promote Transcriptome Surveillance in C. elegans. *Cell* **164**, 974-984, doi:10.1016/j.cell.2016.02.008 (2016).

38 Burris, A. M. *et al.* Hoyeraal-Hreidarsson Syndrome due to PARN Mutations: Fourteen Years of Follow-Up. *Pediatr Neurol* **56**, 62-68.e61, doi:10.1016/j.pediatrneurol.2015.12.005 (2016).

39 Dhanraj, S. *et al.* Bone marrow failure and developmental delay caused by mutations in poly(A)-specific ribonuclease (PARN). *J Med Genet* **52**, 738-748, doi:10.1136/jmedgenet-2015-103292 (2015).

40 Stuart, B. D. *et al.* Exome sequencing links mutations in PARN and RTEL1 with familial pulmonary fibrosis and telomere shortening. *Nat Genet* **47**, 512-517, doi:10.1038/ng.3278 (2015).

41 Tummala, H. *et al.* Poly(A)-specific ribonuclease deficiency impacts telomere biology and causes dyskeratosis congenita. *J Clin Invest* **125**, 2151-2160, doi:10.1172/JCI78963 (2015).

42 Concolino, D. *et al.* Clericuzio-type poikiloderma with neutropenia syndrome in three sibs with mutations in the C16orf57 gene: delineation of the phenotype. *Am J Med Genet A* **152A**, 2588-2594, doi:10.1002/ajmg.a.33600 (2010).

43 Volpi, L. *et al.* Targeted next-generation sequencing appoints c16orf57 as clericuzio-type poikiloderma with neutropenia gene. *Am J Hum Genet* **86**, 72-76, doi:10.1016/j.ajhg.2009.11.014 (2010).

44 Tanaka, A. *et al.* Identification of a homozygous deletion mutation in C16orf57 in a family with Clericuzio-type poikiloderma with neutropenia. *Am J Med Genet A* **152A**, 1347-1348, doi:10.1002/ajmg.a.33455 (2010).

45 Wang, C., Ge, Y., Li, R., He, G. & Lin, Y. Novel compound heterozygous missense variants in TOE1 gene associated with pontocerebellar hypoplasia type 7. *Gene* **862**, 147250, doi:10.1016/j.gene.2023.147250 (2023).

46 Zhang, D. *et al.* Homozygous Rare PARN Missense Mutation in Familial Pulmonary Fibrosis. *Am J Respir Crit Care Med* **199**, 797-799, doi:10.1164/rccm.201809-1632LE (2019).

47 Kropski, J. A. *et al.* Rare Genetic Variants in PARN Are Associated with Pulmonary Fibrosis in Families. *Am J Respir Crit Care Med* **196**, 1481-1484, doi:10.1164/rccm.201703-0635LE (2017).

48 Walne, A. J., Vulliamy, T., Beswick, R., Kirwan, M. & Dokal, I. Mutations in C16orf57 and normal-length telomeres unify a subset of patients with dyskeratosis congenita, poikiloderma with neutropenia and Rothmund-Thomson syndrome. *Hum Mol Genet* **19**, 4453-4461, doi:10.1093/hmg/ddq371 (2010).

49 Walne, A. J. *et al.* Marked overlap of four genetic syndromes with dyskeratosis congenita confounds clinical diagnosis. *Haematologica* **101**, 1180-1189, doi:10.3324/haematol.2016.147769 (2016).

50 Matheny, T., Van Treeck, B., Huynh, T. N. & Parker, R. RNA partitioning into stress granules is based on the summation of multiple interactions. *RNA* **27**, 174-189, doi:10.1261/rna.078204.120 (2021).

51 Van Treeck, B. & Parker, R. Emerging Roles for Intermolecular RNA-RNA Interactions in RNP Assemblies. *Cell* **174**, 791-802, doi:10.1016/j.cell.2018.07.023 (2018).

52 Mao, Y. S., Zhang, B. & Spector, D. L. Biogenesis and function of nuclear bodies. *Trends Genet* **27**, 295-306, doi:10.1016/j.tig.2011.05.006 (2011).

53 Protter, D. S. W. & Parker, R. Principles and Properties of Stress Granules. *Trends Cell Biol* **26**, 668-679, doi:10.1016/j.tcb.2016.05.004 (2016).

54 Parker, R. & Sheth, U. P bodies and the control of mRNA translation and degradation. *Mol Cell* **25**, 635-646, doi:10.1016/j.molcel.2007.02.011 (2007).

55 Schisa, J. A. New insights into the regulation of RNP granule assembly in oocytes. *Int Rev Cell Mol Biol* **295**, 233-289, doi:10.1016/B978-0-12-394306-4.00013-7 (2012).

56 Buchan, J. R. mRNP granules. Assembly, function, and connections with disease. *RNA Biol* **11**, 1019-1030, doi:10.4161/15476286.2014.972208 (2014).

57 McCann, C. *et al.* The Ataxin-2 protein is required for microRNA function and synapse-specific long-term olfactory habituation. *Proc Natl Acad Sci U S A* **108**, E655-662, doi:10.1073/pnas.1107198108 (2011).

58 Krichevsky, A. M. & Kosik, K. S. Neuronal RNA granules: a link between RNA localization and stimulation-dependent translation. *Neuron* **32**, 683-696, doi:10.1016/s0896-6273(01)00508-6 (2001).

59 Advani, V. M. & Ivanov, P. Translational Control under Stress: Reshaping the Translatome. *Bioessays* **41**, e1900009, doi:10.1002/bies.201900009 (2019).

60 Buchan, J. R., Kolaitis, R. M., Taylor, J. P. & Parker, R. Eukaryotic stress granules are cleared by autophagy and Cdc48/VCP function. *Cell* **153**, 1461-1474, doi:10.1016/j.cell.2013.05.037 (2013).

61 Dewey, C. M. *et al.* TDP-43 aggregation in neurodegeneration: are stress granules the key? *Brain Res* **1462**, 16-25, doi:10.1016/j.brainres.2012.02.032 (2012).

62 Kim, H. J. *et al.* Mutations in prion-like domains in hnRNPA2B1 and hnRNPA1 cause multisystem proteinopathy and ALS. *Nature* **495**, 467-473, doi:10.1038/nature11922 (2013).

63 Li, Y. R., King, O. D., Shorter, J. & Gitler, A. D. Stress granules as crucibles of ALS pathogenesis. *J Cell Biol* **201**, 361-372, doi:10.1083/jcb.201302044 (2013).

64 Ramaswami, M., Taylor, J. P. & Parker, R. Altered ribostasis: RNA-protein granules in degenerative disorders. *Cell* **154**, 727-736, doi:10.1016/j.cell.2013.07.038 (2013).

65 Mackenzie, I. R. *et al.* TIA1 Mutations in Amyotrophic Lateral Sclerosis and Frontotemporal Dementia Promote Phase Separation and Alter Stress Granule Dynamics. *Neuron* **95**, 808-816.e809, doi:10.1016/j.neuron.2017.07.025 (2017).

66 Mittag, T. & Parker, R. Multiple Modes of Protein-Protein Interactions Promote RNP Granule Assembly. *J Mol Biol* **430**, 4636-4649, doi:10.1016/j.jmb.2018.08.005 (2018).

67 Mazumder, R., Iyer, L. M., Vasudevan, S. & Aravind, L. Detection of novel members, structure-function analysis and evolutionary classification of the 2H phosphoesterase superfamily. *Nucleic Acids Res* **30**, 5229-5243, doi:10.1093/nar/gkf645 (2002).

68 Shchepachev, V., Wischnewski, H., Missiaglia, E., Soneson, C. & Azzalin, C. M. Mpn1, mutated in poikiloderma with neutropenia protein 1, is a conserved 3'-to-5' RNA exonuclease processing U6 small nuclear RNA. *Cell Rep* **2**, 855-865, doi:10.1016/j.celrep.2012.08.031 (2012).

69 Arn, E. A. & Abelson, J. N. The 2'-5' RNA ligase of Escherichia coli. Purification, cloning, and genomic disruption. *J Biol Chem* **271**, 31145-31153, doi:10.1074/jbc.271.49.31145 (1996).

70 Hofmann, A. *et al.* Structure and mechanism of activity of the cyclic phosphodiesterase of Appr>p, a product of the tRNA splicing reaction. *EMBO J* **19**, 6207-6217, doi:10.1093/emboj/19.22.6207 (2000).

71 Kato, M. *et al.* Crystal structure of the 2'-5' RNA ligase from Thermus thermophilus HB8. *J Mol Biol* **329**, 903-911, doi:10.1016/s0022-2836(03)00448-0 (2003).

72 Sawaya, R., Schwer, B. & Shuman, S. Genetic and biochemical analysis of the functional domains of yeast tRNA ligase. *J Biol Chem* **278**, 43928-43938, doi:10.1074/jbc.M307839200 (2003).

73 Remus, B. S., Jacewicz, A. & Shuman, S. Structure and mechanism of E. coli RNA 2',3'-cyclic phosphodiesterase. *RNA* **20**, 1697-1705, doi:10.1261/rna.046797.114 (2014).

74 Nomura, Y., Roston, D., Montemayor, E. J., Cui, Q. & Butcher, S. E. Structural and mechanistic basis for preferential deadenylation of U6 snRNA by Usb1. *Nucleic Acids Res* **46**, 11488-11501, doi:10.1093/nar/gky812 (2018).

75 Hilcenko, C. *et al.* Aberrant 3' oligoadenylation of spliceosomal U6 small nuclear RNA in poikiloderma with neutropenia. *Blood* **121**, 1028-1038, doi:10.1182/blood-2012-10-461491 (2013).

76 Gao, Y. G., Yao, M., Okada, A. & Tanaka, I. The structure of Pyrococcus horikoshii 2'-5' RNA ligase at 1.94 A resolution reveals a possible open form with a wider active-site cleft. *Acta Crystallogr Sect F Struct Biol Cryst Commun* **62**, 1196-1200, doi:10.1107/S1744309106046616 (2006).

77 Hofmann, A., Grella, M., Botos, I., Filipowicz, W. & Wlodawer, A. Crystal structures of the semireduced and inhibitor-bound forms of cyclic nucleotide phosphodiesterase from Arabidopsis thaliana. *J Biol Chem* **277**, 1419-1425, doi:10.1074/jbc.M107889200 (2002).

78 Gold, M. G., Smith, F. D., Scott, J. D. & Barford, D. AKAP18 contains a phosphoesterase domain that binds AMP. *J Mol Biol* **375**, 1329-1343, doi:10.1016/j.jmb.2007.11.037 (2008).

79 Myllykoski, M., Raasakka, A., Han, H. & Kursula, P. Myelin 2',3'-cyclic nucleotide 3'-phosphodiesterase: active-site ligand binding and molecular conformation. *PLoS One* **7**, e32336, doi:10.1371/journal.pone.0032336 (2012).

80 Myllykoski, M. *et al.* Crystallographic analysis of the reaction cycle of 2',3'-cyclic nucleotide 3'-phosphodiesterase, a unique member of the 2H phosphoesterase family. *J Mol Biol* **425**, 4307-4322, doi:10.1016/j.jmb.2013.06.012 (2013).

81 Didychuk, A. L. *et al.* Usb1 controls U6 snRNP assembly through evolutionarily divergent cyclic phosphodiesterase activities. *Nat Commun* **8**, 497, doi:10.1038/s41467-017-00484-w (2017).

82 Raasakka, A. *et al.* Determinants of ligand binding and catalytic activity in the myelin enzyme 2',3'-cyclic nucleotide 3'-phosphodiesterase. *Sci Rep* **5**, 16520, doi:10.1038/srep16520 (2015).

83 Myllykoski, M. & Kursula, P. Structural aspects of nucleotide ligand binding by a bacterial 2H phosphoesterase. *PLoS One* **12**, e0170355, doi:10.1371/journal.pone.0170355 (2017).

84 Zuo, Y. & Deutscher, M. P. Exoribonuclease superfamilies: structural analysis and phylogenetic distribution. *Nucleic Acids Res* **29**, 1017-1026, doi:10.1093/nar/29.5.1017 (2001).

85 Goldstrohm, A. C. & Wickens, M. Multifunctional deadenylase complexes diversify mRNA control. *Nat Rev Mol Cell Biol* **9**, 337-344, doi:10.1038/nrm2370 (2008).

86 Moser, M. J., Holley, W. R., Chatterjee, A. & Mian, I. S. The proofreading domain of Escherichia coli DNA polymerase I and other DNA and/or RNA exonuclease domains. *Nucleic Acids Res* **25**, 5110-5118, doi:10.1093/nar/25.24.5110 (1997).

87 Bernad, A., Blanco, L., Lázaro, J. M., Martín, G. & Salas, M. A conserved 3'----5' exonuclease active site in prokaryotic and eukaryotic DNA polymerases. *Cell* **59**, 219-228, doi:10.1016/0092-8674(89)90883-0 (1989).

88 Steitz, T. A. & Steitz, J. A. A general two-metal-ion mechanism for catalytic RNA. *Proc Natl Acad Sci U S A* **90**, 6498-6502, doi:10.1073/pnas.90.14.6498 (1993).

89 Ren, Y. G., Martínez, J. & Virtanen, A. Identification of the active site of poly(A)-specific ribonuclease by site-directed mutagenesis and Fe(2+)-mediated cleavage. *J Biol Chem* **277**, 5982-5987, doi:10.1074/jbc.M111515200 (2002).

90 Wu, M. *et al.* Structural insight into poly(A) binding and catalytic mechanism of human PARN. *EMBO J* **24**, 4082-4093, doi:10.1038/sj.emboj.7600869 (2005).

91 De Belle, I., Wu, J. X., Sperandio, S., Mercola, D. & Adamson, E. D. In vivo cloning and characterization of a new growth suppressor protein TOE1 as a direct target gene of Egr1. *J Biol Chem* **278**, 14306-14312, doi:10.1074/jbc.M210502200 (2003).

92 Tucker, M. *et al.* The transcription factor associated Ccr4 and Caf1 proteins are components of the major cytoplasmic mRNA deadenylase in Saccharomyces cerevisiae. *Cell* **104**, 377-386, doi:10.1016/s0092-8674(01)00225-2 (2001).

93 Nousch, M., Techritz, N., Hampel, D., Millonigg, S. & Eckmann, C. R. The Ccr4-Not deadenylase complex constitutes the main poly(A) removal activity in C. elegans. *J Cell Sci* **126**, 4274-4285, doi:10.1242/jcs.132936 (2013).

94 Wagner, E., Clement, S. L. & Lykke-Andersen, J. An unconventional human Ccr4-Caf1 deadenylase complex in nuclear cajal bodies. *Mol Cell Biol* **27**, 1686-1695, doi:10.1128/MCB.01483-06 (2007).

95 Mroczek, S. *et al.* C16orf57, a gene mutated in poikiloderma with neutropenia, encodes a putative phosphodiesterase responsible for the U6 snRNA 3' end modification. *Genes Dev* **26**, 1911-1925, doi:10.1101/gad.193169.112 (2012).

96 Fica, S. M. & Nagai, K. Cryo-electron microscopy snapshots of the spliceosome: structural insights into a dynamic ribonucleoprotein machine. *Nat Struct Mol Biol* **24**, 791-799, doi:10.1038/nsmb.3463 (2017).

97 Kunkel, G. R., Maser, R. L., Calvet, J. P. & Pederson, T. U6 small nuclear RNA is transcribed by RNA polymerase III. *Proc Natl Acad Sci U S A* **83**, 8575-8579, doi:10.1073/pnas.83.22.8575 (1986).

98 Arimbasseri, A. G., Rijal, K. & Maraia, R. J. Transcription termination by the eukaryotic RNA polymerase III. *Biochim Biophys Acta* **1829**, 318-330, doi:10.1016/j.bbagrm.2012.10.006 (2013).

99 Didychuk, A. L., Montemayor, E. J., Brow, D. A. & Butcher, S. E. Structural requirements for protein-catalyzed annealing of U4 and U6 RNAs during di-snRNP assembly. *Nucleic Acids Res* **44**, 1398-1410, doi:10.1093/nar/gkv1374 (2016).

100 Achsel, T. *et al.* A doughnut-shaped heteromer of human Sm-like proteins binds to the 3'-end of U6 snRNA, thereby facilitating U4/U6 duplex formation in vitro. *EMBO J* **18**, 5789-5802, doi:10.1093/emboj/18.20.5789 (1999).

101 Rader, S. D. & Guthrie, C. A conserved Lsm-interaction motif in Prp24 required for efficient U4/U6 di-snRNP formation. *RNA* **8**, 1378-1392, doi:10.1017/s1355838202020010 (2002).

102 Nomura, Y., Montemayor, E. J., Virta, J. M., Hayes, S. M. & Butcher, S. E. Structural basis for the evolution of cyclic phosphodiesterase activity in the U6 snRNA exoribonuclease Usb1. *Nucleic Acids Res* **48**, 1423-1434, doi:10.1093/nar/gkz1177 (2020).

103 Shchepachev, V., Wischnewski, H., Soneson, C., Arnold, A. W. & Azzalin, C. M. Human Mpn1 promotes post-transcriptional processing and stability of U6atac. *FEBS Lett* **589**, 2417-2423, doi:10.1016/j.febslet.2015.06.046 (2015).

104 Patil, P., Uechi, T. & Kenmochi, N. Incomplete splicing of neutrophil-specific genes affects neutrophil development in a zebrafish model of poikiloderma with neutropenia. *RNA Biol* **12**, 426-434, doi:10.1080/15476286.2015.1017240 (2015).

105 Colombo, E. A. *et al.* A zebrafish model of Poikiloderma with Neutropenia recapitulates the human syndrome hallmarks and traces back neutropenia to the myeloid progenitor. *Sci Rep* **5**, 15814, doi:10.1038/srep15814 (2015).

106 Copeland, P. R. & Wormington, M. The mechanism and regulation of deadenylation: identification and characterization of Xenopus PARN. *RNA* **7**, 875-886, doi:10.1017/s1355838201010020 (2001).

107 Körner, C. G. & Wahle, E. Poly(A) tail shortening by a mammalian poly(A)-specific 3'-exoribonuclease. *J Biol Chem* **272**, 10448-10456, doi:10.1074/jbc.272.16.10448 (1997).

108 Martinez, J. *et al.* A 54-kDa fragment of the Poly(A)-specific ribonuclease is an oligomeric, processive, and cap-interacting Poly(A)-specific 3' exonuclease. *J Biol Chem* **275**, 24222-24230, doi:10.1074/jbc.M001705200 (2000).

109 Dehlin, E., Wormington, M., Körner, C. G. & Wahle, E. Cap-dependent deadenylation of mRNA. *EMBO J* **19**, 1079-1086, doi:10.1093/emboj/19.5.1079 (2000).

110 Martînez, J., Ren, Y. G., Nilsson, P., Ehrenberg, M. & Virtanen, A. The mRNA cap structure stimulates rate of poly(A) removal and amplifies processivity of degradation. *J Biol Chem* **276**, 27923-27929, doi:10.1074/jbc.M102270200 (2001).

111 Gao, M., Fritz, D. T., Ford, L. P. & Wilusz, J. Interaction between a poly(A)-specific ribonuclease and the 5' cap influences mRNA deadenylation rates in vitro. *Mol Cell* **5**, 479-488, doi:10.1016/s1097-2765(00)80442-6 (2000).

112 Opyrchal, M., Anderson, J. R., Sokoloski, K. J., Wilusz, C. J. & Wilusz, J. A cell-free mRNA stability assay reveals conservation of the enzymes and mechanisms of mRNA decay between mosquito and mammalian cell lines. *Insect Biochem Mol Biol* **35**, 1321-1334, doi:10.1016/j.ibmb.2005.08.004 (2005).

113 Monecke, T., Schell, S., Dickmanns, A. & Ficner, R. Crystal structure of the RRM domain of poly(A)-specific ribonuclease reveals a novel m(7)G-cap-binding mode. *J Mol Biol* **382**, 827-834, doi:10.1016/j.jmb.2008.07.073 (2008).

114 Liu, W. F., Zhang, A., He, G. J. & Yan, Y. B. The R3H domain stabilizes poly(A)-specific ribonuclease by stabilizing the RRM domain. *Biochem Biophys Res Commun* **360**, 846-851, doi:10.1016/j.bbrc.2007.06.139 (2007).

115 Nagata, T. *et al.* The RRM domain of poly(A)-specific ribonuclease has a noncanonical binding site for mRNA cap analog recognition. *Nucleic Acids Res* **36**, 4754-4767, doi:10.1093/nar/gkn458 (2008).

116 Kim, J. H. & Richter, J. D. Opposing polymerase-deadenylase activities regulate cytoplasmic polyadenylation. *Mol Cell* **24**, 173-183, doi:10.1016/j.molcel.2006.08.016 (2006).

117 Fong, K. W. *et al.* Whole-genome screening identifies proteins localized to distinct nuclear bodies. *J Cell Biol* **203**, 149-164, doi:10.1083/jcb.201303145 (2013).

118 Virtanen, A., Henriksson, N., Nilsson, P. & Nissbeck, M. Poly(A)-specific ribonuclease (PARN): an allosterically regulated, processive and mRNA cap-

interacting deadenylase. *Crit Rev Biochem Mol Biol* **48**, 192-209, doi:10.3109/10409238.2013.771132 (2013).

119 Yoda, M. *et al.* Poly(A)-specific ribonuclease mediates 3'-end trimming of Argonaute2-cleaved precursor microRNAs. *Cell Rep* **5**, 715-726, doi:10.1016/j.celrep.2013.09.029 (2013).

120 Ding, D. *et al.* PNLDC1 is essential for piRNA 3' end trimming and transposon silencing during spermatogenesis in mice. *Nat Commun* **8**, 819, doi:10.1038/s41467-017-00854-4 (2017).

121 Ishikawa, H. *et al.* Poly(A)-specific ribonuclease regulates the processing of small-subunit rRNAs in human cells. *Nucleic Acids Res* **45**, 3437-3447, doi:10.1093/nar/gkw1047 (2017).

122 Montellese, C. *et al.* Poly(A)-specific ribonuclease is a nuclear ribosome biogenesis factor involved in human 18S rRNA maturation. *Nucleic Acids Res* **45**, 6822-6836, doi:10.1093/nar/gkx253 (2017).

123 Nishimura, T. *et al.* PNLDC1, mouse pre-piRNA Trimmer, is required for meiotic and post-meiotic male germ cell development. *EMBO Rep* **19**, doi:10.15252/embr.201744957 (2018).

124 Nishimura, N. *et al.* Isolation and characterization of novel mutants affecting the abscisic acid sensitivity of Arabidopsis germination and seedling growth. *Plant Cell Physiol* **45**, 1485-1499, doi:10.1093/pcp/pch171 (2004).

125 Nishimura, N. *et al.* Analysis of ABA hypersensitive germination2 revealed the pivotal functions of PARN in stress response in Arabidopsis. *Plant J* **44**, 972-984, doi:10.1111/j.1365-313X.2005.02589.x (2005).

126 Reverdatto, S. V., Dutko, J. A., Chekanova, J. A., Hamilton, D. A. & Belostotsky, D. A. mRNA deadenylation by PARN is essential for embryogenesis in higher plants. *RNA* **10**, 1200-1214, doi:10.1261/rna.7540204 (2004).

127 Maragozidis, P. *et al.* Alterations of deadenylase expression in acute leukemias: evidence for poly(a)-specific ribonuclease as a potential biomarker. *Acta Haematol* **128**, 39-46, doi:10.1159/000337418 (2012).

128 Maragozidis, P. *et al.* Poly(A)-specific ribonuclease and Nocturnin in squamous cell lung cancer: prognostic value and impact on gene expression. *Mol Cancer* **14**, 187, doi:10.1186/s12943-015-0457-3 (2015).

129 Roake, C. M. *et al.* Disruption of Telomerase RNA Maturation Kinetics Precipitates Disease. *Mol Cell* **74**, 688-700.e683, doi:10.1016/j.molcel.2019.02.033 (2019).

130 Gao, M., Wilusz, C. J., Peltz, S. W. & Wilusz, J. A novel mRNA-decapping activity in HeLa cytoplasmic extracts is regulated by AU-rich elements. *EMBO J* **20**, 1134-1143, doi:10.1093/emboj/20.5.1134 (2001).

131 Balatsos, N. A., Nilsson, P., Mazza, C., Cusack, S. & Virtanen, A. Inhibition of mRNA deadenylation by the nuclear cap binding complex (CBC). *J Biol Chem* **281**, 4517-4522, doi:10.1074/jbc.M508590200 (2006).

132 Moraes, K. C., Wilusz, C. J. & Wilusz, J. CUG-BP binds to RNA substrates and recruits PARN deadenylase. *RNA* **12**, 1084-1091, doi:10.1261/rna.59606 (2006).

133 Zhang, X. *et al.* PARN deadenylase is involved in miRNA-dependent degradation of TP53 mRNA in mammalian cells. *Nucleic Acids Res* **43**, 10925-10938, doi:10.1093/nar/gkv959 (2015).

134 Lai, W. S., Kennington, E. A. & Blackshear, P. J. Tristetraprolin and its family members can promote the cell-free deadenylation of AU-rich element-containing mRNAs by poly(A) ribonuclease. *Mol Cell Biol* **23**, 3798-3812, doi:10.1128/MCB.23.11.3798-3812.2003 (2003).

135 de Belle, I. *et al.* p53 and Egr-1 additively suppress transformed growth in HT1080 cells but Egr-1 counteracts p53-dependent apoptosis. *Oncogene* **18**, 3633-3642, doi:10.1038/sj.onc.1202696 (1999).

136 Huang, R. P. *et al.* Decreased Egr-1 expression in human, mouse and rat mammary cells and tissues correlates with tumor formation. *Int J Cancer* **72**, 102-109, doi:10.1002/(sici)1097-0215(19970703)72:1<102::aid-ijc15>3.0.co;2-l (1997).

137 Wang, H. *et al.* Knockdown of Toe1 causes developmental arrest during the morula-to-blastocyst transition in mice. *Theriogenology* **194**, 154-161, doi:10.1016/j.theriogenology.2022.10.011 (2022).

138 Sperandio, S. *et al.* TOE1 is an inhibitor of HIV-1 replication with cell-penetrating capability. *Proc Natl Acad Sci U S A* **112**, E3392-3401, doi:10.1073/pnas.1500857112 (2015).

139 Kow, R. L. *et al.* Distinct Poly(A) nucleases have differential impact on sut-2 dependent tauopathy phenotypes. *Neurobiol Dis* **147**, 105148, doi:10.1016/j.nbd.2020.105148 (2021).

140 Colombo, E. A. *et al.* Novel C16orf57 mutations in patients with Poikiloderma with Neutropenia: bioinformatic analysis of the protein and predicted effects of all reported mutations. *Orphanet J Rare Dis* **7**, 7, doi:10.1186/1750-1172-7-7 (2012).

141 Larizza, L., Roversi, G. & Volpi, L. Rothmund-Thomson syndrome. *Orphanet J Rare Dis* **5**, 2, doi:10.1186/1750-1172-5-2 (2010).

142 Kirwan, M. & Dokal, I. Dyskeratosis congenita, stem cells and telomeres. *Biochim Biophys Acta* **1792**, 371-379, doi:10.1016/j.bbadis.2009.01.010 (2009).

143 Mason, P. J. & Bessler, M. The genetics of dyskeratosis congenita. *Cancer Genet* **204**, 635-645, doi:10.1016/j.cancergen.2011.11.002 (2011).

144 Namavar, Y. *et al.* Clinical, neuroradiological and genetic findings in pontocerebellar hypoplasia. *Brain* **134**, 143-156, doi:10.1093/brain/awq287 (2011).

145 NORMAN, R. M. Cerebellar hypoplasia in Werdnig-Hoffmann disease. *Arch Dis Child* **36**, 96-101, doi:10.1136/adc.36.185.96 (1961).

146 Goutières, F., Aicardi, J. & Farkas, E. Anterior horn cell disease associated with pontocerebellar hypoplasia in infants. *J Neurol Neurosurg Psychiatry* **40**, 370-378, doi:10.1136/jnnp.40.4.370 (1977).

147 Barth, P. G. Pontocerebellar hypoplasias. An overview of a group of inherited neurodegenerative disorders with fetal onset. *Brain Dev* **15**, 411-422, doi:10.1016/0387-7604(93)90080-r (1993).

148 Barth, P. G. *et al.* The syndrome of autosomal recessive pontocerebellar hypoplasia, microcephaly, and extrapyramidal dyskinesia (pontocerebellar

hypoplasia type 2): compiled data from 10 pedigrees. *Neurology* **45**, 311-317, doi:10.1212/wnl.45.2.311 (1995).

149 Barth, P. G. Pontocerebellar hypoplasia--how many types? *Eur J Paediatr Neurol* **4**, 161-162, doi:10.1053/ejpn.2000.0294 (2000).

150 Barth, P. G. *et al.* Pontocerebellar hypoplasia type 2: a neuropathological update. *Acta Neuropathol* **114**, 373-386, doi:10.1007/s00401-007-0263-0 (2007).

151 Renbaum, P. *et al.* Spinal muscular atrophy with pontocerebellar hypoplasia is caused by a mutation in the VRK1 gene. *Am J Hum Genet* **85**, 281-289, doi:10.1016/j.ajhg.2009.07.006 (2009).

152 Albrecht, S., Schneider, M. C., Belmont, J. & Armstrong, D. L. Fatal infantile encephalopathy with olivopontocerebellar hypoplasia and micrencephaly. Report of three siblings. *Acta Neuropathol* **85**, 394-399, doi:10.1007/BF00334450 (1993).

153 Budde, B. S. *et al.* tRNA splicing endonuclease mutations cause pontocerebellar hypoplasia. *Nat Genet* **40**, 1113-1118, doi:10.1038/ng.204 (2008).

154 Rajab, A. *et al.* A novel form of pontocerebellar hypoplasia maps to chromosome 7q11-21. *Neurology* **60**, 1664-1667, doi:10.1212/01.wnl.0000068548.58498.41 (2003).

155 Durmaz, B. *et al.* Pontocerebellar hypoplasia type III (CLAM): extended phenotype and novel molecular findings. *J Neurol* **256**, 416-419, doi:10.1007/s00415-009-0094-0 (2009).

156 Patel, M. S., Becker, L. E., Toi, A., Armstrong, D. L. & Chitayat, D. Severe, fetal-onset form of olivopontocerebellar hypoplasia in three sibs: PCH type 5? *Am J Med Genet A* **140**, 594-603, doi:10.1002/ajmg.a.31095 (2006).

157 Edvardson, S. *et al.* Deleterious mutation in the mitochondrial arginyl-transfer RNA synthetase gene is associated with pontocerebellar hypoplasia. *Am J Hum Genet* **81**, 857-862, doi:10.1086/521227 (2007).

158 Rankin, J. *et al.* Pontocerebellar hypoplasia type 6: A British case with PEHO-like features. *Am J Med Genet A* **152A**, 2079-2084, doi:10.1002/ajmg.a.33531 (2010).

159 Anderson, C., Davies, J. H., Lamont, L. & Foulds, N. Early pontocerebellar hypoplasia with vanishing testes: A new syndrome? *Am J Med Genet A* **155A**, 667-672, doi:10.1002/ajmg.a.33897 (2011).

160 Vogiatzi, P., Perdigones, N., Mason, P. J., Wilson, D. B. & Bessler, M. A family with Hoyeraal-Hreidarsson syndrome and four variants in two genes of the telomerase core complex. *Pediatr Blood Cancer* **60**, E4-6, doi:10.1002/pbc.24389 (2013).

161 Bakar, Ö., Işik, U., Canpolat, C. & Alanay, Y. Hoyeraal-Hreidarsson Syndrome: An Extremely Rare Dyskeratosis Congenita Phenotype. *Pediatr Dermatol* **32**, e263-266, doi:10.1111/pde.12693 (2015).

162 Nagpal, N. & Agarwal, S. Telomerase RNA processing: Implications for human health and disease. *Stem Cells*, doi:10.1002/stem.3270 (2020).

163 Clemson, C. M. *et al.* An architectural role for a nuclear noncoding RNA: NEAT1 RNA is essential for the structure of paraspeckles. *Mol Cell* **33**, 717-726, doi:10.1016/j.molcel.2009.01.026 (2009).

164 Mao, Y. S., Sunwoo, H., Zhang, B. & Spector, D. L. Direct visualization of the co-transcriptional assembly of a nuclear body by noncoding RNAs. *Nat Cell Biol* **13**, 95-101, doi:10.1038/ncb2140 (2011).

165 Liu, J., Valencia-Sanchez, M. A., Hannon, G. J. & Parker, R. MicroRNA-dependent localization of targeted mRNAs to mammalian P-bodies. *Nat Cell Biol* **7**, 719-723, doi:10.1038/ncb1274 (2005).

166 Sheth, U. & Parker, R. Decapping and decay of messenger RNA occur in cytoplasmic processing bodies. *Science* **300**, 805-808, doi:10.1126/science.1082320 (2003).

167 Buchan, J. R., Muhlrad, D. & Parker, R. P bodies promote stress granule assembly in Saccharomyces cerevisiae. *J Cell Biol* **183**, 441-455, doi:10.1083/jcb.200807043 (2008).

168 Kedersha, N. *et al.* Dynamic shuttling of TIA-1 accompanies the recruitment of mRNA to mammalian stress granules. *J Cell Biol* **151**, 1257-1268, doi:10.1083/jcb.151.6.1257 (2000).

169 Khong, A. & Parker, R. mRNP architecture in translating and stress conditions reveals an ordered pathway of mRNP compaction. *J Cell Biol* **217**, 4124-4140, doi:10.1083/jcb.201806183 (2018).

170 Khong, A. *et al.* The Stress Granule Transcriptome Reveals Principles of mRNA Accumulation in Stress Granules. *Mol Cell* **68**, 808-820.e805, doi:10.1016/j.molcel.2017.10.015 (2017).

171 Namkoong, S., Ho, A., Woo, Y. M., Kwak, H. & Lee, J. H. Systematic Characterization of Stress-Induced RNA Granulation. *Mol Cell* **70**, 175-187.e178, doi:10.1016/j.molcel.2018.02.025 (2018).

172 Moon, S. L. *et al.* Multicolour single-molecule tracking of mRNA interactions with RNP granules. *Nat Cell Biol* **21**, 162-168, doi:10.1038/s41556-018-0263-4 (2019).

173 Lee, C. S. *et al.* Recruitment of mRNAs to P granules by condensation with intrinsically-disordered proteins. *Elife* **9**, doi:10.7554/eLife.52896 (2020).

174 Matheny, T., Rao, B. S. & Parker, R. Transcriptome-Wide Comparison of Stress Granules and P-Bodies Reveals that Translation Plays a Major Role in RNA Partitioning. *Mol Cell Biol* **39**, doi:10.1128/MCB.00313-19 (2019).

175 Hubstenberger, A. *et al.* P-Body Purification Reveals the Condensation of Repressed mRNA Regulons. *Mol Cell* **68**, 144-157.e145, doi:10.1016/j.molcel.2017.09.003 (2017).

176 Jain, S. *et al.* ATPase-Modulated Stress Granules Contain a Diverse Proteome and Substructure. *Cell* **164**, 487-498, doi:10.1016/j.cell.2015.12.038 (2016).

177 Zagrovic, B., Bartonek, L. & Polyansky, A. A. RNA-protein interactions in an unstructured context. *FEBS Lett* **592**, 2901-2916, doi:10.1002/1873-3468.13116 (2018).

178 Hentze, M. W., Castello, A., Schwarzl, T. & Preiss, T. A brave new world of RNA-binding proteins. *Nat Rev Mol Cell Biol* **19**, 327-341, doi:10.1038/nrm.2017.130 (2018).

179 Jeske, M. *et al.* The Crystal Structure of the Drosophila Germline Inducer Oskar Identifies Two Domains with Distinct Vasa Helicase- and RNA-Binding Activities. *Cell Rep* **12**, 587-598, doi:10.1016/j.celrep.2015.06.055 (2015).

180 Yang, N. *et al.* Structure of Drosophila Oskar reveals a novel RNA binding protein. *Proc Natl Acad Sci U S A* **112**, 11541-11546, doi:10.1073/pnas.1515568112 (2015).

181 Trcek, T. & Lehmann, R. Germ granules in Drosophila. *Traffic* **20**, 650-660, doi:10.1111/tra.12674 (2019).

182 Itzhak, D. N., Tyanova, S., Cox, J. & Borner, G. H. Global, quantitative and dynamic mapping of protein subcellular localization. *Elife* **5**, doi:10.7554/eLife.16950 (2016).

183 Ries, R. J. *et al.* m. *Nature* **571**, 424-428, doi:10.1038/s41586-019-1374-1 (2019).

184 Fu, Y. & Zhuang, X. m. *Nat Chem Biol* **16**, 955-963, doi:10.1038/s41589-020-0524-y (2020).

185 Perry, R. P. & Kelley, D. E. Methylated constituents of heterogeneous nuclear RNA: presence in blocked 5' terminal structures. *Cell* **6**, 13-19, doi:10.1016/0092-8674(75)90068-9 (1975).

186 Desrosiers, R., Friderici, K. & Rottman, F. Identification of methylated nucleosides in messenger RNA from Novikoff hepatoma cells. *Proc Natl Acad Sci U S A* **71**, 3971-3975, doi:10.1073/pnas.71.10.3971 (1974).

187 Xiang, Y. *et al.* Corrigendum: RNA m. *Nature* **552**, 430, doi:10.1038/nature24007 (2017).

188 Khong, A., Matheny, T., Huynh, T. N., Babl, V. & Parker, R. Limited effects of m. *Nat Commun* **13**, 3735, doi:10.1038/s41467-022-31358-5 (2022).

189 Van Treeck, B. *et al.* RNA self-assembly contributes to stress granule formation and defining the stress granule transcriptome. *Proc Natl Acad Sci U S A* **115**, 2734-2739, doi:10.1073/pnas.1800038115 (2018).

190 Aumiller, W. M., Pir Cakmak, F., Davis, B. W. & Keating, C. D. RNA-Based Coacervates as a Model for Membraneless Organelles: Formation, Properties, and Interfacial Liposome Assembly. *Langmuir* **32**, 10042-10053, doi:10.1021/acs.langmuir.6b02499 (2016).

191 Lee, S. *et al.* Noncoding RNA NORAD Regulates Genomic Stability by Sequestering PUMILIO Proteins. *Cell* **164**, 69-80, doi:10.1016/j.cell.2015.12.017 (2016).

192 Tauber, D. *et al.* Modulation of RNA Condensation by the DEAD-Box Protein eIF4A. *Cell* **180**, 411-426.e416, doi:10.1016/j.cell.2019.12.031 (2020).

193 Langdon, E. M. *et al.* mRNA structure determines specificity of a polyQ-driven phase separation. *Science* **360**, 922-927, doi:10.1126/science.aar7432 (2018).

194 Jambor, H., Brunel, C. & Ephrussi, A. Dimerization of oskar 3' UTRs promotes hitchhiking for RNA localization in the Drosophila oocyte. *RNA* **17**, 2049-2057, doi:10.1261/rna.2686411 (2011).

195 Ferrandon, D., Koch, I., Westhof, E. & Nüsslein-Volhard, C. RNA-RNA interaction is required for the formation of specific bicoid mRNA 3' UTR-STAUFEN ribonucleoprotein particles. *EMBO J* **16**, 1751-1758, doi:10.1093/emboj/16.7.1751 (1997).

196 Vourekas, A., Alexiou, P., Vrettos, N., Maragkakis, M. & Mourelatos, Z. Sequence-dependent but not sequence-specific piRNA adhesion traps mRNAs to the germ plasm. *Nature* **531**, 390-394, doi:10.1038/nature17150 (2016).

197 Banani, S. F. *et al.* Compositional Control of Phase-Separated Cellular Bodies. *Cell* **166**, 651-663, doi:10.1016/j.cell.2016.06.010 (2016).

198 Pitchiaya, S. *et al.* Dynamic Recruitment of Single RNAs to Processing Bodies Depends on RNA Functionality. *Mol Cell* **74**, 521-533.e526, doi:10.1016/j.molcel.2019.03.001 (2019).

199 Kedersha, N. *et al.* Stress granules and processing bodies are dynamically linked sites of mRNP remodeling. *J Cell Biol* **169**, 871-884, doi:10.1083/jcb.200502088 (2005).

200 Simpson, C. E., Lui, J., Kershaw, C. J., Sims, P. F. & Ashe, M. P. mRNA localization to P-bodies in yeast is bi-phasic with many mRNAs captured in a late Bfr1p-dependent wave. *J Cell Sci* **127**, 1254-1262, doi:10.1242/jcs.139055 (2014).

201 Aizer, A. *et al.* Quantifying mRNA targeting to P-bodies in living human cells reveals their dual role in mRNA decay and storage. *J Cell Sci* **127**, 4443-4456, doi:10.1242/jcs.152975 (2014).

202 Bhattacharyya, S. N., Habermacher, R., Martine, U., Closs, E. I. & Filipowicz, W. Stress-induced reversal of microRNA repression and mRNA P-body localization in human cells. *Cold Spring Harb Symp Quant Biol* **71**, 513-521, doi:10.1101/sqb.2006.71.038 (2006).

203 Brengues, M., Teixeira, D. & Parker, R. Movement of eukaryotic mRNAs between polysomes and cytoplasmic processing bodies. *Science* **310**, 486-489, doi:10.1126/science.1115791 (2005).

204 Laver, J. D. *et al.* The RNA-Binding Protein Rasputin/G3BP Enhances the Stability and Translation of Its Target mRNAs. *Cell Rep* **30**, 3353-3367.e3357, doi:10.1016/j.celrep.2020.02.066 (2020).

205 An, H., Tan, J. T. & Shelkovnikova, T. A. Stress granules regulate stress-induced paraspeckle assembly. *J Cell Biol* **218**, 4127-4140, doi:10.1083/jcb.201904098 (2019).

206 Liao, Y. C. *et al.* RNA Granules Hitchhike on Lysosomes for Long-Distance Transport, Using Annexin A11 as a Molecular Tether. *Cell* **179**, 147-164.e120, doi:10.1016/j.cell.2019.08.050 (2019).

207 Panas, M. D., Ivanov, P. & Anderson, P. Mechanistic insights into mammalian stress granule dynamics. *J Cell Biol* **215**, 313-323, doi:10.1083/jcb.201609081 (2016).

208 Anderson, P., Kedersha, N. & Ivanov, P. Stress granules, P-bodies and cancer. *Biochim Biophys Acta* **1849**, 861-870, doi:10.1016/j.bbagrm.2014.11.009 (2015).

209 Kedersha, N., Ivanov, P. & Anderson, P. Stress granules and cell signaling: more than just a passing phase? *Trends Biochem Sci* **38**, 494-506, doi:10.1016/j.tibs.2013.07.004 (2013).

210 Reineke, L. C. & Lloyd, R. E. Diversion of stress granules and P-bodies during viral infection. *Virology* **436**, 255-267, doi:10.1016/j.virol.2012.11.017 (2013).

211 Somasekharan, S. P. *et al.* YB-1 regulates stress granule formation and tumor progression by translationally activating G3BP1. *J Cell Biol* **208**, 913-929, doi:10.1083/jcb.201411047 (2015).

212 Niewidok, B. *et al.* Single-molecule imaging reveals dynamic biphasic partition of RNA-binding proteins in stress granules. *J Cell Biol* **217**, 1303-1318, doi:10.1083/jcb.201709007 (2018).

213 Wheeler, J. R., Matheny, T., Jain, S., Abrisch, R. & Parker, R. Distinct stages in stress granule assembly and disassembly. *Elife* **5**, doi:10.7554/eLife.18413 (2016).

214 Wheeler, J. R., Jain, S., Khong, A. & Parker, R. Isolation of yeast and mammalian stress granule cores. *Methods* **126**, 12-17, doi:10.1016/j.ymeth.2017.04.020 (2017).

215 Khong, A., Jain, S., Matheny, T., Wheeler, J. R. & Parker, R. Isolation of mammalian stress granule cores for RNA-Seq analysis. *Methods* **137**, 49-54, doi:10.1016/j.ymeth.2017.11.012 (2018).

216 Youn, J. Y. *et al.* High-Density Proximity Mapping Reveals the Subcellular Organization of mRNA-Associated Granules and Bodies. *Mol Cell* **69**, 517-532.e511, doi:10.1016/j.molcel.2017.12.020 (2018).

217 Markmiller, S. *et al.* Context-Dependent and Disease-Specific Diversity in Protein Interactions within Stress Granules. *Cell* **172**, 590-604.e513, doi:10.1016/j.cell.2017.12.032 (2018).

218 Tichon, A. *et al.* A conserved abundant cytoplasmic long noncoding RNA modulates repression by Pumilio proteins in human cells. *Nat Commun* **7**, 12209, doi:10.1038/ncomms12209 (2016).

219 Tichon, A., Perry, R. B., Stojic, L. & Ulitsky, I. SAM68 is required for regulation of Pumilio by the NORAD long noncoding RNA. *Genes Dev* **32**, 70-78, doi:10.1101/gad.309138.117 (2018).

220 Tourrière, H. *et al.* The RasGAP-associated endoribonuclease G3BP assembles stress granules. *J Cell Biol* **160**, 823-831, doi:10.1083/jcb.200212128 (2003).

221 Kedersha, N. *et al.* G3BP-Caprin1-USP10 complexes mediate stress granule condensation and associate with 40S subunits. *J Cell Biol* **212**, 845-860, doi:10.1083/jcb.201508028 (2016).

222 Baron-Benhamou, J., Gehring, N. H., Kulozik, A. E. & Hentze, M. W. Using the lambdaN peptide to tether proteins to RNAs. *Methods Mol Biol* **257**, 135-154, doi:10.1385/1-59259-750-5:135 (2004).

223 Van Nostrand, E. L. *et al.* A large-scale binding and functional map of human RNA-binding proteins. *Nature* **583**, 711-719, doi:10.1038/s41586-020-2077-3 (2020).

224 Yang, Y. C. *et al.* CLIPdb: a CLIP-seq database for protein-RNA interactions. *BMC Genomics* **16**, 51, doi:10.1186/s12864-015-1273-2 (2015).

225 Subtelny, A. O., Eichhorn, S. W., Chen, G. R., Sive, H. & Bartel, D. P. Poly(A)-tail profiling reveals an embryonic switch in translational control. *Nature* **508**, 66-71, doi:10.1038/nature13007 (2014).

226 Lima, S. A. *et al.* Short poly(A) tails are a conserved feature of highly expressed genes. *Nat Struct Mol Biol* **24**, 1057-1063, doi:10.1038/nsmb.3499 (2017).

227 Dewey, C. M. *et al.* TDP-43 is directed to stress granules by sorbitol, a novel physiological osmotic and oxidative stressor. *Mol Cell Biol* **31**, 1098-1108, doi:10.1128/MCB.01279-10 (2011).

228 Gilks, N. *et al.* Stress granule assembly is mediated by prion-like aggregation of TIA-1. *Mol Biol Cell* **15**, 5383-5398, doi:10.1091/mbc.e04-08-0715 (2004).

229 Buchan, J. R. & Parker, R. Eukaryotic stress granules: the ins and outs of translation. *Mol Cell* **36**, 932-941, doi:10.1016/j.molcel.2009.11.020 (2009).

230 Guillén-Boixet, J. *et al.* RNA-Induced Conformational Switching and Clustering of G3BP Drive Stress Granule Assembly by Condensation. *Cell* **181**, 346-361.e317, doi:10.1016/j.cell.2020.03.049 (2020).

231 Sanders, D. W. *et al.* Competing Protein-RNA Interaction Networks Control Multiphase Intracellular Organization. *Cell* **181**, 306-324.e328, doi:10.1016/j.cell.2020.03.050 (2020).

232 Yang, P. *et al.* G3BP1 Is a Tunable Switch that Triggers Phase Separation to Assemble Stress Granules. *Cell* **181**, 325-345.e328, doi:10.1016/j.cell.2020.03.046 (2020).

233 Nihongaki, Y., Yamamoto, S., Kawano, F., Suzuki, H. & Sato, M. CRISPR-Cas9-based photoactivatable transcription system. *Chem Biol* **22**, 169-174, doi:10.1016/j.chembiol.2014.12.011 (2015).

234 Martin, R. M., Rino, J., Carvalho, C., Kirchhausen, T. & Carmo-Fonseca, M. Live-cell visualization of pre-mRNA splicing with single-molecule sensitivity. *Cell Rep* **4**, 1144-1155, doi:10.1016/j.celrep.2013.08.013 (2013).

235 Ascano, M. *et al.* FMRP targets distinct mRNA sequence elements to regulate protein expression. *Nature* **492**, 382-386, doi:10.1038/nature11737 (2012).

236 Dunagin, M., Cabili, M. N., Rinn, J. & Raj, A. Visualization of lncRNA by single-molecule fluorescence in situ hybridization. *Methods Mol Biol* **1262**, 3-19, doi:10.1007/978-1-4939-2253-6_1 (2015).

237 Gaspar, I., Wippich, F. & Ephrussi, A. Enzymatic production of single-molecule FISH and RNA capture probes. *RNA* **23**, 1582-1591, doi:10.1261/rna.061184.117 (2017).

238 Schindelin, J. *et al.* Fiji: an open-source platform for biological-image analysis. *Nat Methods* **9**, 676-682, doi:10.1038/nmeth.2019 (2012).

239 Trapnell, C. *et al.* Differential analysis of gene regulation at transcript resolution with RNA-seq. *Nat Biotechnol* **31**, 46-53, doi:10.1038/nbt.2450 (2013).

240 Körner, C. G. *et al.* The deadenylating nuclease (DAN) is involved in poly(A) tail removal during the meiotic maturation of Xenopus oocytes. *EMBO J* **17**, 5427-5437, doi:10.1093/emboj/17.18.5427 (1998).

241 Katoh, T., Hojo, H. & Suzuki, T. Destabilization of microRNAs in human cells by 3' deadenylation mediated by PARN and CUGBP1. *Nucleic Acids Res* **43**, 7521-7534, doi:10.1093/nar/gkv669 (2015).

242 Agarwal, V., Bell, G. W., Nam, J. W. & Bartel, D. P. Predicting effective microRNA target sites in mammalian mRNAs. *Elife* **4**, doi:10.7554/eLife.05005 (2015).

243 Liu, J., Zhang, C., Zhao, Y. & Feng, Z. MicroRNA Control of p53. *J Cell Biochem* **118**, 7-14, doi:10.1002/jcb.25609 (2017).

244 Swarbrick, A. *et al.* miR-380-5p represses p53 to control cellular survival and is associated with poor outcome in MYCN-amplified neuroblastoma. *Nat Med* **16**, 1134-1140, doi:10.1038/nm.2227 (2010).

245 Vlachos, I. S. *et al.* DIANA-miRPath v3.0: deciphering microRNA function with experimental support. *Nucleic Acids Res* **43**, W460-466, doi:10.1093/nar/gkv403 (2015).

246 Burns, D. M., D'Ambrogio, A., Nottrott, S. & Richter, J. D. CPEB and two poly(A) polymerases control miR-122 stability and p53 mRNA translation. *Nature* **473**, 105-108, doi:10.1038/nature09908 (2011).

247 Rivlin, N., Brosh, R., Oren, M. & Rotter, V. Mutations in the p53 Tumor Suppressor Gene: Important Milestones at the Various Steps of Tumorigenesis. *Genes Cancer* **2**, 466-474, doi:10.1177/1947601911408889 (2011).

248 Bieging, K. T., Mello, S. S. & Attardi, L. D. Unravelling mechanisms of p53-mediated tumour suppression. *Nat Rev Cancer* **14**, 359-370, doi:10.1038/nrc3711 (2014).

249 Joerger, A. C. & Fersht, A. R. The p53 Pathway: Origins, Inactivation in Cancer, and Emerging Therapeutic Approaches. *Annu Rev Biochem* **85**, 375-404, doi:10.1146/annurev-biochem-060815-014710 (2016).

250 Zhang, L. N. & Yan, Y. B. Depletion of poly(A)-specific ribonuclease (PARN) inhibits proliferation of human gastric cancer cells by blocking cell cycle progression. *Biochim Biophys Acta* **1853**, 522-534, doi:10.1016/j.bbamcr.2014.12.004 (2015).

251 Balatsos, N. A. *et al.* Competitive inhibition of human poly(A)-specific ribonuclease (PARN) by synthetic fluoro-pyranosyl nucleosides. *Biochemistry* **48**, 6044-6051, doi:10.1021/bi900236k (2009).

252 Balatsos, N. A., Anastasakis, D. & Stathopoulos, C. Inhibition of human poly(A)-specific ribonuclease (PARN) by purine nucleotides: kinetic analysis. *J Enzyme Inhib Med Chem* **24**, 516-523, doi:10.1080/14756360802218763 (2009).

253 Balatsos, N. *et al.* Kinetic and in silico analysis of the slow-binding inhibition of human poly(A)-specific ribonuclease (PARN) by novel nucleoside analogues. *Biochimie* **94**, 214-221, doi:10.1016/j.biochi.2011.10.011 (2012).

254 Ren, Y. G., Martínez, J., Kirsebom, L. A. & Virtanen, A. Inhibition of Klenow DNA polymerase and poly(A)-specific ribonuclease by aminoglycosides. *RNA* **8**, 1393-1400, doi:10.1017/s1355838202021015 (2002).

255 Jadhav, G. P. *et al.* Discovery, synthesis and biochemical profiling of purine-2,6-dione derivatives as inhibitors of the human poly(A)-selective ribonuclease Caf1. *Bioorg Med Chem Lett* **25**, 4219-4224, doi:10.1016/j.bmcl.2015.07.095 (2015).

256 Maryati, M. *et al.* A fluorescence-based assay suitable for quantitative analysis of deadenylase enzyme activity. *Nucleic Acids Res* **42**, e30, doi:10.1093/nar/gkt972 (2014).

257 Ren, Y. G., Kirsebom, L. A. & Virtanen, A. Coordination of divalent metal ions in the active site of poly(A)-specific ribonuclease. *J Biol Chem* **279**, 48702-48706, doi:10.1074/jbc.M403858200 (2004).

258 Qin, X. *et al.* The Bcr-Abl inhibitor GNF-7 inhibits necroptosis and ameliorates acute kidney injury by targeting RIPK1 and RIPK3 kinases. *Biochem Pharmacol* **177**, 113947, doi:10.1016/j.bcp.2020.113947 (2020).

259 Liang, X. *et al.* Discovery of 2-((3-Amino-4-methylphenyl)amino)-N-(2-methyl-5-(3-(trifluoromethyl)benzamido)phenyl)-4-(methylamino)pyrimidine-5-carboxamide (CHMFL-ABL-053) as a Potent, Selective, and Orally Available BCR-

ABL/SRC/p38 Kinase Inhibitor for Chronic Myeloid Leukemia. *J Med Chem* **59**, 1984-2004, doi:10.1021/acs.jmedchem.5b01618 (2016).

260 Nonami, A. *et al.* Identification of novel therapeutic targets in acute leukemias with NRAS mutations using a pharmacologic approach. *Blood* **125**, 3133-3143, doi:10.1182/blood-2014-12-615906 (2015).

261 Friesner, R. A. *et al.* Glide: a new approach for rapid, accurate docking and scoring. 1. Method and assessment of docking accuracy. *J Med Chem* **47**, 1739-1749, doi:10.1021/jm0306430 (2004).

262 Friesner, R. A. *et al.* Extra precision glide: docking and scoring incorporating a model of hydrophobic enclosure for protein-ligand complexes. *J Med Chem* **49**, 6177-6196, doi:10.1021/jm051256o (2006).

263 Halgren, T. A. Identifying and characterizing binding sites and assessing druggability. *J Chem Inf Model* **49**, 377-389, doi:10.1021/ci800324m (2009).

264 Beckstein, O., Fourrier, A. & Iorga, B. I. Prediction of hydration free energies for the SAMPL4 diverse set of compounds using molecular dynamics simulations with the OPLS-AA force field. *J Comput Aided Mol Des* **28**, 265-276, doi:10.1007/s10822-014-9727-1 (2014).

265 Xi, L. & Cech, T. R. Inventory of telomerase components in human cells reveals multiple subpopulations of hTR and hTERT. *Nucleic Acids Res* **42**, 8565-8577, doi:10.1093/nar/gku560 (2014).

266 Jafri, M. A., Ansari, S. A., Alqahtani, M. H. & Shay, J. W. Roles of telomeres and telomerase in cancer, and advances in telomerase-targeted therapies. *Genome Med* **8**, 69, doi:10.1186/s13073-016-0324-x (2016).

APPENDIX

Supporting tables and figures

Table A.1. Table of all luciferase-NORAD chimera constructs.

This table lists all constructs used in the NORAD experiments with length, SG enrichment, and predicted protein binding sites (assuming luciferase has 2 protein binding sites).

Construct	Length (bp)	%SG accumulation	Predicted number of protein binding sites
FL NORAD	5287	70.9	51
NORAD-PREmut	5287	50	33 (assuming SAM68 sites not affected)
1/2 NORAD	2644	61.8	24
2/2 NORAD	2643	58.9	29
1/4 NORAD	1322	42.6	9
2/4 NORAD	1322	56	17
3/4 NORAD	1322	50	22
4/4 NORAD	1321	33.2	9
1/8 NORAD	661	20.9	2
2/8 NORAD	661	38.2	9
3/8 NORAD	661	35.8	7
4/8 NORAD	661	57.5	12
5/8 NORAD	661	41.3	15
6/8 NORAD	661	31.8	8
7/8 NORAD	661	34.8	6
8/8 NORAD	660	45.6	5
2/2 asNORAD	2643	25	8
1/4 asNORAD	1322	20.7	4
2/4 asNORAD	1322	26.2	5
3/4 asNORAD	1322	45.4	3
4/4 asNORAD	1321	56.25	7
1/8 asNORAD	661	20	2
2/8 asNORAD	661	27.45	4
3/8 asNORAD	661	33.3	4
4/8 asNORAD	661	21.2	3
5/8 asNORAD	661	29.8	3
6/8 asNORAD	661	30.4	2
7/8 asNORAD	661	21.1	4
8/8 asNORAD	660	32	5
660bp Luc	660	20.2	3
1300 bp Luc	1300	24.2	4
FL Luc	1635	21.1	4
2xLuc	3340	23.25	6
3xLuc	5045	30.5	8

*Assuming Luciferase has 2 protein binding sites

Table A.2. Plasmids and Oligos.

This table describes all plasmids used in this study, including their construction. Oligos used for plasmid construction are also listed.

Plasmid Number	Description	Construction Notes
pRP2854	CRISPR/Cas9 plasmid for targeting to AAVS locus	Gift from Dan Youmans in Tom Cech lab
pRP2855	AAVS TDP43	Gift from Josh Wheeler in Parker Lab
pRP2856	AAVS Luciferase	PCR off of Addgene 64127 with oBVT164 and oBVT165. Cut pRP2855 with NotI and BglII. In Fusion.
pRP2871	Tet-Luciferase 7 BoxB	PCR off of Addgene 60817 with oBVT255 and oBVT256. Amplify Addgene 64127 with oBVT123 and oBVT179. PCR off insert gave smear. In Fusion cloning. Isolate colony that had 7 inserts.
pRP2873	AAVS Luciferase 7 BoxB	PCR off pRP2871 with oBVT174 and oBVT259. Cup pRP2855 with NotI and BglII. Gibson assembly.
pRP2874	AAVS Luciferase 25 BoxB	PCR off pRP2856 with oBVT316 and oBVT317. Cut Addgene 60817 with SacI and SmaI. Gibson assembly.
pRP2940	G3BP-GFP-LN	Gift from Richard Lloyd lab.
pRP2941	GFP-LN	Gift from Richard Lloyd lab.
pRP2944	FMRP-GFP-LN	PCR amplify Addgene 48690 with oBVT297 and oBVT298. Cut pRP2940 with EcoRI and BamHI. Gibson assembly.
pRP2877	Tet-Luciferase with FL NORAD in 3'UTR	PCR off Addgene 64127 with oBVT122 anbd 123 for Vector. PCR off cDNA NORAD with oBVT231 and oBVT232 for insert. Gibson cloning
pRP2878	Tet-Luciferase with 5' half of NORAD in 3'UTR	PCR off Addgene 64127 with oBVT122 anbd 123 for Vector. PCR off cDNA NORAD with oBVT231 and oBVT234 for insert. Gibson cloning
pRP2879	Tet-Luciferase with 3' half of NORAD in 3'UTR	PCR off Addgene 64127 with oBVT122 and 123 for Vector. PCR off cDNA NORAD with oBVT233 and oBVT232. Gibson cloning.
pRP2880	Tet-Luciferase with 1/4 NORAD in 3'UTR	PCR off Addgene 64127 with oBVT122 and 123 for Vector. PCR off cDNA NORAD with oBVT231 and oBVT273. Gibson cloning.
pRP2881	Tet-Luciferase with 2/4 NORAD in 3'UTR	PCR off Addgene 64127 with oBVT122 and 123 for Vector. PCR off cDNA NORAD with oBVT275 and oBVT234. Gibson cloning.
pRP2882	Tet-Luciferase with 3/4 NORAD in 3'UTR	PCR off Addgene 64127 with oBVT122 and 123 for Vector. PCR off cDNA NORAD with oBVT233 and oBVT277. Gibson cloning.
pRP2883	Tet-Luciferase with 4/4 NORAD in 3'UTR	PCR off Addgene 64127 with oBVT122 and 123 for Vector. PCR off cDNA NORAD with oBVT279 and oBVT232. Gibson cloning.
pRP2884	Tet-Luciferase with 1/8 NORAD in 3'UTR	PCR off Addgene 64127 with oBVT122 and 123 for Vector. PCR off cDNA NORAD with oBVT231 and oBVT281. Gibson cloning.
pRP2885	Tet-Luciferase with 2/8 NORAD in 3'UTR	PCR off Addgene 64127 with oBVT122 and 123 for Vector. PCR off cDNA NORAD with oBVT283 and oBVT273. Gibson cloning.
pRP2886	Tet-Luciferase with 3/8 NORAD in 3'UTR	PCR off Addgene 64127 with oBVT122 and 123 for Vector. PCR off cDNA NORAD with oBVT275 and oBVT285. Gibson cloning.
pRP2887	Tet-Luciferase with 4/8 NORAD in 3'UTR	PCR off Addgene 64127 with oBVT122 and 123 for Vector. PCR off cDNA NORAD with oBVT287 and oBVT234. Gibson cloning.
pRP2888	Tet-luciferase with 5/8 NORAD in 3'UTR	PCR off Addgene 64127 with oBVT122 and 123 for Vector. PCR off cDNA NORAD with oBVT233 and oBVT289. Gibson cloning.
pRP2889	Tet-luciferase with 6/8 NORAD in 3'UTR	PCR off Addgene 64127 with oBVT122 and 123 for Vector. PCR off cDNA NORAD with oBVT291 and oBVT277. Gibson cloning.
pRP2890	Tet-Luciferase with 7/8 NORAD in 3'UTR	PCR off Addgene 64127 with oBVT122 and 123 for Vector. PCR off cDNA NORAD with oBVT279 and oBVT293. Gibson cloning.
pRP2891	Tet-Luciferase with 8/8 NORAD in 3'UTR	PCR off Addgene 64127 with oBVT122 and 123 for Vector. PCR off cDNA NORAD with oBVT295 and oBVT232. Gibson cloning.
pRP2909	Tet-Luciferase with AS 2/2 of NORAD in 3'UTR	PCR off Addgene 64127 with oBVT122 and 123 for Vector. PCR off cDNA NORAD with oBVT254 and oBVT251. Gibson cloning.

pRP2910	Tet-Luciferase with AS 1/4 NORAD in 3'UTR	PCR off Addgene 64127 with oBVT122 and 123 for Vector. PCR off cDNA NORAD with oBVT252 and oBVT274. Gibson cloning.
pRP2911	Tet-Luciferase with AS 2/4 NORAD in 3'UTR	PCR off Addgene 64127 with oBVT122 and 123 for Vector. PCR off cDNA NORAD with oBVT276 and oBVT253. Gibson cloning.
pRP2912	Tet-Luciferase with AS 3/4 NORAD in 3'UTR	PCR off Addgene 64127 with oBVT122 and 123 for Vector. PCR off cDNA NORAD with oBVT254 and oBVT278. Gibson cloning.
pRP2913	Tet-Luciferase with AS 4/4 NORAD in 3'UTR	PCR off Addgene 64127 with oBVT122 and 123 for Vector. PCR off cDNA NORAD with oBVT280 and oBVT251. Gibson cloning.
pRP2914	Tet-Luciferase with AS 1/8 NORAD in 3'UTR	PCR off Addgene 64127 with oBVT122 and 123 for Vector. PCR off cDNA NORAD with oBVT252 and oBVT282. Gibson cloning.
pRP2915	Tet-Luciferase with AS 2/8 NORAD in 3'UTR	PCR off Addgene 64127 with oBVT122 and 123 for Vector. PCR off cDNA NORAD with oBVT284 and oBVT274. Gibson cloning.
pRP2916	Tet-Luciferase with AS 3/8 NORAD in 3'UTR	PCR off Addgene 64127 with oBVT122 and 123 for Vector. PCR off cDNA NORAD with oBVT276 and oBVT286. Gibson cloning.
pRP2917	Tet-Luciferase with AS 4/8 NORAD in 3'UTR	PCR off Addgene 64127 with oBVT122 and 123 for Vector. PCR off cDNA NORAD with oBVT288 and oBVT253. Gibson cloning.
pRP2918	Tet-Luciferase with AS 5/8 NORAD in 3'UTR	PCR off Addgene 64127 with oBVT122 and 123 for Vector. PCR off cDNA NORAD with oBVT254 and oBVT290. Gibson cloning.
pRP2919	Tet-Luciferase with AS 6/8 NORAD in 3'UTR	PCR off Addgene 64127 with oBVT122 and 123 for Vector. PCR off cDNA NORAD with oBVT292 and oBVT278. Gibson cloning.
pRP2920	Tet-Luciferase with AS 7/8 NORAD in 3'UTR	PCR off Addgene 64127 with oBVT122 and 123 for Vector. PCR off cDNA NORAD with oBVT280 and oBVT294. Gibson cloning.
pRP2921	Tet-Luciferase with AS 8/8 NORAD in 3'UTR	PCR off Addgene 64127 with oBVT122 and 123 for Vector. PCR off cDNA NORAD with oBVT279 and oBVT251. Gibson cloning.
	Tet-Luciferase with NORAD-PREmut in 3'UTR	PCR off Addgene 64127 with oBVT122 anbd 123 for Vector. PCR off cDNA NORAD-PREmut from Josh Mendel's lab with oBVT231 and oBVT232 for insert. Gibson cloning
pRP2892	AAVS with FL NORAD in 3'UTR of luc	PCR off pRP2877 with oBVT164 and 248 for insert. Cut pRP2855 with NotI and BglII. In Fusion/Gibson to clone sections together.
pRP2893	AAVS with 5' half of NORAD in 3'UTR	PCR off pRP2878 with oBVT164 and 258 for insert. Cut pRP2855 with NotI and BglII. In Fusion/Gibson to clone sections together.
pRP2894	AAVS with 3'half of NORAD in 3'UTR	PCR off pRP2879 with oBVT164 and 249 for insert. Cut pRP2855 with NotI and BglII. In Fusion/Gibson to clone sections together.
pRP2895	AAVS with 1/4 NORAD in 3'UTR	PCR off pRP2880 with oBVT164 and 300 for insert. Cut pRP2855 with NotI and BglII. In Fusion/Gibson to clone sections together.
pRP2896	AAVS with 2/4 NORAD in 3'UTR	PCR off pRP2881 with oBVT164 and 249 for insert. Cut pRP2855 with NotI and BglII. In Fusion/Gibson to clone sections together.
pRP2897	AAVS with 3/4 NORAD in 3'UTR	PCR off pRP2882 with oBVT164 and 303 for insert. Cut pRP2855 with NotI and BglII. In Fusion/Gibson to clone sections together.
pRP2898	AAVS with 4/4 NORAD in 3'UTR	PCR off pRP2883 with oBVT164 and 248 for insert. Cut pRP2855 with NotI and BglII. In Fusion/Gibson to clone sections together.
pRP2899	AAVS with 1/8 NORAD in 3'UTR	PCR off pRP2884 with oBVT164 and 299 for insert. Cut pRP2855 with NotI and BglII. In Fusion/Gibson to clone sections together.
pRP2900	AAVS with 2/8 NORAD in 3'UTR	PCR off pRP2885 with oBVT164 and 300 for insert. Cut pRP2855 with NotI and BglII. In Fusion/Gibson to clone sections together.
pRP2901	AAVS with 3/8 NORAD in 3'UTR	PCR off pRP2886 with oBVT164 and 301 for insert. Cut pRP2855 with NotI and BglII. In Fusion/Gibson to clone sections together.
pRP2902	AAVS with 4/8 NORAD in 3'UTR	PCR off pRP2887 with oBVT164 and 249 for insert. Cut pRP2855 with NotI and BglII. In Fusion/Gibson to clone sections together.
pRP2903	AAVS with 5/8 NORAD in 3'UTR	PCR off pRP2888 with oBVT164 and 302 for insert. Cut pRP2855 with NotI and BglII. In Fusion/Gibson to clone sections together.
pRP2904	AAVS with 6/8 NORAD in 3'UTR	PCR off pRP2889 with oBVT164 and 303 for insert. Cut pRP2855 with NotI and BglII. In Fusion/Gibson to clone sections together.
pRP2905	AAVS with 7/8 NORAD in 3'UTR	PCR off pRP2890 with oBVT164 and 304 for insert. Cut pRP2855 with NotI and BglII. In Fusion/Gibson to clone sections together.
pRP2906	AAVS with 8/8 NORAD in 3'UTR	PCR off pRP2891 with oBVT164 and 248 for insert. Cut pRP2855 with NotI and BglII. In Fusion/Gibson to clone sections together.
pRP2924	AAVS with AS 2/2 of NORAD in 3'UTR	PCR off pRP2909 with oBVT164 and 258 for insert. Cut pRP2855 with NotI and BglII. In Fusion/Gibson to clone sections together.
pRP2925	AAVS with AS 1/4 NORAD in 3'UTR	PCR off pRP2910 with oBVT164 and 257 for insert. Cut pRP2855 with NotI and BglII. In Fusion/Gibson to clone sections together.

pRP2926	AAVS with AS 2/4 NORAD in 3'UTR	PCR off pRP2911 with oBVT164 and 306 for insert. Cut pRP2855 with NotI and BglII. In Fusion/Gibson to clone sections together.
pRP2927	AAVS with AS 3/4 NORAD in 3'UTR	PCR off pRP2912 with oBVT164 and 258 for insert. Cut pRP2855 with NotI and BglII. In Fusion/Gibson to clone sections together.
pRP2928	AAVS with AS 4/4 NORAD in 3'UTR	PCR off pRP2913 with oBVT164 and 309 for insert. Cut pRP2855 with NotI and BglII. In Fusion/Gibson to clone sections together.
pRP2929	AAVS with AS 1/8 NORAD in 3'UTR	PCR off pRP2914 with oBVT164 and 257 for insert. Cut pRP2855 with NotI and BglII. In Fusion/Gibson to clone sections together.
pRP2930	AAVS with AS 2/8 NORAD in 3'UTR	PCR off pRP2915 with oBVT164 and 305 for insert. Cut pRP2855 with NotI and BglII. In Fusion/Gibson to clone sections together.
pRP2931	AAVS with AS 3/8 NORAD in 3'UTR	PCR off pRP2916 with oBVT164 and 306 for insert. Cut pRP2855 with NotI and BglII. In Fusion/Gibson to clone sections together.
pRP2932	AAVS with AS 4/8 NORAD in 3'UTR	PCR off pRP2917 with oBVT164 and 307 for insert. Cut pRP2855 with NotI and BglII. In Fusion/Gibson to clone sections together.
pRP2933	AAVS with AS 5/8 NORAD in 3'UTR	PCR off pRP2918 with oBVT164 and 258 for insert. Cut pRP2855 with NotI and BglII. In Fusion/Gibson to clone sections together.
pRP2934	AAVS with AS 6/8 NORAD in 3'UTR	PCR off pRP2919 with oBVT164 and 308 for insert. Cut pRP2855 with NotI and BglII. In Fusion/Gibson to clone sections together.
pRP2935	AAVS with AS 7/8 NORAD in 3'UTR	PCR off pRP2920 with oBVT164 and 309 for insert. Cut pRP2855 with NotI and BglII. In Fusion/Gibson to clone sections together.
pRP2936	AAVS with AS 8/8 NORAD in 3'UTR	PCR off pRP2921 with oBVT164 and 310 for insert. Cut pRP2855 with NotI and BglII. In Fusion/Gibson to clone sections together.
pRP2937	AAVS with FL luciferase in 3'UTR of luciferase	PCR off pRP2856 with oBVT311 and oBVT312. Cut pRP2856 with Not1. Gibson assembly
pRP2938	AAVS with 1300nt luciferase in 3'UTR of luciferase	PCR off pRP2856 with oBVT311 and oBVT313. Cut pRP2856 with Not1. Gibson assembly
pRP2939	AAVS with 660nt luciferase in 3'UTR of luciferase	PCR off pRP2856 with oBVT311 and oBVT314. Cut pRP2856 with Not1. Gibson assembly
	AAVS with 3xluciferase in 3'UTR of luciferase	PCR off pRP2837 with oBVT311 and oBVT312. Extract the right-size band. Cut pRP2856 with Not1. Gibson assembly
	AAVS with 2xluciferase in 3'UTR of luciferase	PCR off with oBVT311 and oBVT312. Extract the right-size band. Cut pRP2856 with Not1. Gibson assembly
	AAVS with FL NORAD in 3'UTR of luc	PCR off with oBVT164 and 248 for insert. Cut pRP2855 with NotI and BglII. In Fusion/Gibson to clone sections together.
Addgene 64127	Tet-inducible luciferase reporter	
Addgene 60817	pCMV5-25BoxB	
Addgene 48690	pFRT-TODestFLAGHAhFMRPiso1	

Oligo	Sequence
oBVT123	ATAAGATCTTTACTTCTTGGC
oBVT164	GAGAATTGGCTAGCAGATCTGGTACCGAATTCGCCACCAT
oBVT165	GATCCCTCGAGGAGCGGCCGCCTGCTTTAATAAGATCTTTACTTCTTGGC
oBVT174	TAGTTGTGGGGGAGGAAGT
oBVT179	TAAAGCAGGCGGCCG
oBVT255	CCAAGAAGTAAAGATCTTATCGTTTAGTGAACCGTCAG
oBVT256	AATAAACAAGTTCTGCTTTAGGATCCAGATAATATCCTCG
oBVT259	GATCCCTCGAGGAGCGGCCGCCTGCTTTAGGATCCAGATAATATCC
oBVT297	GATCTCGAGCTCAAGCTTCGAATTCATGGAGGAGCTGGTGGTG
oBVT298	ATGGTGGCGACCGGCCGGTGGATCCCGGGTACTCCATTCACGAG
oBVT316	GAGGATATTATCTGGATCCCTAAAGCAGGCGGCCGCTC

oBVT317	GACGGTTCACTAAACGAGCTATAAGATCTTTACTTCTTGGCCTTAATGAGAATCTCG
oBVT122	TAAAGCAGAACTTGTTTATTGCAG
oBVT231	CCAAGAAGTAAAGATCTTATAGTTCCGGTCCGGCAGAG
oBVT232	AATAAACAAGTTCTGCTTTAGGAAATTGAAAAACACAAGCAAAGAACAAAG
oBVT233	CCAAGAAGTAAAGATCTTATTATTGTATATATAACGGACAAATTAGTCCC
oBVT234	AATAAACAAGTTCTGCTTTATATACAGTATAGCAAAGTTAAATGAAATGCATGTAACATATAC
oBVT273	AATAAACAAGTTCTGCTTTAACAATGAGTATTACTCAACAGGTGATTTG
oBVT274	CCAAGAAGTAAAGATCTTATACAATGAGTATTACTCAACAGGTGATTTG
oBVT275	CCAAGAAGTAAAGATCTTATGTTTGTGCAGTGGTTCAGGG
oBVT276	AATAAACAAGTTCTGCTTTAGTTTGTGCAGTGGTTCAGGG
oBVT277	AATAAACAAGTTCTGCTTTAAACCTACATTGTGCACTTTTTTTTTTG
oBVT278	CCAAGAAGTAAAGATCTTATAACCTACATTGTGCACTTTTTTTTTG
oBVT279	CCAAGAAGTAAAGATCTTATAACAGTAGAGGGCTTAAGTAACAC
oBVT280	AATAAACAAGTTCTGCTTTAAACAGTAGAGGGCTTAAGTAACAC
oBVT281	AATAAACAAGTTCTGCTTTAAGCAAAGTCTGGTAGAATGAAGACC
oBVT282	CCAAGAAGTAAAGATCTTATAGCAAAGTCTGGTAGAATGAAGACC
oBVT283	CCAAGAAGTAAAGATCTTATGTCGGAAGAGAGAAATGGTAGAATG
oBVT284	AATAAACAAGTTCTGCTTTAGTCGGAAGAGAGAAATGGTAGAATG
oBVT285	AATAAACAAGTTCTGCTTTATATGAACACACTAGTAATATTACCTTTTGC
oBVT286	CCAAGAAGTAAAGATCTTATTATGAACACACTAGTAATATTACCTTTTGC
oBVT287	CCAAGAAGTAAAGATCTTATCTTGGACATTTTCAGACACCATTTTTC
oBVT288	AATAAACAAGTTCTGCTTTACTTGGACATTTTCAGACACCATTTTTC
oBVT289	AATAAACAAGTTCTGCTTTACTCCTATGTCCGCTTATATACACTATATAC
oBVT290	CCAAGAAGTAAAGATCTTATCTCCTATGTCCGCTTATATACACTATATAC
oBVT291	CCAAGAAGTAAAGATCTTATTCCTAATTTACGTCTAGTCGATGTTAAAAAG
oBVT292	AATAAACAAGTTCTGCTTTATCCTAATTTACGTCTAGTCGATGTTAAAAAG
oBVT293	AATAAACAAGTTCTGCTTTATCCTATCAATTATAACAAAGGTATTTACAAATAG
oBVT294	CCAAGAAGTAAAGATCTTATTCCTATCAATTATAACAAAGGTATTTACAAATAG
oBVT295	CCAAGAAGTAAAGATCTTATTACATCTTGGACATGGAATTGTTAAGC
oBVT296	AATAAACAAGTTCTGCTTTATACATCTTGGACATGGAATTGTTAAGC
oBVT164	GAGAATTGGCTAGCAGATCTGGTACCGAATTCGCCACCAT
oBVT299	GATCCCTCGAGGAGCGGCCGCCTGCTTTAAGCAAAGTCTGG
oBVT300	GATCCCTCGAGGAGCGGCCGCCTGCTTTAACAATGAGTATTACTCAACAGGTG
oBVT301	GATCCCTCGAGGAGCGGCCGCCTGCTTTATATGAACACACTAGTAATATTACC
oBVT302	GATCCCTCGAGGAGCGGCCGCCTGCTTTACTCCTATGTCCGCTTATATAC
oBVT303	GATCCCTCGAGGAGCGGCCGCCTGCTTTAAACCTACATTGTGCACTTTTTTTTTTG
oBVT304	GATCCCTCGAGGAGCGGCCGCCTGCTTTATCCTATCAATTATAACAAAGGTATTTACAAATAG
oBVT305	GATCCCTCGAGGAGCGGCCGCCTGCTTTAGTCGGAAGAGAGAAATGG
oBVT306	GATCCCTCGAGGAGCGGCCGCCTGCTTTAGTTTGTGCAGTGGTTC

oBVT307	GATCCCTCGAGGAGCGGCCGCCTGCTTTACTTGGACATTTTCAGACACC
oBVT308	GATCCCTCGAGGAGCGGCCGCCTGCTTTATCCTAATTTACGTCTAGTCGATG
oBVT309	GATCCCTCGAGGAGCGGCCGCCTGCTTTAAACAGTAGAGGGCTTAAGTAAC
oBVT310	GATCCCTCGAGGAGCGGCCGCCTGCTTTATACATCTTGGACATGGAATTGTTAAG
oBVT311	GATCTTATTAAAGCAGGCGGGAAGATGCCAAAAACATTAAG
oBVT312	GTGGATCCCTCGAGGAGCGGCTTCTTGGCCTTAATGAG
oBVT313	GTGGATCCCTCGAGGAGCGGATCAGGCTCTTCAGCCGG
oBVT314	GTGGATCCCTCGAGGAGCGGCATGACTGAATCGGACAC
oBVT248	GATCCCTCGAGGAGCGGCCGCCTGCTTTAGGAAATTGAAAAACAC
oBVT249	ATCCCTCGAGGAGCGGCCGCCTGCTTTATATACAGTATAGCAAAG
oBVT254	AATAAACAAGTTCTGCTTTATATTGTATATATAACGGACAAATTAGTC
oBVT258	GATCCCTCGAGGAGCGGCCGCCTGCTTTATATTGTATATATAACGGACAAATTAG

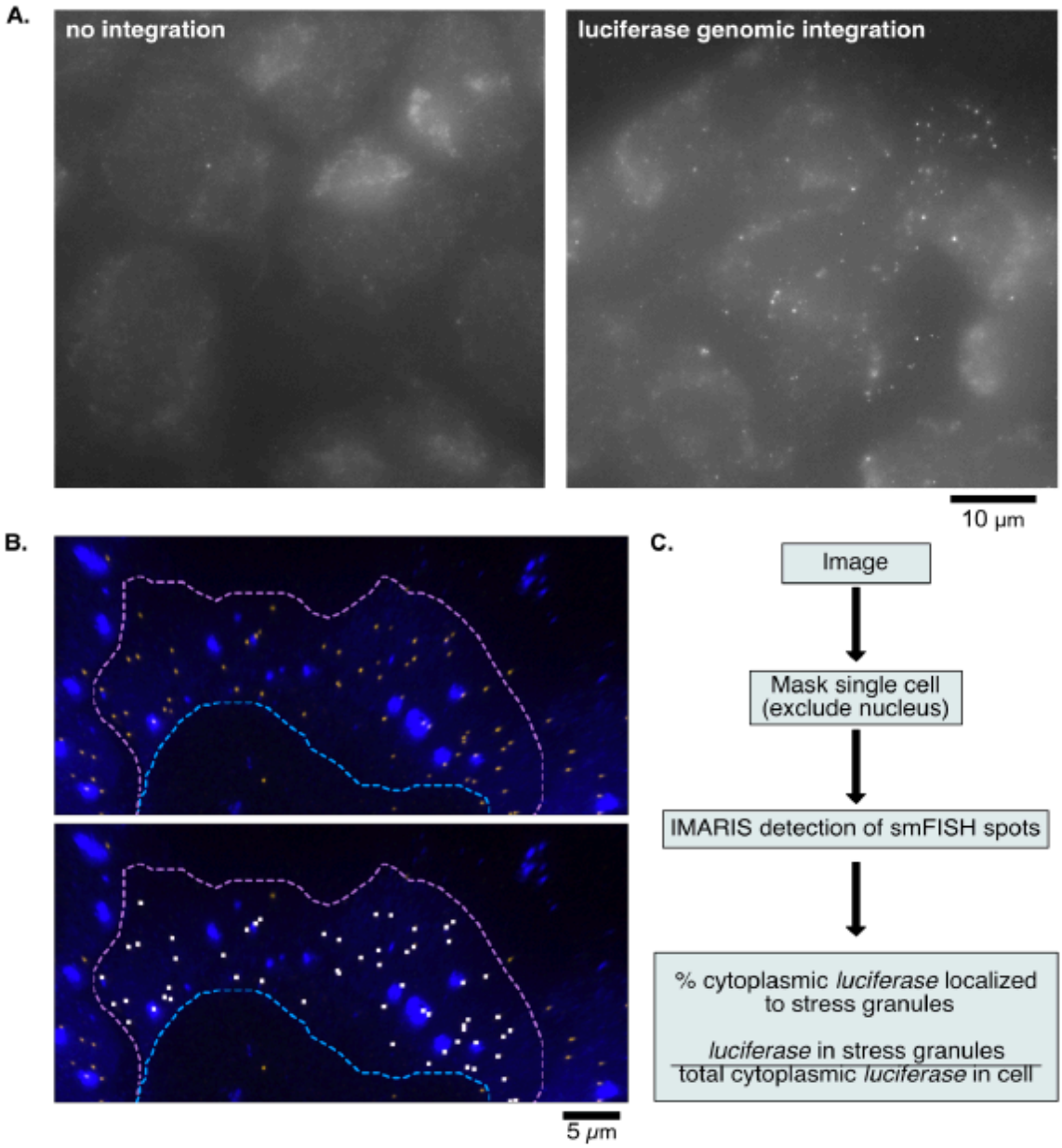

Figure A.1. *Luciferase* as a reporter mRNA.

(**A**) *Luciferase* mRNA is not endogenous to mammalian cells. Non-deconvolved microscopy images showing smFISH signal in U-2 OS cells lacking genomic integration and cells with successful genomic integration. (**B**) *Luciferase* RNA is not enriched in SGs. Stress granules in blue, *luciferase* RNA in yellow (above) or demarcated by IMARIS software in white (below). (**C**) Workflow for smFISH quantification. Following imaging, single cells can be masked using IMARIS. From here, the percent of cytoplasmic *luciferase* localized to stress granules is calculated.

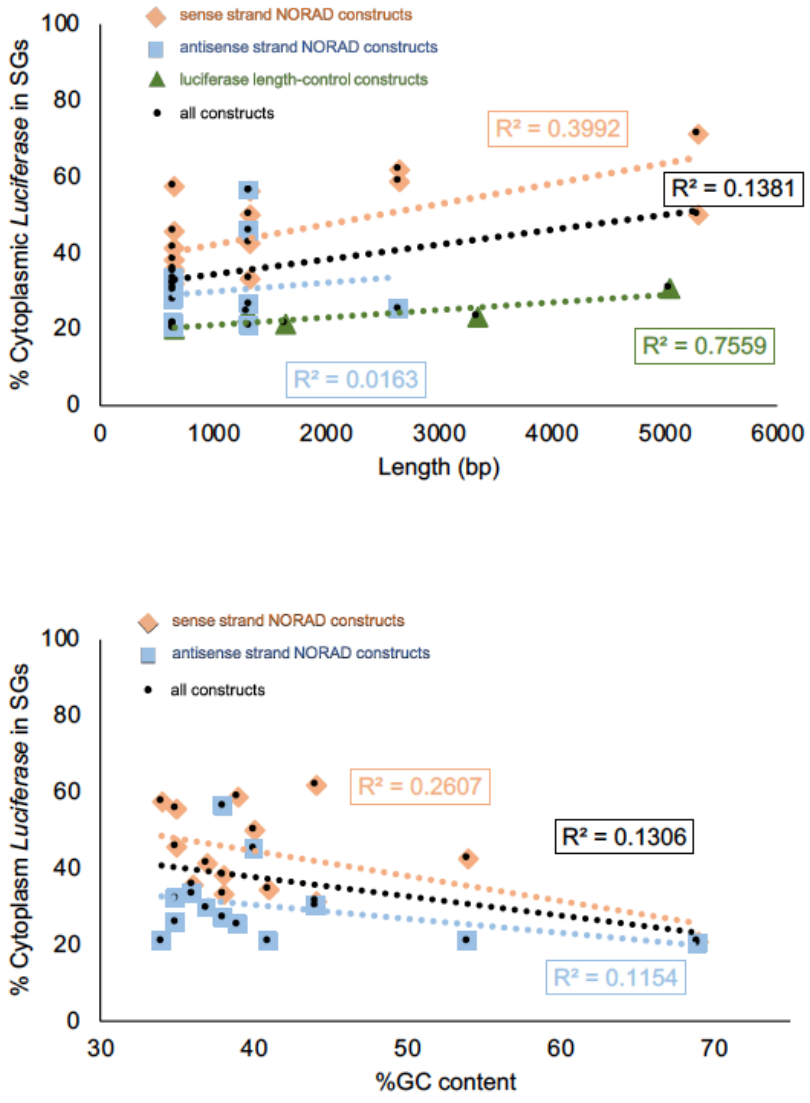

Figure A.2. Correlation between SG enrichment and length/GC content.

(**A**) Correlation between SG enrichment and constructs' length. Orange diamonds are sense-NORAD constructs, light blue squares are antisense-NORAD constructs, dark green triangles are luciferase length control constructs, and black circles are all the constructs. (**B**) Correlation between SG enrichment and %GC content of the contructs. Orange diamonds are sense-NORAD constructs, light blue squares are antisense-NORAD constructs, and black circles are all the constructs.

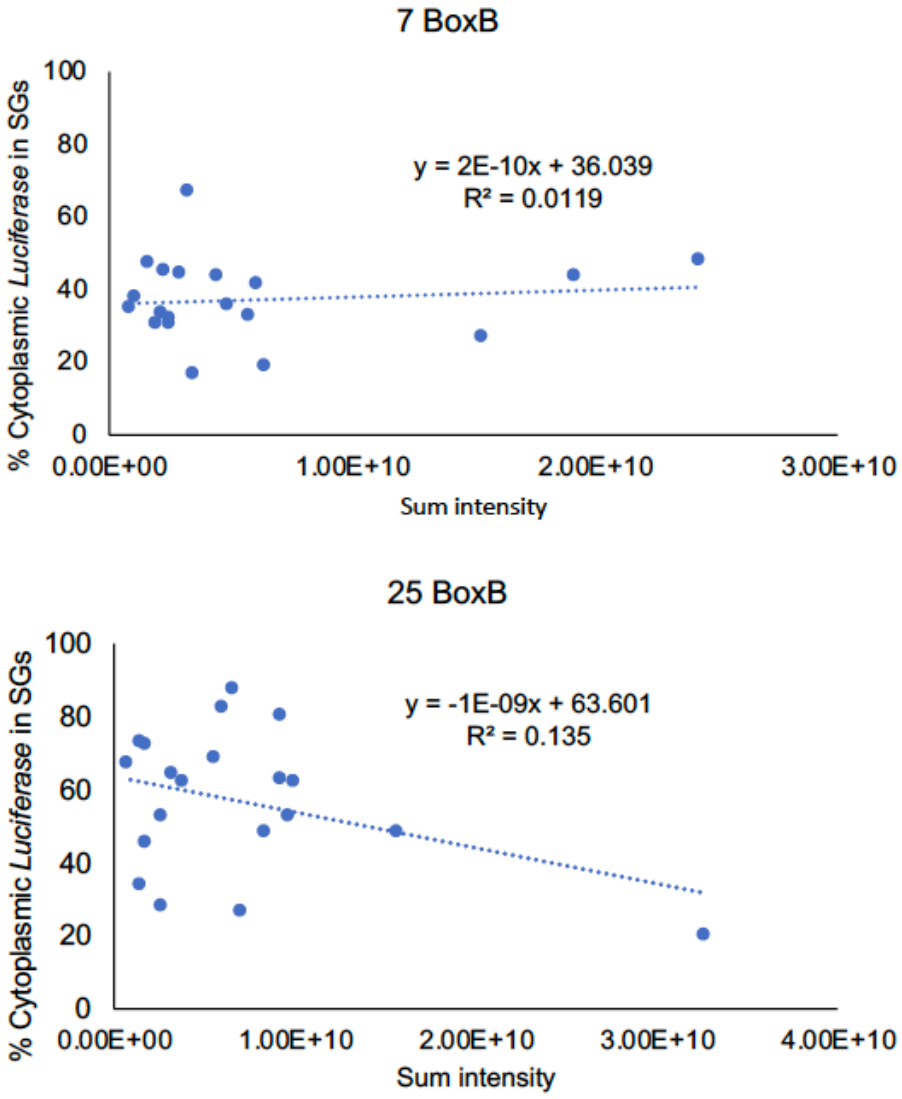

Figure A.3. Correlation between G3BP intensity and *luciferase* SG enrichment.

(**A**) Correlation between SG enrichment of *luciferase* with 7 BoxB and expression level of G3BP1-GFP-λN. (**B**) Correlation between SG enrichment of *luciferase* with 25 BoxB and expression level of G3BP1-GFP-λN.

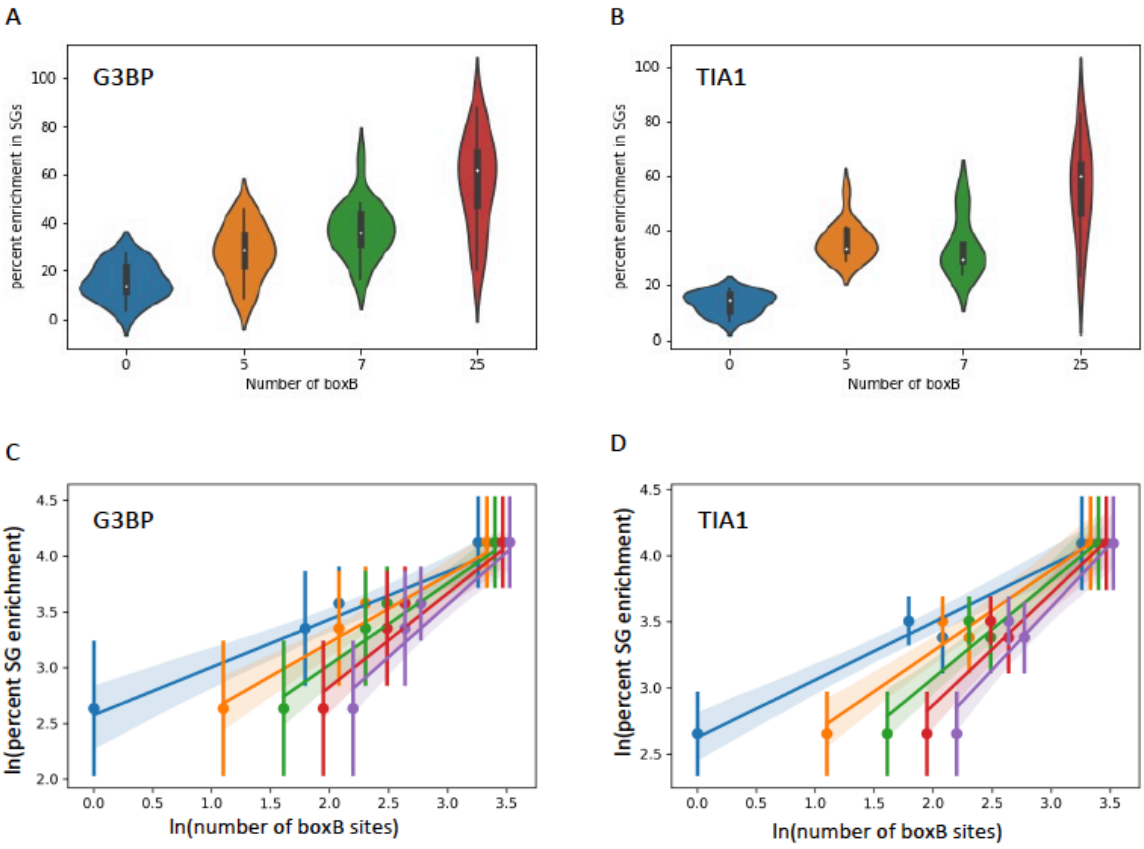

Figure A.4. Mathematical modeling of RBP interactions.

(**A**) Violin plots showing the distribution of SG enrichment for luciferase reporters with varying numbers of BoxB sites when tethered to G3BP (**B**) Same as A, but for TIA1 tethering experiments. (**C**) Logarithmic transformations of data used to perform curve fitting for G3BP tethering experiments (each line represents a different value for n). Pearson's r values from this analysis can be found in Figure 4A. (**D**) Logarithmic transformations of data used to perform curve fitting for TIA tethering experiments (each line represents a different value for n). Pearson's r values from this analysis can be found in **Figure 2.4B**.

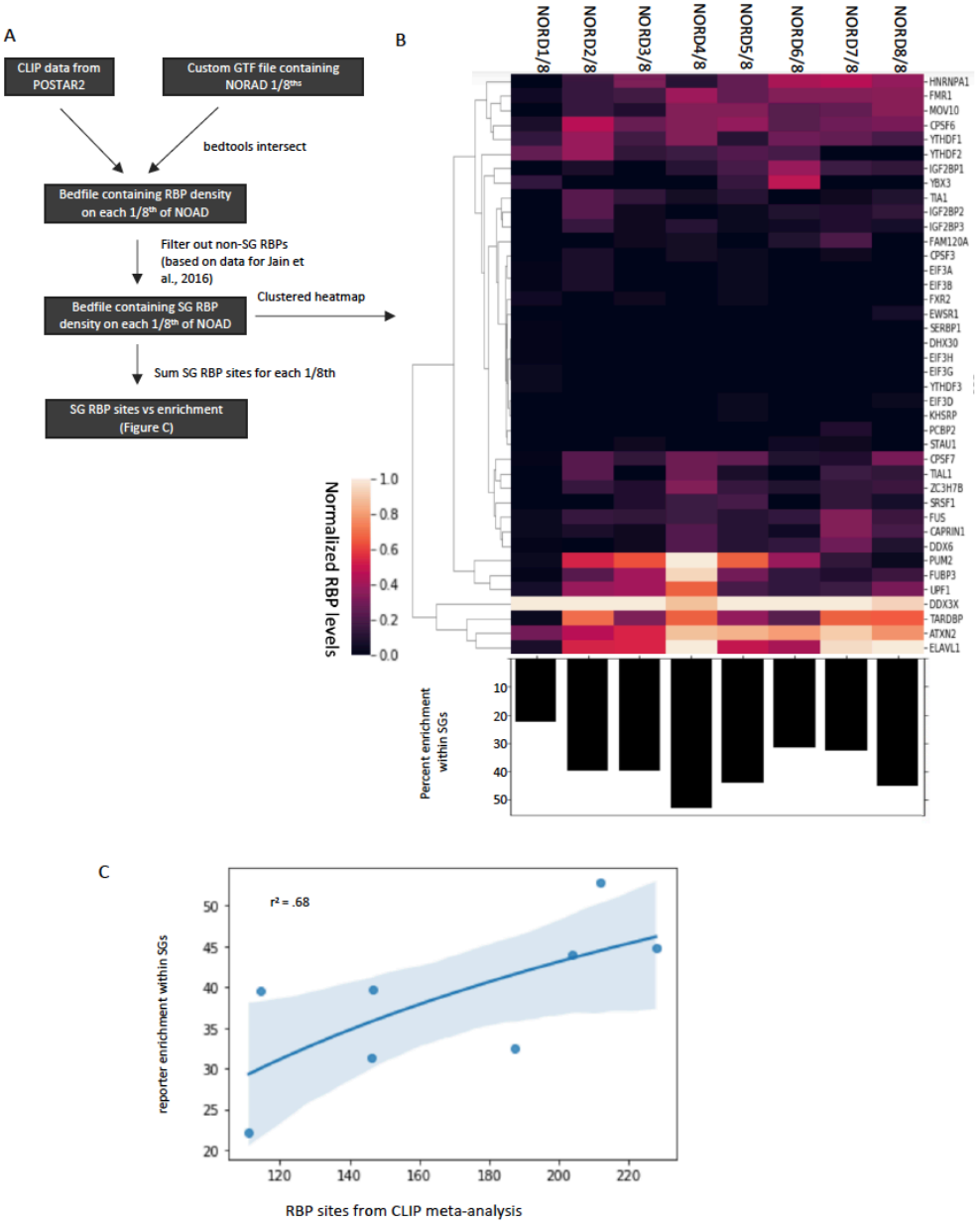

Figure A.5. CLIP analysis of NORAD RBP interactions.

(**A**) Schematic depicting how RBP CLIP analysis was performed. (**B**) *Top:* Clustered heatmap depicting RBP CLIP sites for each 1/8th of the NORAD transcript. *Bottom:* Barplots showing percentage of transcripts enriched in stress granules. (**C**) Scatterplot showing SG enrichment vs. number of summed SG CLIP sites.

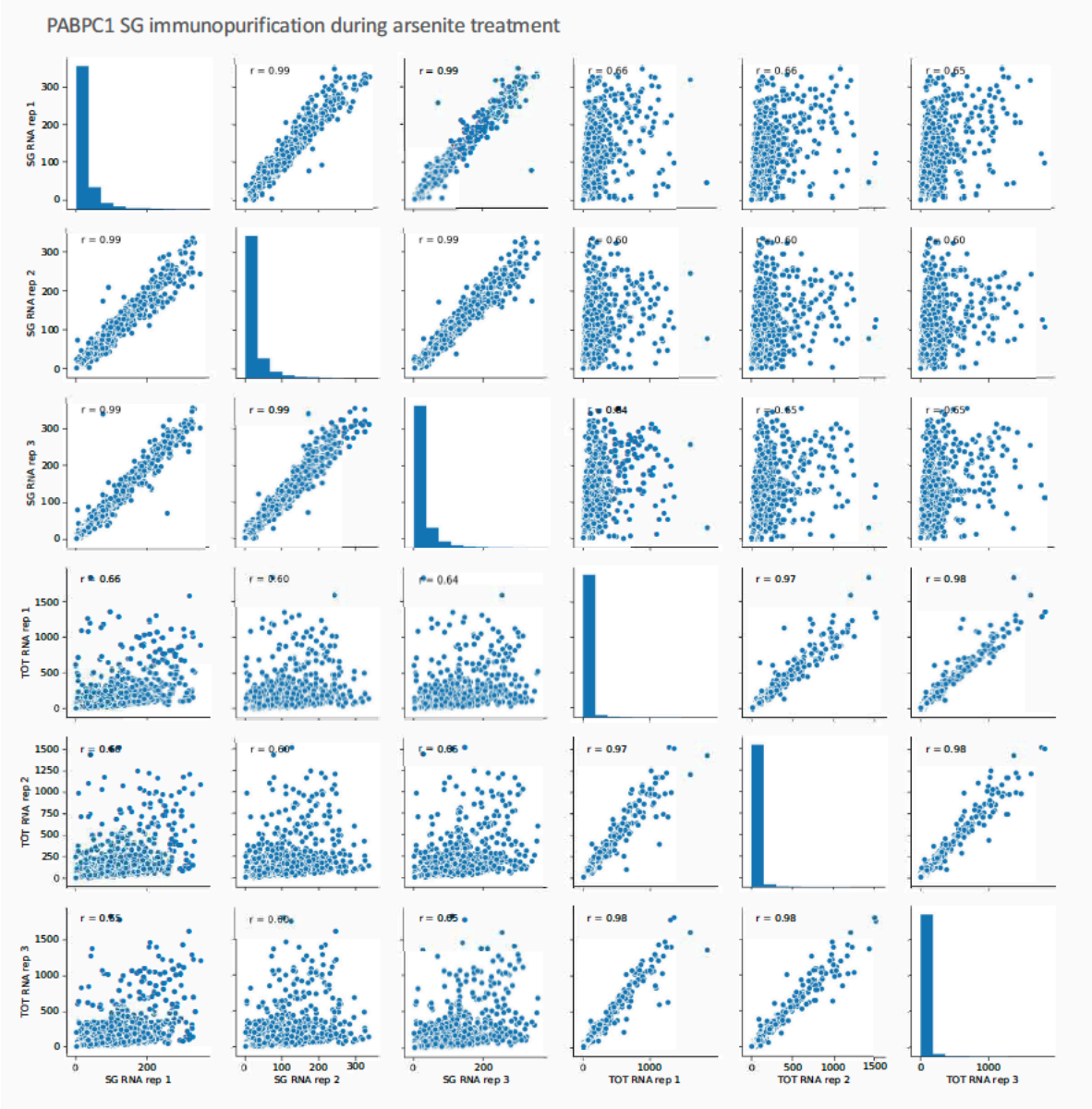

Figure A.6. Total RNA and SG core purification via PABPC1 pulldown under arsenite stress yields reproducible transcriptomes.

Pairwise scatterplots and Pearson correlations for PABPC1 SG immunopurification and total RNA replicates during arsenite treatment.

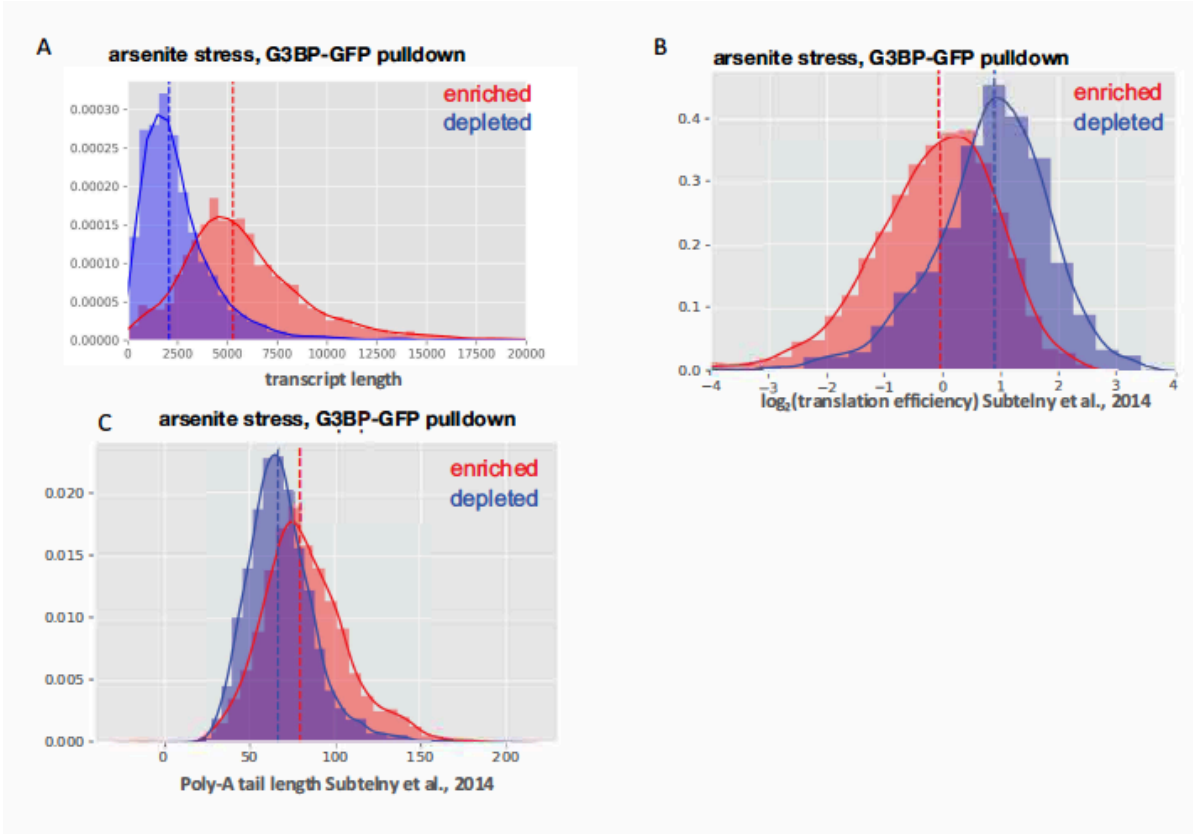

Figure A.7. SG cores purified with G3BP immunopurification are enriched for longer RNAs with decreased translation efficiency scores and longer poly-A tails.

Histograms of (**A**) transcript length, (**B**) translation efficiency, and (**C**) poly-A tail length of SG enriched and depleted transcripts from G3BP1-GFP immunopurification of arsenite-induced SGs [170].

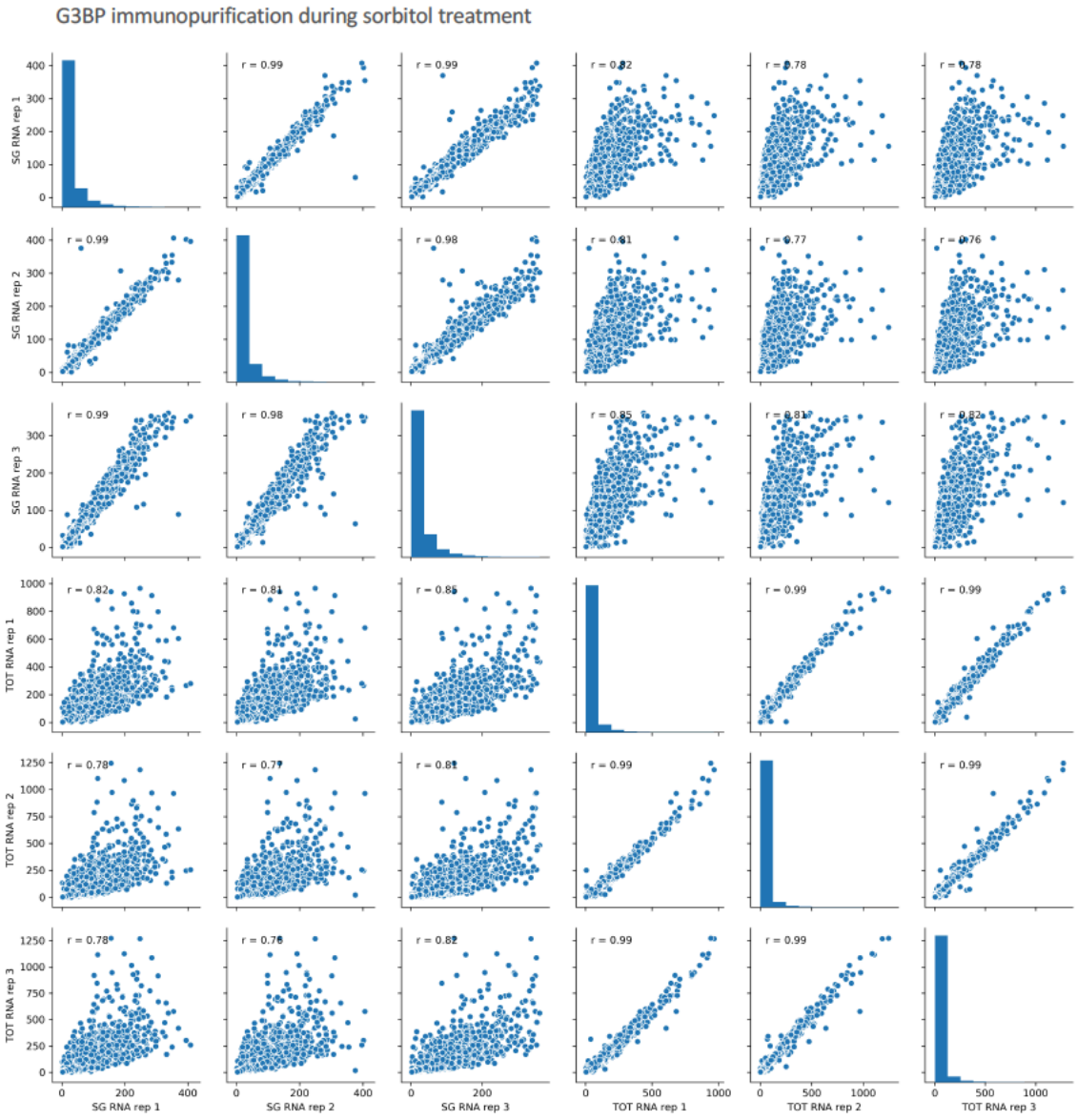

Figure A.8. Total RNA and SG core purification via G3BP1-GFP pulldown under sorbitol stress yields reproducible transcriptomes.

Pairwise scatterplots and Pearson correlations for G3BP SG immunopurification and total RNA replicates during sorbitol treatment.

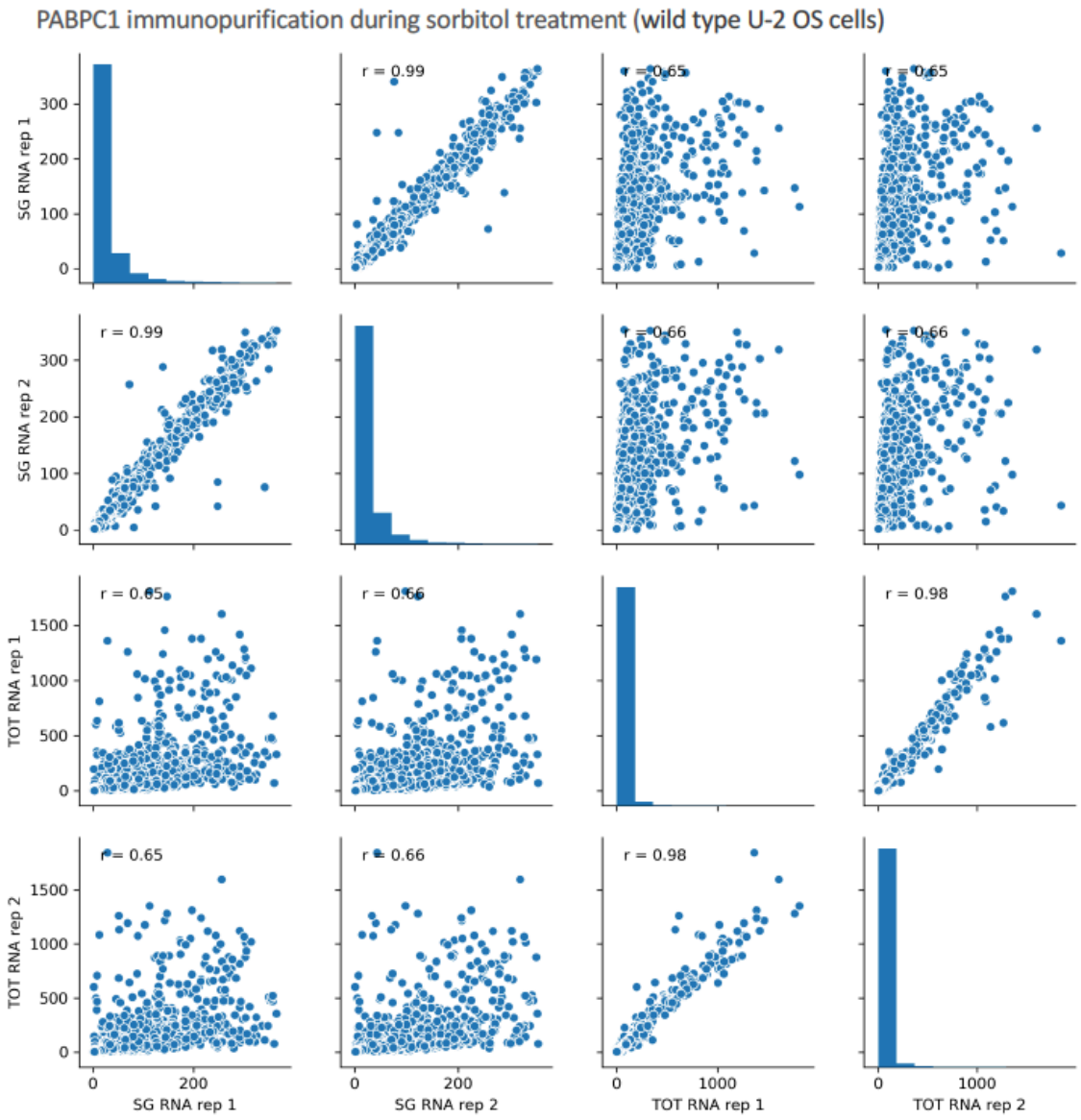

Figure A.9. Total RNA and SG core purification via PABPC1 pulldown under sorbitol stress yields reproducible transcriptomes.

Pairwise scatterplots and Pearson correlations for PABPC1 SG immunopurification and total RNA replicates during sorbitol treatment.

Figure A.10. Total RNA and SG core purification from ΔΔG3BP1/2 cells via PABPC1 pulldown under sorbitol stress yields reproducible transcriptomes.

Pairwise scatterplots and Pearson correlations for PABPC1 SG immunopurification and total RNA replicates during sorbitol treatment in ΔΔG3BP1/2 cells.

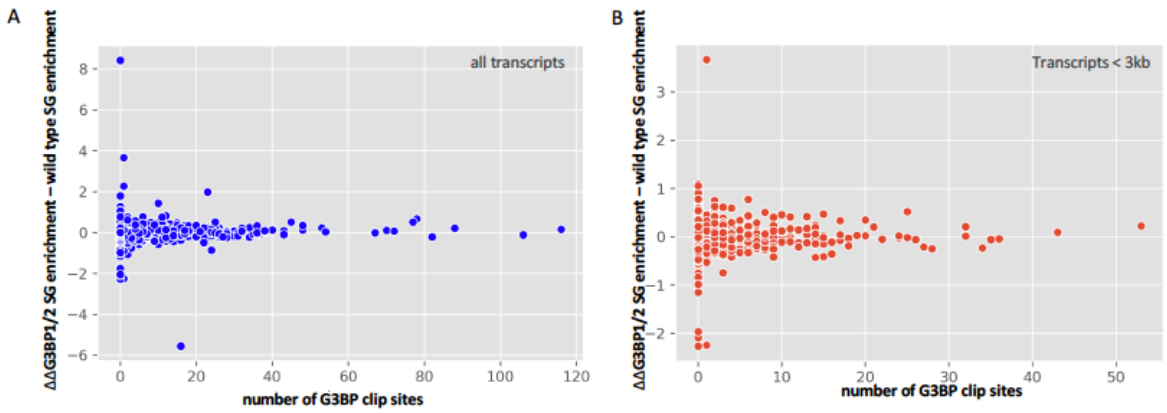

Figure A.11. Analysis of the change in SG enrichment scores in G3BP deletion cells as a function of the number of G3BP CLIP sites.

(**A**) ΔΔG3BP1/2 SG enrichment – wild type SG enrichment vs. number of G3BP CLIP sites. (**B**) Same as (**A**), but only for transcripts < 3 kb.

Table A.3. List of all the compounds tested as PARN inhibitors with their corresponding properties.

The table listed all the compounds in previous studies and this studies with their determined IC50/K_i and whether they can inhibit PARN *in vitro* and in cells.

	Compound name	Rename	PARN inhibitor *in vitro*	IC50 (μM)	K_i (μM)	PARN inhibitor in cells
Computational docking	5-ITU	5a	no	n.d.	n.d.	n.d.
	5-bromotubercidine	5b	no	n.d.	n.d.	n.d.
	Tubercidine	5c	yes	n.d.	n.d.	n.d.
	Vidarabine	5d	no	n.d.	n.d.	n.d.
	AZD8835	5e	no	n.d.	n.d.	n.d.
	Clofarabine	5f	no	n.d.	n.d.	n.d.
	AICAR	5g	no	n.d.	n.d.	n.d.
	Spongosine	5h	yes	n.d.	n.d.	n.d.
	Regadenoson	5i	yes	n.d.	n.d.	n.d.
	2,6-diamino adenosine	5j	yes	n.d.	n.d.	n.d.
	2-amino adenosine	5k	no	n.d.	n.d.	n.d.
	Cladribine	5l	yes	n.d.	n.d.	n.d.
	TWS119	5m	no	n.d.	n.d.	n.d.
	L-adenosine	5n	no	n.d.	n.d.	n.d.
	GNF-7	5o	yes	34.56	n.d.	**yes**
High-throughput screening	SYG-00454609	TH1	yes	1.39	n.d.	no
	SYG-00457029	TH2	yes	7.22	n.d.	no
	SYG-00456810	TH3	yes	5.25	n.d.	no
	SYG-00466189	TH4	yes	5.11	n.d.	no
	SYG-00465471	TH5	yes	2.91	n.d.	no
	SYG-00457986	TH6	yes	8.09	n.d.	no
	SYG-00449761	TH7	yes	1.64	n.d.	no
	SYG-00446344	TH8	yes	3.94	n.d.	no
	SYG-00466277	TH9	yes	5.50	n.d.	no
	SYG-00458754	TH10	yes	5.71	n.d.	no
	SYG-00457386	TH11	yes	3.36	n.d.	**yes**
	SYG-00459052	TH12	yes	3.30	n.d.	no
	SYG-00463654	TH13	yes	6.26	n.d.	no
	SYG-00449350	TH14	yes	2.50	n.d.	no
	SYG-00456208	TH15	yes	2.00	n.d.	**yes**
	SYG-00445034	TH16	yes	7.90	n.d.	**yes**
	SYG-00462261	TH17	yes	9.46	n.d.	no
	SYG-00447413	TH18	yes	0.20	n.d.	no

Ref. 251	9-(3′,4′, dideoxy-3′-fluoro-β-d-glucopyranosyl)-*N*6-benzoyl adenine	A2	yes	n.d.	510 ± 52	n.d.
	1-(3′,4′, dideoxy-3′-fluoro-β-d-glucopyranosyl)-*N*4-benzoyl adenine	A6	yes	n.d.	210 ± 45	n.d.
	3-deoxy-3-fluoro-glucopyranose	B6	yes	n.d.	n.d.	n.d.
		C6	yes	n.d.	645 ± 37	n.d.
Ref. 253	1-(3′-deoxy-3′-fluoro-β-d-glucopyranosyl) uracil	U1	yes	n.d.	19 ± 5	n.d.
	1-(3′-deoxy-3′-fluoro-β-d-glucopyranosyl) 5-fluorouracil	FU1	yes	n.d.	98 ± 12	n.d.
	1-(3′-deoxy-3′-fluoro-β-d-glucopyranosyl) thymine	T1	yes	n.d.	135 ± 18	n.d.
Ref. 254	Neomycin B		yes	n.d.	0.4 ± 0.1	n.d.
	Paromomycin		yes	n.d.	17.3 ± 3.5	n.d.
	Lividomycin		yes	n.d.	18.7 ± 2.8	n.d.
	Kanamycin B		yes	n.d.	7.3 ± 0.4	n.d.
	Kanamycin A		yes	n.d.	64.7 ± 7.8	n.d.
	Tobramycin		yes	n.d.	7.1 ± 0.2	n.d.
Ref. 255		5a	yes	84.1 ± 6.7	n.d.	n.d.
		5b	yes	n.d.	n.d.	n.d.
		5c	yes	119 ± 25	n.d.	n.d.
		5d	yes	125 ± 32	n.d.	n.d.
		5e	yes	245 ± 20	n.d.	n.d.
		5f	yes	n.d.	n.d.	n.d.
		5g	yes	n.d.	n.d.	n.d.
		5h	yes	n.d.	n.d.	n.d.
		5i	yes	n.d.	n.d.	n.d.
		5j	yes	n.d.	n.d.	n.d.
		5k	yes	n.d.	n.d.	n.d.
		8a	yes	n.d.	n.d.	n.d.
		8b	yes	n.d.	n.d.	n.d.
		8d	yes	n.d.	n.d.	n.d.
		8e	yes	n.d.	n.d.	n.d.
		8f	yes	n.d.	n.d.	n.d.
		8j	yes	23.9 ± 3.7	n.d.	n.d.
		8k	yes	n.d.	n.d.	n.d.

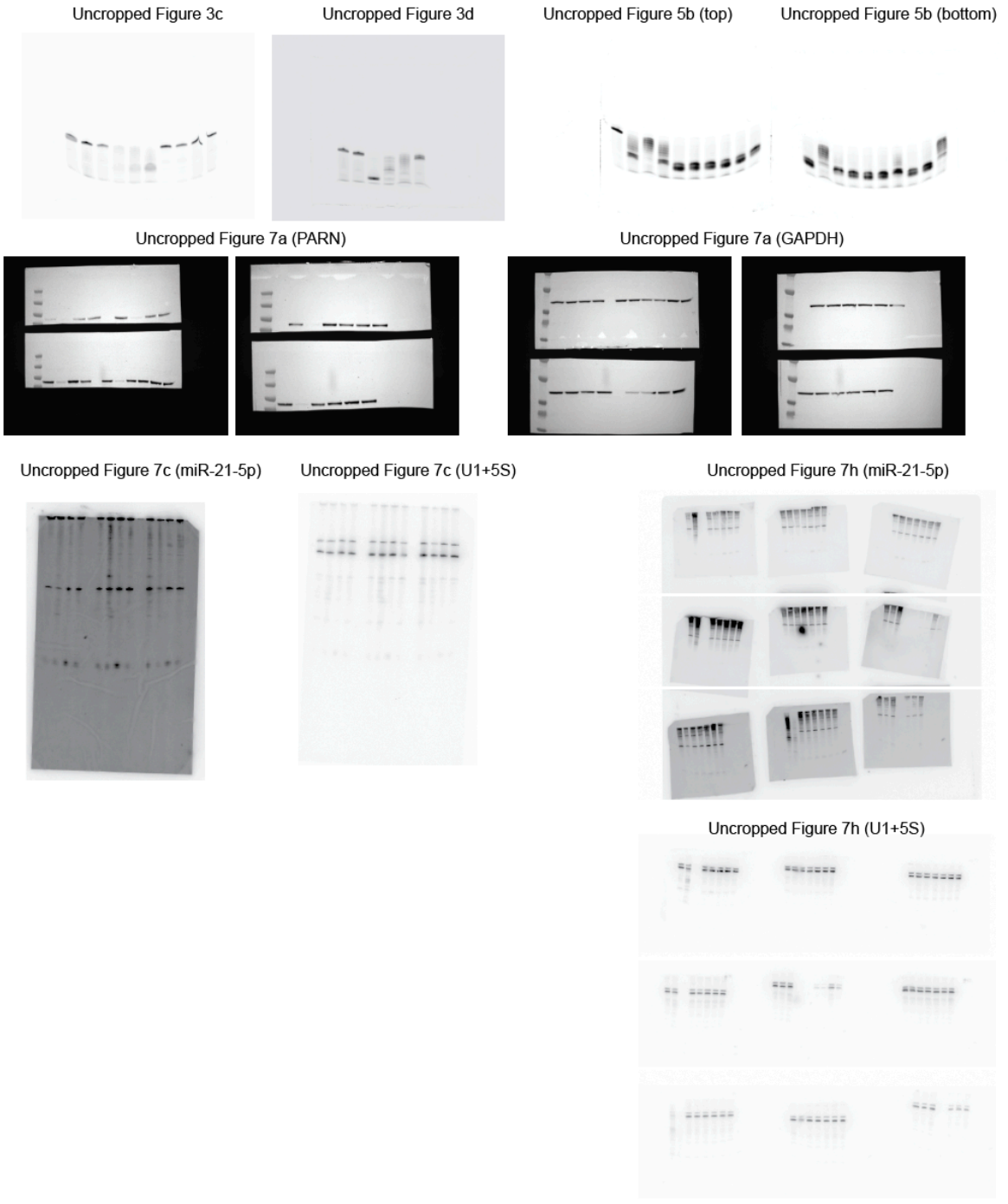

Figure A.13. Original images of gels and blots acquired during the study (Chapter III).

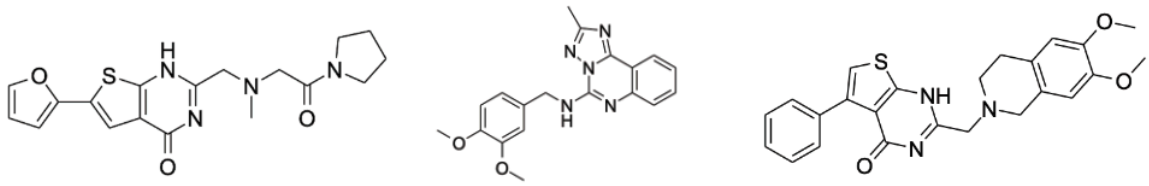

Figure A.14. Chemical structures of TH11, TH15, and TH16.